UC San Diego
UC San Diego Electronic Theses and Dissertations

Title
Computational Design of Novel Electrodes for Alkali-ion Batteries

Permalink
https://escholarship.org/uc/item/0wj315g4

Author
Guo, Xingyu

Publication Date
2022

Peer reviewed|Thesis/dissertation

eScholarship.org Powered by the California Digital Library
University of California

UNIVERSITY OF CALIFORNIA SAN DIEGO

Computational Design of Novel Electrodes for Alkali-ion Batteries

A dissertation submitted in partial satisfaction of the
requirements for the degree
Doctor of Philosophy

in

Materials Science and Engineering

by

Xingyu Guo

Committee in charge:

Professor Shyue Ping Ong, Chair
Professor Zheng Chen
Professor Olivia Graeve
Professor Ping Liu
Professor Ying Shirley Meng
Professor Tod Pascal

2022

Copyright
Xingyu Guo, 2022
All rights reserved.

The dissertation of Xingyu Guo is approved, and it is acceptable in quality and form for publication on microfilm and electronically.

University of California San Diego

2022

DEDICATION

To my grandparents. They were unable to follow their aspirations in school when they were young, but they have maintained their curiosity and desire to learn throughout their lives.

TABLE OF CONTENTS

LIST OF FIGURES

LIST OF TABLES

ACKNOWLEDGEMENTS

First of all, I would like to express my gratitude to my advisor, Dr. Shyue Ping Ong, for his support and guidance throughout my graduate studies. His professionalism in scientific research and code development are invaluable for me. My deepest gratitude also goes to the thesis committee Dr. Olivia Graeve, Dr. Ping Liu, Dr. Tod Pascal and Dr. Zheng Chen for their assistance and support in the completion of this dissertation.

Secondly, I would like to express my special thanks to Dr. Zhenbin Wang. Thank you for impressing me with your enthusiasm for research and your unreserved sharing of your research expertise. I would like to extend my sincere thanks to all my collaborators, Dr. Chi Chen, Dr. Xiangguo Li, Dr. Zhi Deng. Dr. Bo Wang, Dr. Xi Chen and Dr. Panpan Xu. I also wish to thank all the members in MAVRL group and my friends Lisa Matsukata and her dog Nina for curing depression.

Finally, I'd like to express my great gratitude to my family for always being there for me, sharing both joy and sorrow together. You are always my reason to smile.

Chapter 2 is, in total, a reprint of the material "Water contributes to higher energy density and cycling stability of Prussian blue analogue cathodes for aqueous sodium-ion batteries." Chemistry of Materials 31, no. 15 (2019): 5933-5942. Xingyu Guo, Zhenbin Wang, Zhi Deng, Xiangguo Li, Bo Wang, Xi Chen, and Shyue Ping Ong. The dissertation author was the primary investigator and author of this scientific paper.

Chapter 3 is, in full, a reprint of the material "Design principles for aqueous Na-ion battery cathodes." Chemistry of Materials 32, no. 16 (2020): 6875-6885. Xingyu Guo, Zhenbin Wang, Zhi Deng, Bo Wang, Xi Chen, and Shyue Ping Ong. The dissertation author was the primary investigator and author of this paper.

Chapter 5, in part is currently being prepared for submission for publication of the material "The Intercalation Chemistry of the Disordered RockSalt $Li_3V_2O_5$ Anode from Cluster Expansions and Machine Learning Interatomic Potentials." Xingyu Guo, Chi Chen, Shyue Ping

Ong. The dissertation author was the primary investigator and author of this paper.

I would like to acknowledge GEIRI North America for providing the financial support via Project No. SGRIDGKJ[2017]841. I would also like to acknowledge computing resources provided by the Triton Shared Computing Cluster (TSCC) at the University of California, San Diego, the National Energy Research Scientific Computing Centre (NERSC), and the Extreme Science and Engineering Discovery Environment (XSEDE) supported by the National Science Foundation, under Grant No. ACI-1053575.

VITA

2011-2015	B.S. in Materials Science and Engineering, Northwestern Polytechnical University, China
2015-2016	M.S. in Materials Science and Engineering, Northwestern University, USA
2017-2022	Ph.D. in Materials Science and Engineering, University of California San Diego, USA

PUBLICATIONS

1. **Xingyu Guo**, Zhenbin Wang, Zhi Deng, Xiangguo Li, Bo Wang, Xi Chen, and Shyue Ping Ong. "Water contributes to higher energy density and cycling stability of Prussian blue analogue cathodes for aqueous sodium-ion batteries." Chemistry of Materials 31, no. 15 (2019): 5933-5942.

2. **Xingyu Guo**, Zhenbin Wang, Zhi Deng, Bo Wang, Xi Chen, and Shyue Ping Ong. "Design principles for aqueous Na-ion battery cathodes." Chemistry of Materials 32, no. 16 (2020): 6875-6885.

3.**Xingyu Guo**, Chi Chen, Shyue Ping Ong "The Intercalation Chemistry of the Disordered RockSalt $Li_3V_2O_5$ Anode from Cluster Expansions and Machine Learning Interatomic Potentials" (*Submitted*)

4. Panpan Xu, **Xingyu Guo**, Minghao Zhang, Haodong Liu, Zhenzhen Yang, Hongpeng Gao, Mingqian Li, Guorui Cai, Yifan Zhao, Yan Chen, Ke An, Ira D. Bloom, Juchen Guo, Ping Liu, Ying Shirley Meng, Shyue Ping Ong, Zheng Chen, "Elucidation of the Defects Evolution Induced by Proton Exchange in Layered Cathode Material" (*In preparation*)

ABSTRACT OF THE DISSERTATION

Computational Design of Novel Electrodes for Alkali-ion Batteries

by

Xingyu Guo

Doctor of Philosophy in Materials Science and Engineering

University of California San Diego, 2022

Professor Shyue Ping Ong, Chair

The alkali-ion batteries are the key to unlock the bottleneck of the renewable energy storage and pave the way for a renewable-powered future. Battery technologies for grid-scale energy storage systems requires low costs, safety, high efficiency and high sustainability. In this dissertation, we present not only in-depth understandings of the electrode working mechanism but also develop novel cathode materials for alkali-ion batteries using first principles calculations. We divide the dissertation into four project-based parts.

In the first project, we performed a comprehensive study of Prussian blue and its analogues (PBAs) cathodes in aqueous sodium-ion batteries. Using density functional theory calculations, we proposed a general rule of the phase transition that dry PBAs generally undergo a phase

transition from a rhombohedral $Na_2PR(CN)_6$ (where P and R are transition metals) to a tetragonal/cubic $PR(CN)_6$ during Na extraction, which is in line with experimental observations. Using a grand potential phase diagram construction, we show that existence of lattice water and Na co-intercalation contribute to both higher energy density and better cycling stability. We also identified four new PBA compositions – $Na_2CoMn(CN)_6$, $Na_2NiMn(CN)_6$, $Na_2CuMn(CN)_6$ and $Na_2ZnMn(CN)_6$ – that show great promise as cathodes for aqueous rechargeable Na-ion batteries.

In the second project, we developed design rules for aqueous sodium-ion battery cathodes through a comprehensive density functional theory study of the working potential and aqueous stability of known cathode materials. These design rules were applied in a high-throughput screening of Na-ion battery cathode materials for application in aqueous electrolytes. Five promising cathode materials - NASICON-$Na_3Fe_2(PO_4)_3$, Na_2FePO_4F, $Na_3FeCO_3PO_4$, alluadite-$Na_2Fe_3(PO_4)_3$ and $Na_3MnCO_3PO_4$, were identified as hitherto unexplored aqueous sodium-ion battery cathodes, with high voltage, good capacity, high stability in aqueous environments and facile Na-ion migration. These findings pave the way the practical cathode development for large-scale energy storage systems based on aqueous Na-ion battery chemistry.

Then in the third project, we constructed a large database of aqueous Na-ion battery cathodes (Na-ion Aqueous Electrode Database, or NAED) based on the developed design rules in the second project. By screening and analyze the data in the database, we identified two promising candidates, $NaMn_2O_4$ and $Na_2(FeVO_4)_3$ for synthesis and experimentation in aqueous sodium-ion batteries.

The final project presents a comprehensive study of Li insertion mechanism in *DRX*-$Li_3V_2O_5$ anode in Li-ion batteries. Using a combination of first-principles calculations and cluster expansion methods, we show that during discharge, Li ions mainly intercalate into tetrahedral sites, while the majority of Li and V ions in octahedral sites remain stable. Furthermore, its fast-charging nature is attributed to the facile diffusivity of Li ions via a correlated "octahedral - tetrahedral - octahedral" Li diffusion.

Chapter 1

Introduction

1.1 Background

Global climate change has had an increasing impact on human society over the last few decades, including extreme weather events, rising temperatures, deteriorating air and water quality as well as imperiled ecosystems. As called for in the Paris Agreement in 2015, to keep global warming to no more than 1.5 $°C$, emissions need to be reduced by 45% by 2030 and reach net zero by 2050.[4] One of the most important ways to mitigate the climate change is to replace the traditional polluting coal, gas and oil-fired power with energy from renewable sources, which is inexpensive and produces low greenhouse emissions and air pollution.

According to the report by the International Energy Agency, global renewable electricity generation grows by more than 8 % to reach 8300 TWh in 2021, the greatest annual growth rate since the 1970s.[2] In particular, solar PV and wind account for two-thirds of renewable energy growth. However, transition to a renewable-fueled world is still challenging due to lack of effective energy storage techniques. Generation of renewable energy is dependent on natural resources and is uncontrollable by humans. Also, the ability to output consistently high power quality is critical to achieve a stable and high-efficiency network.

To unlock the bottleneck of the renewable energy storage and pave the way for a renewable-powered future, battery technology is the key. Battery technology for grid-scale energy storage systems requires low costs, safety, high efficiency and high sustainability.

1.2 Review of the alkali ion batteries

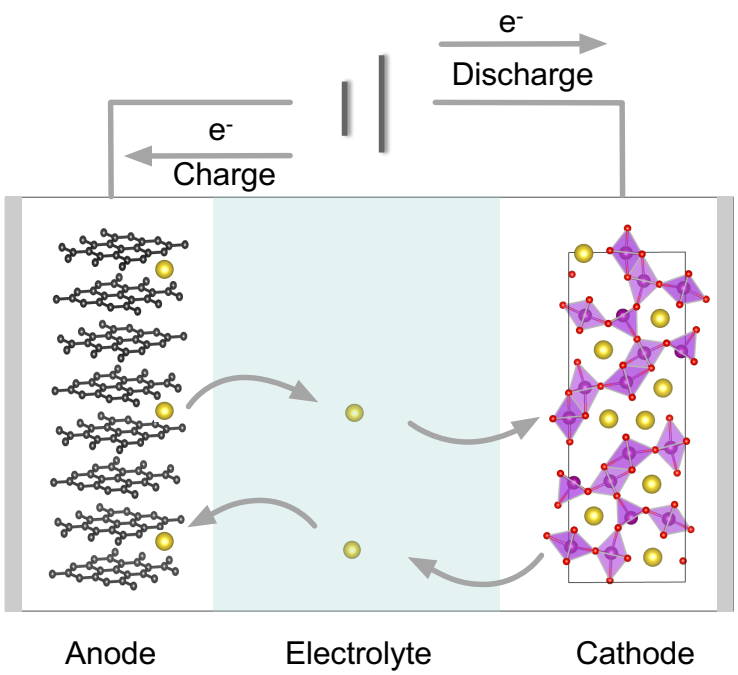

Figure 1.1: Schematic illustration of an alkali-ion battery

Figure 1.1 shows a schematic illustration of a typical rechargeable alkali-ion battery. Alkali-ion battery consists of two electrodes, cathodes and anodes, seperated by an electronically insulating, ion-conducting electrolyte. During discharge, alkali ions migrate from the anode to the cathode through electrolyte and meanwhile electrons transfer through the external circuit. During charge, alkali ions de-intercalate from the cathode and migrate back into the anode. The redox reactions occurs during the whole electrochemical process. For example, in a $LiMO_2$||C

battery, the reaction can be expressed as follows:

$$\text{Cathodes: } LiMO_2 = Li_{1-x}MO_2 + xLi^+ + xe^- \tag{1.2.1}$$

$$\text{Anodes: } C + xLi^+ + xe^- = Li_xC \tag{1.2.2}$$

$$\text{Overall reaction: } LiMO_2 + C = Li_xC + Li_{1-x}MO_2 \tag{1.2.3}$$

1.2.1 Li-ion batteries

Over the past few decades, there has been a surge in lithium ion battery production. Currently, cathodes used in a Li ion battery are intercalation compounds that are able to store Li^+ with a stable solid network. The first commercialized intercalation cathode is layered $LiTiS_2$, demonstrated by Whittingham and Thompson [175] in 1970s. Using $LiCoO_2$ as cathode and carbon as anode material, SONY released its first commercial Li ion battery in 1990s, which is still widely used in portable electronics due to its high energy density and good cycling performance.[102] The high costs and low thermal stability of cobalt-based materials leads to the investigation of other cathode materials with cheaper price and longer duration. The commercialization of $LiNi_xMn_yCo_zO_2$ (NCM) and olivine type $LiFePO_4$ (LFP) battery has led to a surge in energy storage industry over the last ten years. NCM batteries are preferred in applications of electric vehicles because of its high energy density, high lithium diffusivity ($\sim 10^{-10}$ cm^2/s) and electron mobility ($\sim 10^{-6}$ S/cm).[121, 67] LFP batteries are also widely used in electric vehicles and is also a promising candidates for grid scale energy storage. LFP battery contains neither cobalt and nickle element, making it less costly and more environmental friendly than other commonly used batteries.[119] Compared with $LiCoO_2$, the phosphate framework of $LiFePO_4$ is shown to be much stable against oxygen release up to temperature of 500 $\sim$ 600 °C, making LFP the safest battery in today's market. [32] Furthermore, LFP battery is able to sustain excellent cycling performance for more than 3000 cycles under most situations.[131] Recently,

disordered rocksalt (DRX) materials have been intensively studied as promising candidates for cathodes Li ion batteries. With a closely packed face-centered-cubic lattice, DRX materials are able to achieve high energy density. The disordered arrangement of cations lead to chemical variety, reducing the dependent on high cost Co, Ni and Mn element in batteries.[29]

Up to date, graphite has been the dominant anode material used in lithium ion batteries due to its high energy density, superior electrical and ionic conductivity, high surface area and modest volume change during electrochemical reactions.[57, 22, 21] There are two major drawbacks of graphite anode: the safety issues caused by Li dendrite growth at low voltage potential and its limited capacity ($\sim$ 350 mAh/g).[99] Silicon based anode has around ten times the specific capacity of the conventional graphite anode. but oxide passivation on silicon surface and its relatively large volume expansion during Li insertion still affect its long-term stability. Recently, the development of nanotechnology has made the commercialization of Si anode on the verge. [111, 30] Lithium-titanate (LTO) battery uses insertion compound spinel $Li_4Ti_5O_{12}$ as anode, which provides safe, high rate capability but low energy density ($\sim$ 177 Wh/L) cells relative to those with graphite/carbon anodes.[155, 78] Recently, disordered rock salt $Li_3V_2O_5$ compound has been shown to yield high energy density and rate capability at a higher voltage of 0.6 V against Li (vs 0.1 V for traditional graphite), which can prevent Li plating and lead to faster charging and safer Li ion batteries.[98]

1.2.2 Na-ion batteries

Since 2010, demand for Li-ion batteries has increased exponentially, raising concerns about future supply risks due to limited lithium resources in the earth's crust. Therefore, the abundance and low cost of Na in crust ($\sim$9.10 wt%) and sea water ($\sim$1.08 x 10^{-2} kg/L) made Na-ion batteries promising candidates for future energy storage systems.[160, 76] Unlike Li-ion batteries, the commercialisation of Na-ion batteries is just at its initial stage.

The overall chemistry of Na-ion batteries is identical to that of Li-ion batteries, where

Na ion shutting between two electrodes upon charge/discharge. In general, the average voltage of cathodes in Na ion batteries is 0.5 V lower than that in Li ion batteries due to a cathodic effect.[115] Layered oxides Na_xMO_2 compounds, for example, $P2$ and $O3$-Na_xTMO_2, have been intensively investigated as cathode materials in Na-ion batteries.[82] The tunnel-type $Na_{0.44}MnO_2$ (Space group: *Pbam*) compound is among the most well-studied cathodes in Na-ion batteries. $Na_{0.44}MnO_2$ exhibits consecutive biphasic reactions with Na^+ intercalation within $2.0 \sim 3.5$ V vs Na/Na^+.[174] The inter-connected diffusion channels and the abundant vacancies in the structure facilitates Na^+ diffusion in the charge/discharge processes, achieving a specific capacity of 120 mAh/g.[70]

Compared with oxide compounds, polyanionic compounds are more stable against overheat due to the strong $P-O$ covalent bond. The Natrium Super Ionic CONductor (NASICON) compounds have been extensively studied as cathodes in Na-ion batteries due to their open framework, which enable facile Na^+ diffusion.[41] Particularly, $R\bar{3}c$-$Na_3V_2(PO_4)_3$ is the most widely investigated NASICON-type cathode, which is shown to be stable over 3000 cycles with retained capacity of 82 mAh/g. [141]. Fe-based phosphates are another group of compounds that have attracted much attention from researchers. For example, Olivine-$NaFePO_4$, pyrophosphate-$Na_2FeP_2O_7$ and mixed anionic phosphate $Na_4Fe_3(PO_4)_2P_2O_7$ have all been shown as host for Na ions at average redox potential of around 3 V vs Na/Na^+.[35, 65, 37].

Prussian blue analogues (PBAs) with a general chemical formula of $A_xP[R(CN)_6]_{1-y} \cdot nH_2O$ (A = alkali or alkaline ion, P and R = transition metals), have been demonstrated as excellent cathode materials for Na-ion batteries because their open 3D framework enables fast ionic diffusion and superior cycling stability.[164] In particular, $K_{0.6}Ni_{1.2}Fe(CN)_6 \cdot 3.6\,H_2O$ show great performance during electrochemical cycling of Na^+ ions with a zero strain.[173]

Commercialization of Na ion batteries is just getting started. CATL recently released its first generation Na-ion batteries, which feature Prussian White as the cathode and hard carbon as the anode. The energy density of the released battery is able to achieve up to 160 Wh/kg. Although

the demonstrated energy density is lower than that of LFP batteries, its faster charging rate, high system integration efficiency (> 80 %) and improved low temperature (-20° C) performance made the future applications of Na ion batteries promising.[1]

1.3 Motivation and overview

Grid-scale battery storage is essential for achieving a sustainable future. Batteries used in grid-scale energy storage systems must be safe and cost effective, ensuring long term stability. Among all the electrochemical technologies, lithium ion batteries are the most commonly used and show the highest energy density, cycle stability and energy efficiency. However, some intrinsic limitations make the current Li ion batteries less feasible for grid energy storage. One of the major issue is the safety. The growth of lithium dendrite at the surface of anode cause batteries to short-circuit. Also, the organic liquid electrolyte inside conventional cells is toxic and intrinsically flammable, which may results in fires and explosions when the batteries are overheated. It is therefore of critical importance to develop novel electrode materials for the next-generation energy storage technologies.

Na-ion batteries are promising alternatives for energy storage in future industries due to their low cost and high ionic conductivity compared to their lithium counterparts. In particular, aqueous Na ion batteries, which uses aqueous solution as electrolyte, has been shown to be promising candidates for grid-energy storage. An aqueous electrolyte is inherently safe and environmentally benign. Also, the ionic conductivity of the aqueous electrolyte is higher than those of organic electrolytes by two orders of magnitude, resulting in high round-trip efficiency.[122] As of now, only a few compounds have been studied as cathodes in aqueous Na-ion batteries with low energy density. Due to lacking of design principles, the majority of aqueous Na ion battery research is still dominated by the trial and error approach.

This thesis is divided into the following chapters:

Chapter 2 provides a comprehensive study of Prussian blue and its analogues (PBAs) cathodes and the mechanism of water co-intercalation with Na ions during charge and discharge.

Chapter 3 presents design rules for aqueous sodium-ion battery cathodes through a comprehensive density functional theory study of the working potential and aqueous stability of known cathode materials. These design rules were applied to a high-throughput screening of Na-ion battery cathode materials for applications in aqueous electrolytes.

Chapter 4 shows the high-throughput screening for cathodes in aqueous sodium ion batteries using the developed rules in Chapter 3. A high throughput (HT) workflow for automated descriptor calculations, data storage and analysis was designed and a database containing 3847 computed compounds with calculated properties of structure, phase stability, theoretical capacity, average voltage and aqueous stabilities was constructed. Two promising candidates, $Na_2(FeVO_4)_3$ and $NaMn_2O_4$ was proposed for further experimental validations.

Chapter 5 performs a comprehensive study of Li insertion mechanism in *DRX*-$Li_3V_2O_5$ anodes using a combination of first-principles calculations, cluster expansion and machine learning methods. A distinct Li intercalation mechanism and illustrations for future design of anode materials in Li-ion batteries was proposed.

Chapter 6 concludes this thesis.

Chapter 2

Water Contributes to Higher Energy Density and Cycling Stability of Prussian Blue Analogue Cathodes for Aqueous Sodium-Ion Batteries

2.1 Introduction

Aqueous sodium-ion batteries (ASIBs) are promising candidates for large-scale electric energy-storage applications due to their high rate capabilities, good cycling stabilities and high safety.[73] Compared to conventional organic solvent electrolytes, aqueous electrolytes have a narrower stable voltage window of 1.23 V, beyond which the electrolysis of H_2O occurs. Consequently, one of the key challenges in ASIBs is the discovery of electrodes with suitable working potential and high moisture stability in aqueous electrolytes.

Recently, extensive efforts have been devoted to exploring new cathodes in ASIBs. Among them, Prussian blue and its analogues (PBAs) have been investigated intensively due to their

excellent electrochemical properties. The chemical composition of PBAs can be expressed as $A_xP[R(CN)_6]_{1-y}\square_y \cdot nH_2O$, where A is an alkali or alkaline metal ion, P and R are transition metal (TM) ions, and $\square$ indicates a $R(CN)_6$ vacancy. Both P and R can undergo reversible redox reactions:

$$Na_2P[R(CN)_6] \leftrightarrow P[R(CN)_6] + 2Na^+ + 2e^- \tag{2.1.1}$$

Various crystal structures of PBAs have been reported in the literature (Figure 2.1). Prussian blue ($Fe_4[Fe(CN)_6]_3 \bullet xH_2O$) crystallize in a face-centered cubic phase (spacegroup: $Fm\bar{3}m$).[52] Under Na deficient conditions, some PBAs form a tetragonal lattice due to the elongation of c axis caused by Jahn-Teller effects of certain transition metals, such as Mn^{3+}.[149, 68] When different amounts of Na ions and water molecules enter the PBAs lattice, the symmetry of the crystal is further reduced to form monoclinic and rhombohedral structures.[149, 68, 168, 179] Figure 2.1 (a) shows the cubic/tetragonal PBA crystal structure, in which the transition metals are six-fold coordinated by nitrogen and carbon atoms connected through cyanide (CN) ligands. In the monoclinic (Figure 2.1 (b)) and rhombohedral (Figure 2.1 (a)) phase, the octahedra twist and Na ions are displaced from the face-centered sites. The open 3D framework of PBAs enables fast ionic diffusion as well as stable cycling stability during alkali intercalation/de-intercalation.

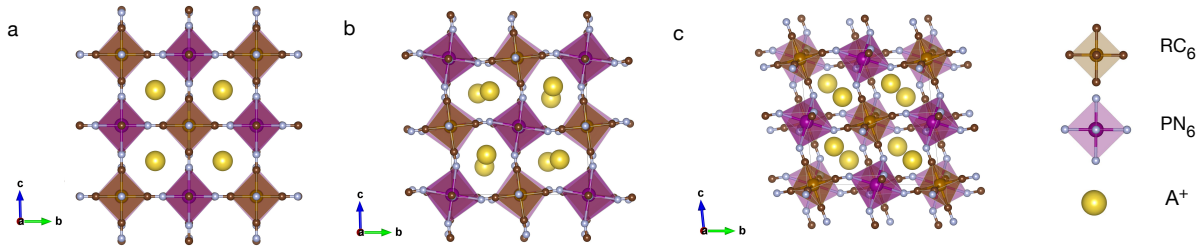

Figure 2.1: Crystal structures of PBAs. (a) cubic/tetragonal (spacegroup: $Fm\bar{3}m$ or $I4/mmm$), (b) monoclinic (spacegroup: $P2_1/c$) and (c) rhombohedral (spacegroup: $R\bar{3}$).

There have been extensive experimental studies of PBAs-based cathodes in both aqueous and non-aqueous SIBs. To optimize the performance of PBAs-based electrodes in SIBs, one common practice is to substitute the P and R sites with different transition metals. For example,

in organic electrolytes, the $Na_xFeFe(CN)_6$ compound has been reported to exhibit a reversible Na^+ insertion capacity of 120 mAh g^{-1} with 87% capacity retention over 500 cycles.[177] By replacing the P site with Ni, the reversibility can be further improved by limiting the amount of Na intercalated to 1 and hence, the volume change with cycling, and a zero capacity loss after 5000 cycles has been observed in aqueous electrolyte.[172] When both the P and R sites are replaced by Mn, an exceptionally high capacity of > 200 mAh g^{-1} has been achieved $Mn^{3+}Mn^{3+} \rightarrow Mn^{2+}Mn^{+}$.[86] Due to the flexibility of the PBA structure, there remains a wide unexplored space of PBAs.

Depending on experimental conditions, various phase transitions and polymorphs of PBAs along with distinct electrochemical behaviors have been reported. Also, the existence of lattice water in PBAs further complicates their structural and electrochemical properties. For example, Song *et al.* have reported that the existence of coordinating water molecules in $Na_2MnFe(CN)_6$ cathodes not only affects its crystal structure but also changes the shape of its voltage profile in a 1:1 diethyl carbonate (DEC) ethylene carbonate (EC) electrolyte.[149] While lattice water is generally believed to have a detrimental effect on the transport of Na^+ ions,[133] $KCuFe(CN)_6$ and $Na_2NiFe(CN)_6$ have been shown to have better cycling stability in aqueous electrolytes than those in organic electrolytes.[172, 171] The hydrated low-defect $Na_2MnFe(CN)_6$ have been determined to crystallize in monoclinic phase along with two coordination H_2O per formula by XRD techniques.[149] The O atoms have been shown to occupy the large interstitial sites and form zig-zag Na-O chains interpenetrating the 3D framework. Similar results have been reported for hydrated $Na_2MnMn(CN)_6$. The structure of $Fe_4[Fe(CN)_6]_3{\cdot}14H_2O$ have also been investigated by neutron diffraction experiment.[52] Due to the randomly distributed $Fe(CN)_6$ vacancies, the $Fe_4[Fe(CN)_6]_3{\cdot}14H_2O$ crystal deviates from face-centered cubic symmetry, and the water molecules occupy both the empty N sites of $Fe(CN)_6$ vacancies and the interstitial positions. Therefore, understanding how the presence of water influences the phase evolution with alkali intercalation may help to enhance the performance of PBA cathodes as well as contribute to their

development in ASIBs.

While density functional theory (DFT) calculations have been extensively used in the study and design of alkali-ion battery cathodes,[25, 66, 115, 95, 26] there have only been a few attempts to use DFT calculations to provide insights into PBA cathodes, probably due to the complexity of the PBA phase space and the complicating effects of lattice water. Ling et al. have shown that the intercalation of different cations into $FeFe(CN)_6$ cathodes in organic electrolytes is strongly affected by the ionic radius.[96] Xiao et al. have also studied the structural evolution of both dry and hydrated $Na_2MnFe(CN)_6$ cathode upon Na intercalation, and found that during Na intercalation, the dehydrated material undergoes a direct phase transition from orthorhombic to rhombohedral phase while the hydrated one stays in monoclinic phase and shows a stable phase at intermediate Na concentration.[181] However, their model for the hydrated phase was simplified to reproduce the correct voltage profile observed in experiment.

In this work, we performed a comprehensive study of the phase evolution of PBA cathodes in the presence of water as well as with Na intercalation. Under dry conditions, it is found that the most stable Na-rich PBA structure is always the rhombohedral phase, while the most stable Na-deficient structure is either the cubic or tetragonal phase. Using DFT grand potential phase diagrams, we show that water and Na co-intercalation behavior under different electrolyte conditions causes distinct phase transition phenomena during electrochemical reaction processes and generally increases the Na insertion voltage. Using these insights, we identified four promising aqueous Na-ion cathodes in the PBA structure using a broad suite of descriptors.

2.2 Theoretical Approach

2.2.1 Computational details

All density functional theory (DFT) calculations were performed using the Vienna *Ab initio* Simulation Package (VASP) within the projected-augmented wave method.[80, 18] The

screened hybrid Heyd-Scuseria-Ernzerhof (HSE) functional[54] was used to obtaining an accurate structural description and energies of PBAs. All analysis was carried out using HSE computed quantities, unless otherwise stated. We have also benchmarked the Perdew-Burke-Ernzerhof (PBE) generalized gradient approximation (GGA)[126] and PBEsol functionals with the Hubbard U extension (PBE+U)[84] as well as the strongly constrained and appropriately normed (SCAN) meta-GGA with van der Waals (vdW) functional implemented (SCAN + rvv10)[125] in terms of their ability to predict the average voltage of PBAs cathodes. For all structure optimizations and total energy calculations, energies and forces were converged to within 10^{-5} eV and 0.05 eV, respectively, and a k-point density of at least 1000/(number of atoms in unit cell) and an energy cutoff of 520 eV were used. All $Na_2PR(CN)_6$ were initialized with P and R in the 2+ oxidation state, while different initializations of oxidation states ($P^{3+}R^{3+}$, $P^{4+}R^{2+}$, $P^{2+}R^{4+}$) for $PR(CN)_6$ were evaluated to identify the lowest energy configuration. PBAs have been shown to exhibit various spin-ordering configurations with temperatures, compositions and photoinduction.[145, 38, 106] For all polymorphs, we calculated the total energies of all possible spin-ordering configurations and the lowest energy one was used for the property calculations (See Table 2.3). In this work, only ferromagnetic configurations were considered based on previous results from Nishino et al.[106] All crystal structure manipulations and data analysis were performed using Python Materials Genomics (pymatgen) package.[117]

2.2.2 Average voltage

The average intercalation voltage *vs* Na/Na^+ was calculated based on the following formula[8]

$$V = -\frac{E(\mathrm{Na_n P[R(CN)]_6}) - E(\mathrm{Na_(n-x) P[R(CN)]_6}) - xE(Na)}{xe} \tag{2.2.1}$$

2.2.3 Grand potential diagram

Grand potential phase diagrams have been used to study open electrochemical systems.[113, 138] For the $Na_xP[R(CN)_6$ system open to H_2O and Na, the relevant thermodynamic potential is the grand potential (Φ), defined as

$$\Phi = G_{Na_xP[R(CN)_6]\cdot \mathrm{nH_2O}} - n_{H_2O}\mu_{H_2O} - n_{Na}\mu_{Na} \tag{2.2.2}$$

where $G_{Na_xP[R(CN)_6]\cdot \mathrm{nH_2O}}$ is the Gibbs free energy, which can be approximated by the computed HSE energy at 0K for solids,[113] n_{H_2O} and μ_{H_2O} are the number of H_2O molecules per formula and the chemical potential of H_2O, respectively, and n_{Na} and μ_{Na} are the number and chemical potential of Na, respectively.

The chemical potential of liquid H_2O can be expressed as

$$\mu_{H_2O(l)} = \mu^0_{H_2O(l)} + RT\,lna_{H2O(l)} \tag{2.2.3}$$

Where $\mu^0_{H_2O(l)}$,$lna_{H2O(l)}$, R and T are defined as the chemical potential of liquid H_2O in its standard state, activity of H_2O in the electrolyte, universal gas constant and temperature, respectively. By assigning different various values to , different electrolyte conditions can be simulated.

Previously, Gautam et al. have derived the reference chemical potential for liquid H_2O from the PBE computed energy of ceH2O vapor and the enthalpy of evaporation, which has been shown to reproduce the oxide $\rightarrow$ hydroxide formation energies of main group metals.[138] Using a similar approach with HSE computed energies, we obtained $\mu^0_{H_2O(l)}$ = -19.566 eV, Separately, Nørskov et al. have computed the reference chemical potential for liquid H_2O by calculating the total energy of ceH2O vapor at 0.035 bar as the reference state because at this pressure, gas-phase ceH2O is in equilibrium with liquid water at 300 K.[107] Using this approach with

HSE computed energies, we obtained $\mu^0_{H_2O(l)}$ = -18.866 eV. In this work, we derived a $\mu^0_{H_2O(l)}$ for PBAs compounds by considering the following neutralization reaction of hydrogen cyanide and alkali hydroxide:

$$\mathrm{ACN(s)} + \mathrm{H_2O(l)} \leftrightarrow \mathrm{HCN(g)} + \mathrm{AOH(s)} \tag{2.2.4}$$

where A is an alkali metal. The enthalpy of liquid H_2O can therefore be obtained by fitting the DFT-calculated energies of HCN vapor, solid AOH and solid ACN with the experimental standard enthalpy of the reaction (ΔH_r^{exp}) obtained from the NIST Chemistry WebBook.[97] Due to limited experimental data, we performed this fitting using only two alkali metals Na and K. The DFT total energy of HCN was obtained by calculating the energy of a single molecule of HCN in a 15×15×15 A box, while the zero-point energy (ZPE) of HCN vapor was obtained from the calculated frequencies. The initial structures of AOH and ACN solids were obtained from Inorganic Crystal Structure Database (ICSD)[15] and then fully relaxed to obtain an accurate total energy from DFT calculations. The chemical potential of pure liquid H_2O is then obtained by the following formula

$$\mu^0_{H_2O(l)} = \Delta H_r^{exp} - (E_{HCN(g)} + E_{ZPE(HCN(g))} + E_{AOH(s)} + E_{ACN(s)}) - TS_{water}) \tag{2.2.5}$$

Using this approach, we derived a reference value of $\mu^0_{H_2O(l)}$ = -19.165 eV, which is in between the two reference values derived using the previous two approaches. We will discuss the implications of the reference in the Discussion section.

Finally, the chemical potential of Na, μ_{Na}, is related to the voltage V with respect to the Na metal anode by:

$$V = -\frac{\mu_{Na} - \mu^0_{Na}}{e} \tag{2.2.6}$$

where μNa^0 is the chemical potential of Na metal and e is the electron charge.

2.3 Results and Discussion

In this section, we will first present detailed benchmarks on five experimentally-known PBA compositions - $Na_xPR(CN)_6$ where (P, R) = (Mn, Mn), (Mn, Fe), (Fe, Fe), (Co, Fe), (Ni, Fe) - followed by a comprehensive screening for new PBA compositions.

2.3.1 Benchmarking of exchange-correlation functionals

The mixed-valence nature of PBAs leads to a rich electronic structure, which complicates the description of their properties by DFT calculations. Previous studies have showed that HSE functional is able to describe the structural and electronic properties of $FeFe(CN)_6$[176] as well as the sodium intercalation voltages of $Na_2MnFe(CN)_6$.[181] GGA+U methods have been shown to reach a good agreement with HSE functional only if different effective U values are applied to each individual site of $FeFe(CN)_6$,[176] which hinders its application as a predictive tool in PBAs compounds. In the Materials Project, a set of U values for the various transition metals have been calibrated for transition metal oxide systems.[61, 167] We have also evaluated the performance of various exchange-correlation functionals (PBE[126], PBE+U[167], PBEsol[128], PBEsol+U[167], HSE[54], SCAN[152], SCAN+rVV10[125]) in reproducing experimental spin configuration, lattice parameters and redox potentials of PBAs. From Table 2.4, it can be observed only HSE, PBE + U and PBEsol +U reproduce the experimental ground spin states for all tested Na concentrations. Furthermore, the HSE functional yields the most accurate lattice parameters with error less than $\sim$0.8 % across all Na concentrations and for both wet and dry PBAs (Figure 2.10) as well as the most accurate voltages (Table 2.5).

Table 2.1 compares the voltages of five well-known PBAs computed using various exchange-correlation functionals with the experimentally measured voltages. We find that both the PBE+U and PBEsol+U functionals utilizing Materials Project-calibrated U values are not able to achieve even qualitative accuracy in predicting the voltage steps of $Na_2MnMn(CN)_6$

Table 2.1: Calculated and experimental average voltages for five PBA cathodes. Individual voltage steps for $Na_2PR(CN)_6 \rightarrow NaPR(CN)_6$ and $NaPR(CN)_6 \rightarrow PR(CN)_6$ are indicated if $NaPR(CN)_6$ is a stable intermediate in the computed pseudo-binary $PR(CN)_6-Na_2PR(CN)_6$ 0K stability diagram for the functional.

Formula	Voltage (V vs Na/Na^+)			
	Exp.	PBE+U	PBEsol+U	HSE
$Na_2MnMn(CN)_6$	2.65/3.55[86]	1.14 /3.17	0.51	2.18/2.70
$Na_2MnFe(CN)_6$	3.53[149]	3.17	3.18	3.10
$Na_2FeFe(CN)_6$	3.00/3.29[168]	2.70	6.47	2.91/3.02
$Na_2CoFe(CN)_6$	3.12/3.42[179]	2.63/3.55	2.73/3.65	3.04/3.06
$Na_2NiFe(CN)_6$	3.38[86]	2.75	3.02	3.22

and $Na_2FeFe(CN)_6$. In particular, $NaMnMn(CN)_6$ is not a stable intermediate in PBEsol+U, and $NaFeFe(CN)_6$ is not a stable intermediate in both PBE+U and PBEsol+U. Furthermore, the voltages from the HSE functional are in much better agreement with the experimental voltages compared to PBE+U and PBEsol+U. Except for $Na_2MnMn(CN)_6$, the errors of all the voltages calculated by HSE are within 0.5 V.

2.3.2 Thermodynamic stability and Na intercalation in dry PBAs

Figure 2.2 shows the calculated pseudo-binary stability diagrams for the five experimentally known PBAs at x_{Na} = 0, 1, 2. At full sodiation (x_{Na} = 2), the most stable structure for all five PBAs is the densely-packed rhombohedral phase (shown in Figure 2.1 (c)). In all instances, the rhombohedral phase is more stable than the more open tetragonal, monoclinic and cubic phases by more than 30 meV/atom. At full desodiation (x_{Na} = 0), the less densely-packed cubic and tetragonal phases (shown in Figure 2.1 (a) and (b), respectively) become more stable. The elongation of *c* axes in $Na_2MnFe(CN)_6$ and $Na_2MnMn(CN)_6$ to form the tetragonal phase is due to the Jahn-Teller effect of Mn^{3+}. Consequently, under equilibrium electrochemical processes, there is a reversible phase transition from rhombohedral to cubic/tetragonal phase in *dry* PBAs-based cathodes. This trend has been observed in experiments for many PBAs compounds.[149, 168, 179, 64] The phase transformations can be interpreted by the competition between the Coulombic interaction

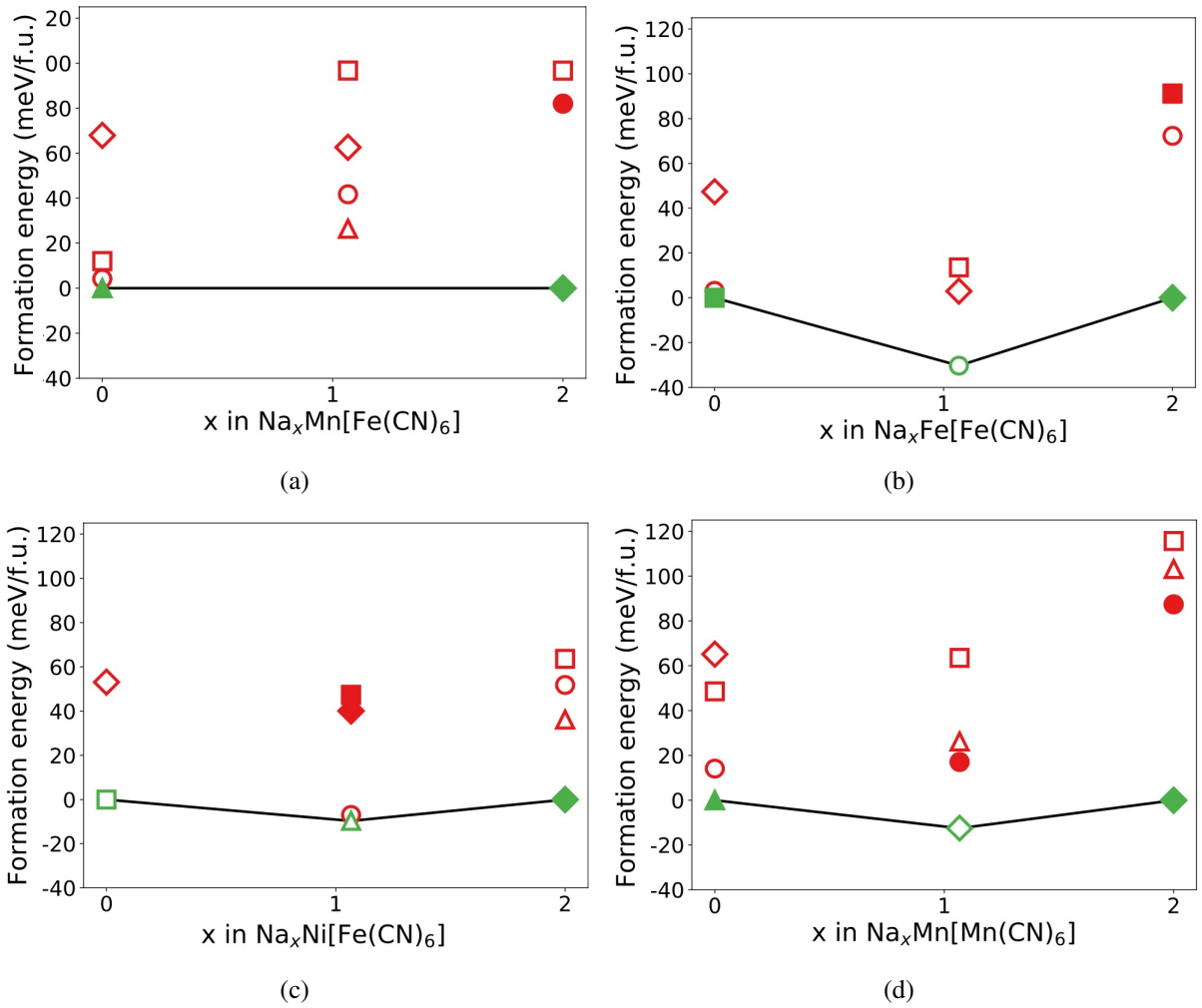

Figure 2.2: DFT-computed pseudo-binary stability diagrams of five known dry PBA compounds. All the stable phases are in green color and unstable phases are in red color. The filled markers denote the phases that have been observed experimentally. The square marker refers to cubic phase, the triangle marker refers to tetrahedral phase, the diamond marker refers to rhombohedral phase and the circle marker refers to monoclinic phase.

of Na^+ and $N^{\delta-}$ atoms and the tendency to maximize $d - \pi$ orbital overlap.[181] The former effect tends to bend the bonds and tilt the polyhedral whereas the latter straighten the lattice.

At $x_{Na} = 1$, only $NaFeFe(CN)_6$, $NaMnMn(CN)_6$ and $NaNiFe(CN)_6$ are predicted to be stable with respect to their fully sodiated desodiated counterparts. There are a few discrepancies between the DFT predicted stabilities and experimental observations. $NaMnMn(CN)_6$ has been reported to be in the orthorhombic phase, while our DFT calculations show the rhombohedral phase to be the most stable.[86] $NaCoFe(CN)_6$ has been reported to be stable in cubic phase, and two plateaus have been observed during charge/discharge processes.[179] In the DFT calculations, the cubic phase of $NaCoFe(CN)_6$ is nearly degenerate in energy with the monoclinic phase and lies only 1.4 meV/atom above the hull. We believe these discrepancies are possibly due to the effect of water and vacancies in PBA lattice. In particular, the insertion of Na ions can be largely hindered by $Fe(CN)_6$ vacancies, which has been reported to cause significant capacity fading.[133] Also, the fully-desodiated $NiFe(CN)_6$ has not been reported experimentally to the authors' knowledge, and no phase transition has been observed when rhombohedral $Na_2NiFe(CN)_6$ is oxidized to $NaNiFe(CN)_6$ experimentally.[64] The DFT calculations find the tetragonal $NaNiFe(CN)_6$ to be the most stable phase and the rhombohedral phase lies 3.8 meV/atom above the hull. We hypothesize that rhombohedral $NaNiFe(CN)_6$ is kinetically stabilized during fast charge/discharge processes.

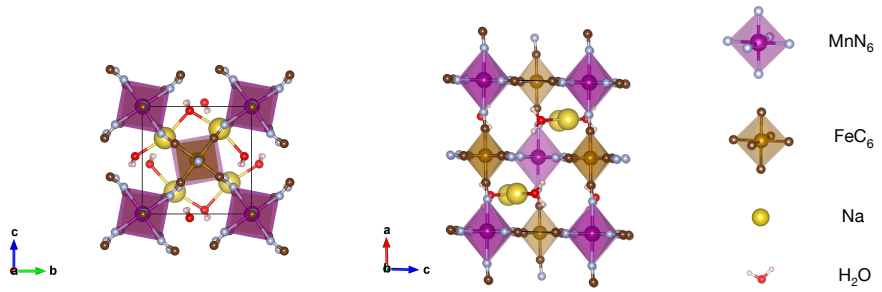

Figure 2.3: Optimized structure of $Na_2MnFe(CN)_6{\cdot}2H_2O$.

Table 2.2: Spin state and lattice parameters of $Na_2MnFe(CN)_6{\cdot}2H_2O$

Method	Spin state	Space group	Lattice parameter
Exp.	Mn: $t_{2g}^3\ e_g^2$, Fe: t_{2g}^6 (5)	$P2_1/c$	a = 7.34, b = 7.53, c = 10.59 α = 90, β = 92.1, γ = 90
HSE	Mn: $t_{2g}^3\ e_g^2$, Fe: t_{2g}^6 (5)	$P1$	a = 7.34, b = 7.46, c = 10.58 α = 90, β = 92.6, γ = 90

2.4 Effect of water in PBA lattice

To probe the effect of water on PBAs, we have selected $Na_2MnFe(CN)_6{\cdot}2H_2O$ as a model system due to the availability of experimental data on $Na_{1.89}Mn[Fe(CN)_6]_{0.97}{\cdot}1.87H_2O$.[149] Initial structures were obtained by placing two H_2O molecules per formula unit at void spaces found by Voronoi tessellation in the cubic, tetragonal, monoclinic and rhombohedral structures of *dry* $Na_2MnFe(CN)_6$. The structures were then fully relaxed by HSE functional.

Table 2.2 shows the calculated ground spin state configurations and lattice parameters of the most stable hydrated structure, which are in good agreement with experimental observations.[149] However, the positions of Na ions and H_2O molecules in our relaxed $Na_2MnFe(CN)_6{\cdot}2H_2O$ structure are opposite to those reported by synchrotron XRD and neutron diffraction. As illustrated in Figure 2.3, the DFT calculations predict that Na ions occupy the interstitial sites and coordinate with four nearest N atoms whereas H_2O molecules reside at the center of the void space. This configuration is predicted to be 6 eV per formula unit lower in energy than the experimentally reported structure. Similar results have been obtained by Xiao et al.[181] We also calculated other common hydrated PBAs and similar Na-H_2O arrangements were obtained. Given that XRD techniques are generally unable to distinguish lighter elements, we will use the lowest DFT energy hydrated structure for subsequent analysis and recommend that more advanced characterization, e.g. using neutron techniques, be carried out to confirm the positions of Na and O atoms in PBA structures. We also carried out similar calculations on $Fe_4[Fe(CN)_6]_3{\cdot}14H_2O$ and our results showed good agreement with the experimental data (see Table 2.6).

2.4.1 Effect of Na and water on the structure of PBAs

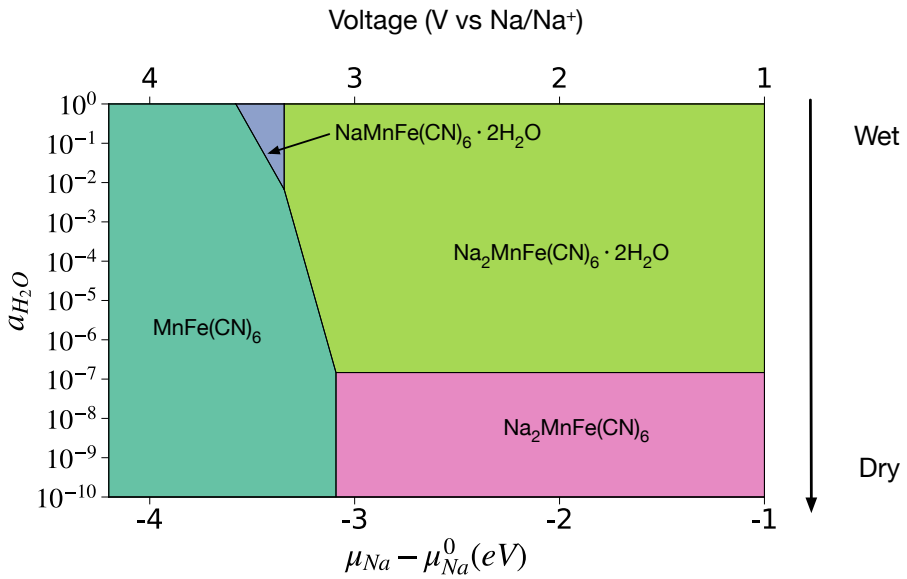

Figure 2.4: Grand potential phase diagram of $Na_xMnFe(CN)_6 \cdot nH_2O$.

Figure 2.4 shows the grand potential phase diagram of $Na_xMnFe(CN)_7 \cdot nH_2O$, where each colored region corresponds a single stable phase. Qualitatively similar results were obtained for the other common PBAs and are shown in Figure 2.13. As the chemical potential of Na decreases, Na is extracted from the PBA structure (charging process). In extremely dry electrolytes ($a_{H2O} < 10^{-8}$), only the dry $Na_xMnFe(CN)_6$ structures are stable. As the activity of water increases, hydrated phases become stable over a wider range of Na chemical potentials/voltages, which in turn result in changes in the phase transition behavior upon Na intercalation and hence, the voltage profile (see next section).

It has been well established that nearly all low-defect, Na-rich PBAs contain water in the lattice when synthesized in aqueous environments. It is also known that the hydrated monoclinic $Na_2MnFe(CN)_6 \cdot nH_2O$ disappears after several charge/discharge cycles in organic electrolytes,[149] which is consistent with the lack of hydrated phases in the computed grand potential diagram under extremely dry conditions A reversible phase transition between monoclinic hydrated $Na_2MnFe(CN)_6 \cdot xH_2O$ and rhombohedral dry $Na_2MnFe(CN)_6$ has also been observed

upon drying in vacuum followed by exposure to humid air.[149]

Our calculations show that, under same conditions, the fully desodiated structures are much more water-resistant compared with the sodiated ones. Although there have been reports of containing water molecules in Na deficient PBAs, for example $Fe_4[Fe(CN)_6]_3 \cdot 14H_2O$ and $K_{0.04}NiFe(CN)_{6.4}H_2O$[52, 64] we believe this is the effect of $Fe(CN)_6$ defects. Our calculations for the $Fe_4[Fe(CN)_6]_3$ structures containing different amount of H_2O showed that in aqueous solutions, the hydrated $Fe_4[Fe(CN)_6]_3$ is more stable than their dry counterparts (see Figure 2.14).

In dry electrolytes, a reversible phase transition between rhombohedral $Na_2MnFe(CN)_6$ and tetragonal $MnFe(CN)_6$ is predicted. During Na intercalation in wet electrolytes, different phase transition behaviors happen due to the co-intercalation of H_2O and Na ions. The crystal structure changes from monoclinic $Na_2MnFe(CN)_6 \cdot 2H_2O$ to tetragonal $MnFe(CN)_6$.

Water molecules in the PBA lattice may also serve as "pillars" that facilitate low-strain charge/discharge processes.[94, 89] Figure 2.5 shows the volume change of the three common PBAs cathodes during charge processes with respect to their fully discharged states. It can be seen that in dry electrolytes, all cathodes undergo a volume expansion of 15% $\sim$ 20% with extraction of Na^+. In wet electrolytes, on the other hand, $Na_2FeMn(CN)_6$ and $Na_2FeFe(CN)_6$ undergo a volume reduction of 7% and 4%, respectively, with extraction of Na^+, while $Na_2NiFe(CN)_6$ undergoes only a small volume increase of 1.3 %. The volume changes in wet electrolytes are therefore much smaller in magnitude compared to that in dry electrolytes, which may result in better cycling stabilities. These observations are in line with prior experimental results showing that $Na_2NiFe(CN)_6$ cathodes exhibit a near-zero capacity loss after 5000 cycles in aqueous electrolytes[172], while capacity fading of 4% has been observed after only 200 cycles[64] in organic electrolytes. These results also point to the potential for naturally hydrated compounds to serve as electrode materials in alkali ion batteries due to distinct effect of lattice water in electrochemical reactions. Several hydrated compounds have already been shown to exhibit great performance, such as $Na_{0.71}MnO_2 \cdot nH_2O$,[105] $Zn_{0.25}V_2O_5 \cdot nH_2O$ [85] and $FePO_4 \cdot nH_2O$[94].

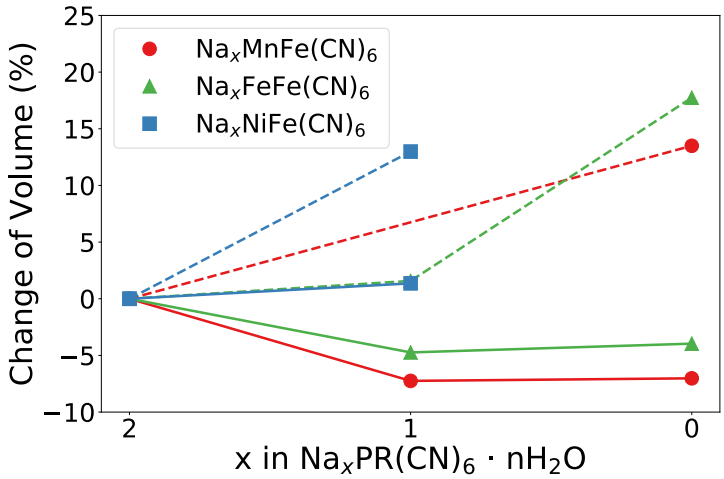

Figure 2.5: Volume change of PBAs upon Na deintercalation in wet (solid line) and dry (dashed line) electrolyte.

Figure 2.6 shows the computed voltage profiles for the $Na_xMnFe(CN)_6$, $Na_xNiFe(CN)_6$ and $Na_xFeFe(CN)_6$ PBAs in wet (a_{H_2O} = 1), dry (a_{H_2O} = 10^{-4}) and very dry (a_{H_2O} = 10^{-9}) electrolytes. The average voltage as a function of a_{H_2O} is plotted in Figure 2.12. In general, we observe that an increasing a_{H_2O} results in an increase in the voltage for all three PBAs. This is consistent with the increase of the redox potential of $Na_2MnFe(CN)_6$ in aqueous electrolyte reported in the literature.[124, 103]

For $Na_xMnFe(CN)_6$, the DFT calculations predict only a single voltage plateau of 3.09 V for $0 \leq x \leq 1$ in dry/very-dry electrolytes, while two voltage plateaus are predicted due to the emergence of the stable hydrated phase at intermediate Na concentrations in wet electrolytes. The single-plateau behavior in dry electrolytes is in line with the experimental findings of 3.44 V vs Na/Na^+.[149] Further, Pasta et al. have reported two plateaus at 3.5 V and 4.0 V vs Na/Na^+ for $Na_{1.33}Mn[Fe(CN)_6]_{0.79}$ in a saturated $NaClO_4$ aqueous electrolyte, which is qualitatively consistent with our DFT predictions.[124] Similarly, it has been reported that $Na_2FeFe(CN)_6$ exhibits two voltage plateaus at 3.0 V and 3.29 V vs Na/Na^+ in a mixture of DEC/EC electrolyte,[168] and the gap between the two plateaus becomes larger (3.1 V and 4.0 V vs Na/Na^+) in 1mol/L Na_2SO_4 aqueous electrolyte.[168, 178] These observations are again in

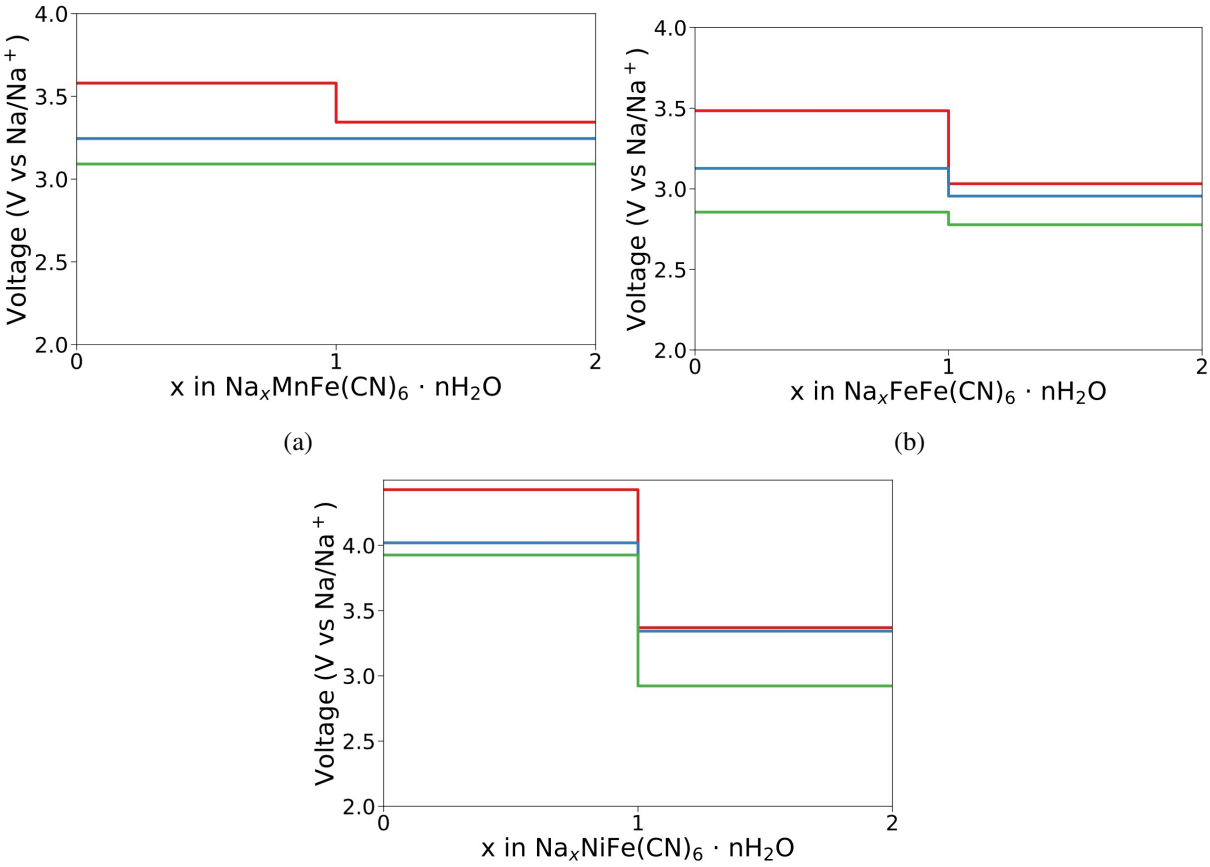

Figure 2.6: Na insertion voltage profiles (a) $Na_xMnFe(CN)_6{\cdot}nH_2O$ (b) $Na_xNiFe(CN)_6{\cdot}nH_2O$ and (c) $Na_xFeFe(CN)_6{\cdot}nH_2O$ for three water activities, representing wet (a_{H_2O} = 1, red line), dry ($a_{H_2O} = 10^{-4}$, blue line) and very dry ($a_{H_2O} = 10^{-9}$, green line) electrolytes.

qualitative agreement with our calculations.

Our results predict that the voltage of $Na_2NiFe(CN)_6$ in $0 \leq x \leq 1$ varies from 3.92 to 4.43 V vs Na/Na^+, which is beyond the stability window of aqueous solutions. Thus, only half of its theoretical capacity can be realized in aqueous electrolyte. In fact, Ni^{2+}/Ni^{3+} is known to be electrochemically inactive in PBAs cathodes,[172, 64] and this is confirmed by the integrated DFT spin densities which show that in the active redox couple in $Na_2NiFe(CN)_6$ is $Fe^{2+\rightarrow 4+}$ (see Figure 2.16(a)). The high voltage at $0 \leq x \leq 1$ is due to the $Fe^{3+\rightarrow 4+}$ couple.

One further observation is that the HSE-predicted voltages, especially at high water activities, are generally underestimated relative to experiments.[124, 178] One possible reason for this discrepancy may be the presence of defects, such as $Fe(CN)_6$ vacancies which have been reported experimentally.[52, 184] A further source of the discrepancy may be the choice of the value of the reference chemical potential of water, $\mu^0_{H_2O(l)}$. The effect of the chemical potential of water on the phase stabilities of $Na_xMnFe(CN)_6 \cdot nH_2O$ system is shown in Figure 2.7(a). From Figure 2.7(a), we can see that when becomes less negative than $\mu^0_{H_2O(l)}$, the fully hydrated $NaMnFe(CN)_6 \cdot nH_2O$ is predicted to be stable across a wider range of Na concentrations. For $\mu_{H_2O(l)} >$ -18.96 eV, $MnFe(CN)_6 \cdot H_2O$ becomes more stable than its dehydrated counterpart. The predicted Na insertion voltages as a function of $\mu_{H_2O(l)}$ is shown in Figure 2.7 (b). The predicted second voltage plateau (shown in Figure 2.7(c)) increases with and reaches a value of 3.90 V vs Na/Na^+ when $MnFe(CN)_6 \cdot H_2O$ is stabilized relative to $MnFe(CN)_6$, which is much closer to the experimentally observed voltage of 4.0 V vs Na/Na^+.[124]

We also note that the predicted voltage of $Na_2NiFe(CN)_6$ in dry electrolytes, which is 2.92 V vs Na/Na^+, deviates from the experimental finding of 3.38 V vs Na/Na^+.[64] This is mainly due to the different phase transition behaviors predicted by DFT calculations. In our calculations, a phase transition between rhombohedral $Na_2NiFe(CN)_6$ and tetragonal $NaNiFe(CN)_6$ is predicted while the rhombohedral $Na_2NiFe(CN)_6$ has been shown to be preserved in experiments possibly due to the metastability caused by fast charge/discharge processes.[64]

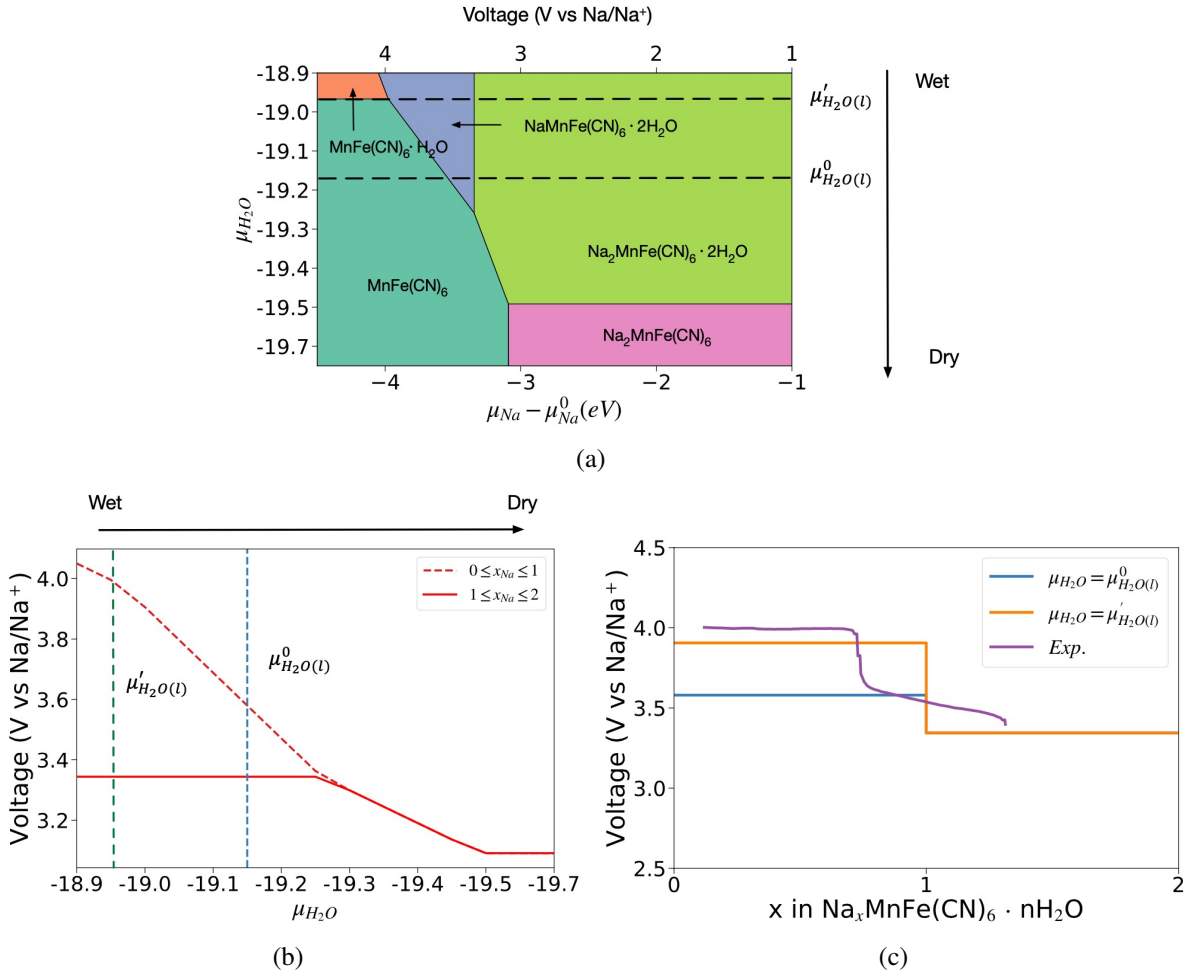

Figure 2.7: Grand potential diagram of $Na_xMnFe(CN)_6{\cdot}nH_2O$ (b) Average Na insertion voltage for low (dashed line) and high (solid line) Na concentrations as a function of the electrolyte water content (μ_{H_2O}) (c) voltage profile of $Na_xMnFe(CN)_6{\cdot}nH_2O$ at $\mu_{H_2O(l)} = \mu^0_{H_2O(l)}$, $\mu'_{H_2O(l)}$ and experimental results.

2.4.2 Screening for PBA cathodes for Aqueous Na-ion Batteries

Based on the above findings, we have performed a comprehensive screening for aqueous PBA cathodes. Only PBAs with R = Fe, Mn were considered given that they have been extensively studied experimentally, while P is allowed to be Ti, V, Cr, Mn, Fe, Co, Ni, Cu, Zn, Mo. Initial candidates for *dry* $PR(CN)_6$ and $Na_2PR(CN)_6$ PBAs were first generated using the cubic/tetragonal and rhombohedral structures, respectively.

Figure 8 shows the HSE average voltages for the PBA candidates for two Na intercalation. It is observed that except P = Ti and Mo, the R = Mn PBAs generally exhibit lower average voltages than the R = Fe PBAs, which is due to the lower standard potentials of $Mn(CN)_6^{3-/4-}$ compared to $Fe(CN)_6^{3-/4-}$.[79] For P = Ti, the integrated DFT spin densities (Figure 2.16 (g)) show that the Ti undergo a two-electron redox (2+→4+) instead of a one-electron (2+→3+) redox process on both the P and R sites. On the other hand, for the P = Ni, Cu and Zn PBAs, the integrated DFT spin densities (see Figure 2.16(a)-(f)) show that the R cation, i.e., Mn or Fe, undergo a two-electron redox from 2+ to 4+. In the case of Ni, Mn/Fe oxidation to 4+ takes place preferentially to Ni oxidation. In the case of Cu and Zn, the 3+ oxidation state is generally not preferred. The voltages of the PBAs that have been investigated experimentally (denoted with asterisks) are lie within/close to the H_2/O_2 evolution limits.

Among the compositions that have not yet been studied experimentally, $Na_2CoMn(CN)_6$ is predicted to have a relatively high average voltage of 2.48 V. During Na deintercalation, both Co^{2+} and Mn^{2+} are electrochemically active and oxidized to Co^{3+} and Mn^{3+}. $Na_2NiMn(CN)_6$, $Na_2CuMn(CN)_6$ and $Na_2ZnMn(CN)_6$ are also predicted to have relatively high average voltages of 2.52V, 2.91 V and 2.65 V, respectively, which is due to the two-electron redox of $Mn^{2+\rightarrow 4+}$. It should be noted, however, that experimentally studied $Na_2CuFe(CN)_6$ and $Na_2ZnFe(CN)_6$ have been reported to exhibit only one-electron redox, likely due to the high voltage of the $Fe^{3+\rightarrow 4+}$ redox couple (DFT predicted voltages of 3.81V and 4.24 V) beyond the O_2 evolution limit. Further detailed investigations on the effects of hydration were performed on these candidates.

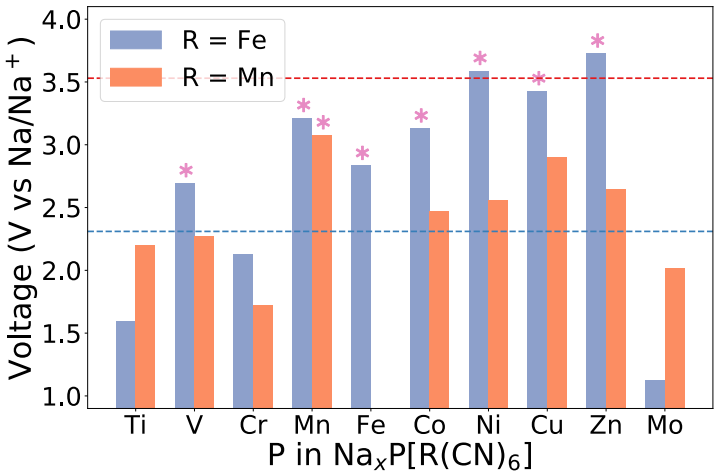

Figure 2.8: Predicted voltages for all initial candidates in the screening processes in dry electrolyte. The cathodes that are known experimentally are marked with asterisk. The red and blue lines are the potential of O_2 and H_2 evolution in water, respectively.

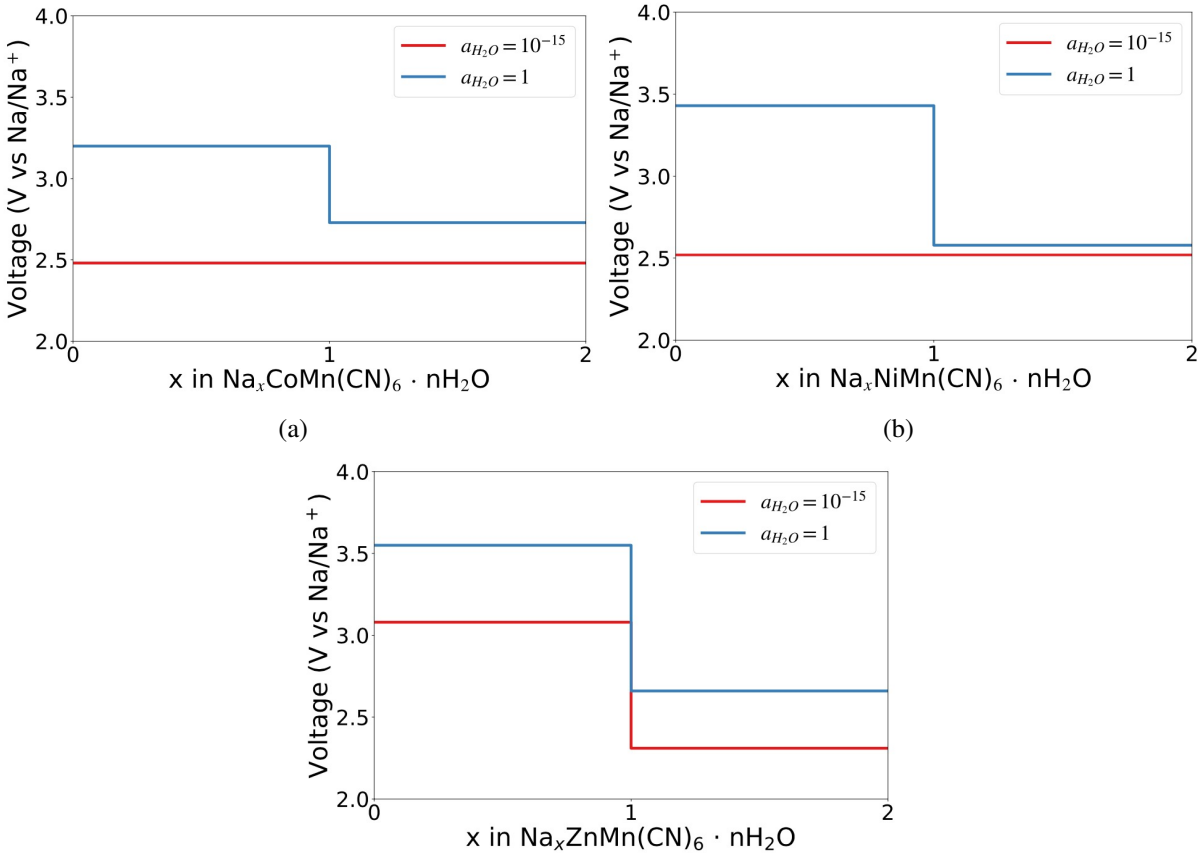

Figure 2.9: Predicted voltage profiles of the predicted PBAs cathodes.

Figure 2.9 shows the DFT-computed voltage profiles for the four candidates in both wet and dry electrolytes. The corresponding computed pseudo-binary and grand potential phase diagrams are given in Figures 2.15 and Figures 2.17, respectively. In dry electrolytes, both $Na_xCoMn(CN)_6$ and $Na_xNiMn(CN)_6$ are predicted to undergo a two-phase reaction upon charge from $x = 2$ to $x = 0$, with a phase transition from rhombohedral to tetragonal and cubic phase, respectively. In wet electrolytes, an intermediate stable phase is observed at $x = 1$, which introduces a step in the voltage profile (blue lines in Figure 2.9 (a) and (b)). The voltages of $Na_2CoMn(CN)_6$ and $Na_2NiMn(CN)_6$ are predicted to be 3.15 V/2.73 V and 3.43 V/2.58 V vs Na/Na^+, respectively.

In dry electrolytes, at , monoclinic $NaZnMn(CN)_6$ and $NaCuMn(CN)_6$ are predicted to be stable and form two plateaus on their voltage profiles. The voltage of $Na_xZnMn(CN)_6$ is predicted to be 3.08 V/2.31 V vs Na/Na^+ in dry electrolyte and 3.55/2.66 vs Na/Na^+ in wet electrolytes. $Na_xCuMn(CN)_6$ has a voltage of 3.48 V /2.33 V vs Na/Na^+ in dry electrolytes and the voltage increased to 4.12 V/2.55 V vs Na/Na^+ in wet electrolytes.

2.5 Conclusion

Using first-principles computations, we have performed a comprehensive analysis into the phase behavior of PBA cathodes for aqueous Na-ion batteries. A key contribution of our work is elucidating the effect of lattice water on the phase stability, and consequently the Na-intercalation voltage profile. We have found that all dry PBAs compounds undergo rhombohedral to cubic/tetragonal phase transitions during Na deintercalation. The presence of lattice water raises the voltage and acts as pillars to reduce the volume change during electrochemical cycling, contributing to both higher energy density and better cycling stability. Using these insights, we have identified four new PBA compositions - $Na_2CoMn(CN)_6$, $Na_2NiMn(CN)_6$, $Na_2CuMn(CN)_6$ and $Na_2ZnMn(CN)_6$ - that show great promise as aqueous Na-ion battery cathodes.

Chapter 2 is, in total, a reprint of the material "Water contributes to higher energy density and cycling stability of Prussian blue analogue cathodes for aqueous sodium-ion batteries." Chemistry of Materials 31, no. 15 (2019): 5933-5942. Xingyu Guo, Zhenbin Wang, Zhi Deng, Xiangguo Li, Bo Wang, Xi Chen, and Shyue Ping Ong. The dissertation author was the primary investigator and author of this scientific paper.

Appendix: Supplementary Information

Water Contributes to Higher Energy Density and Cycling Stability of Prussian Blue Analogue Cathodes for Aqueous Sodium-Ion Batteries

2.6 Spin Ordering Effect on phase stability of PBAs compounds

Table 2.3: Energy difference in spin-ordering between the ground state and the next lowest energy state by HSE functional.

Composition	ΔE (meV/atom)	Ground state	Second lowest energy state
$Na_2MnFe(CN)_6$	151.1	Mn: $t_{2g}^3e_g^2$, Fe: t_{2g}^6	Mn: t_{2g}^5, Fe: t_{2g}^6
$MnFe(CN)_6$	13.7	Mn: $t_{2g}^3e_g^1$, Fe: t_{2g}^5	Mn: t_{2g}^4, Fe: t_{2g}^5
$Na_2CoFe(CN)_6$	64.9	Co: $t_{2g}^5e_g^2$, Fe: t_{2g}^6	Co: $t_{2g}^6e_g^1$, Fe: t_{2g}^6
$NaCoFe(CN)_6$	121.9	Co: t_{2g}^6, Fe: t_{2g}^6	Co: $t_{2g}^5e_g^2$, Fe: t_{2g}^5
$CoFe(CN)_6$	98.9	Co: t_{2g}^6, Fe: t_{2g}^5	Co: $t_{2g}^4e_g^2$, Fe: t_{2g}^5
$Na_2FeFe(CN)_6$	76.2	Fe: $t_{2g}^4e_g2$, Fe: t_{2g}^6	Fe: t_{2g}^6, Fe: t_{2g}^6
$NaFeFe(CN)_6$	40.0	Fe: $t_{2g}^4e_g2$, Fe: t_{2g}^5	Fe: $t_{2g}^3e_g^2$, Fe: t_{2g}^6
$FeFe(CN)_6$	34	Fe: $t_{2g}^3e_g^2$, Fe: t_{2g}^5	Fe: t_{2g}^5, Fe: t_{2g}^5

2.7 Comparison of different functionals

Table 2.4: Ability of various functionals to reproduce the experimentally observed spin configurations of $Na_xMnFe(CN)_6$.

	Spin state		
	$MnFe(CN)_6$	$Na_2MnFe(CN)_6$	$Na_2MnFe(CN)_6{\cdot}2H_2O$
Exp.	Mn: $t_{2g}^3e_g^1$, Fe: t_{2g}^5 (5)	Mn: $t_{2g}^3e_g^2$, Fe: t_{2g}^6 (5)	Mn: $t_{2g}^3e_g^2$, Fe: t_{2g}^6 (5)
Failed functionals	GGA, PBEsol, SCAN, SCAN+rvv10 (Mn: t_{2g}^4, Fe: t_{2g}^5 (3))	None	PBEsol (Mn: t_{2g}^5, Fe: t_{2g}^6 (1))

Table 2.5: Calculated and experimental average voltages for PBA cathodes in wet electrolyte (a_{H_2O} =1))

Formula	Voltage (V vs Na/Na^+)		
	Exp.	HSE	SCAN+rvv10
$Na_2MnFe(CN)_6$	3.5/4.0[124]	3.34/3.58	2.48/3.13
$Na_2FeFe(CN)_6$	3.10/4.0[36]	3.03/3.48	2.2/4.95
$Na_2NiFe(CN)_6$	3.38[172]	3.37/4.43	4.05/4.73

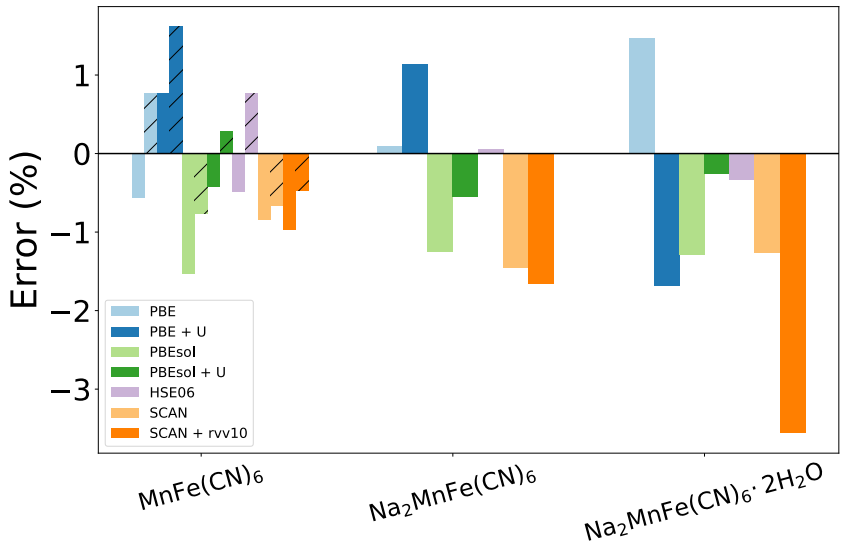

Figure 2.10: Error rate of the calculated lattice parameters of tetragonal $MnFe(CN)_6$, rhombohedral $Na_2MnFe(CN)_6$ and monoclinic $Na_2MnFe(CN)_6{\cdot}2H_2O$ with respect to experiments. The patterned ones are the lattice parameters along *c* axis of the calculated $MnFe(CN)_6$.

2.8 Calculated grand potential phase diagrams of $Na_xFeFe(CN)_6{\cdot}nH_2O$ and $Na_xNiFe(CN)_6{\cdot}nH_2O$ system

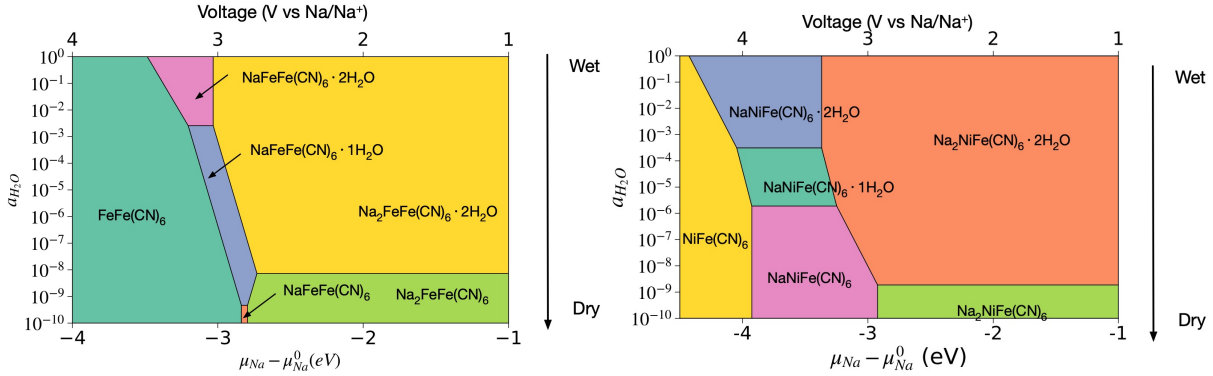

(a) (b)

Figure 2.11: Calculated grand potential diagram of (a) $Na_xFeFe(CN)_6{\cdot}nH_2O$ and (b) $Na_xNiFe(CN)_6{\cdot}nH_2O$.

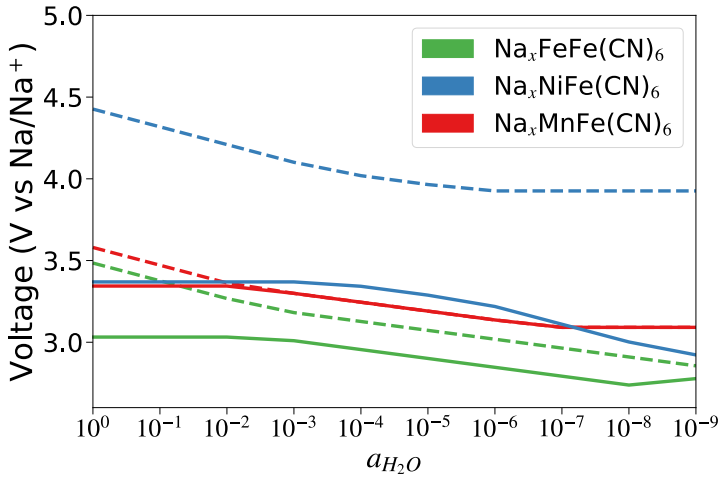

Figure 2.12: Predicted average voltages of as a function of activity of water in $Na_2MnFe(CN)_6$, $Na_2NiFe(CN)_6$, in $Na_2FeFe(CN)_6$ cathodes. Solid line: $1 \leq x \leq 2$; Dotted line: $0 \leq x \leq 1$.

2.9 Computed voltage as a function of activity of water

2.10 Effect of $Fe(CN)_6$ defect

We here investigated the phase stability of the $Fe_4[Fe(CN)_6]_3 \cdot nH_2O$ structures with n = 0, 6, 14. According to previous experimental observations[52], the initial defective structure of the $Fe_4[Fe(CN)_6]_3 \cdot nH_2O$ was constructed by removing one $Fe(CN)_6$ cluster from a $2 \times 2 \times 2$ supercell of cubic $FeFe(CN)_6$ structure. Two distinct types of water molecules, one fills the empty nitrogen sites of $Fe(CN)_6$ vacancies (H_2O_d) and the other occupies the interstitial positions in the lattice (H_2O_i), were inserted into the initial structure to mimic the hydrated $Fe_4[Fe(CN)_6]_3$.

2.11 Computed voltage as a function of activity of water

The calculated lattice parameters (Table 2.6) of dehydrated $Fe_4[Fe(CN)_6]_3$ overestimated the experimental result of 1.2%. The optimized $Fe_4[Fe(CN)_6]_3 \cdot 14H_2O$ crystal structure (Figure 2.13) is shown to be distorted from the cubic lattice due to the high concentration of $Fe(CN)_6$ defect and H2O molecules in the simulation cell. The position of the water molecules agrees with

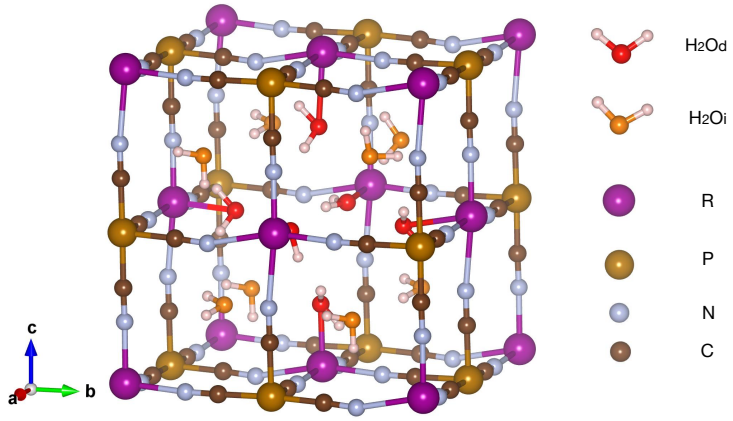

Figure 2.13: Crystal structure of DFT calculated $Fe_4[Fe(CN)_6]_3 \cdot 14H_2O$.

those reported in the literature.[52] While the lattice parameters of hydrated $Fe_4[Fe(CN)_6]_3$ is accurately predicted and the error rate are within 0.3%.

Table 2.6: DFT calculated and experimental lattice parameter of $Fe_4[Fe(CN)_6]_3$ and $Fe_4[Fe(CN)_6]_3 \cdot 14H_2O$.

Method	Composition	Space group	Lattice parameters (A)
Exp.	$Fe_4[Fe(CN)_6]_3$	$Fm\bar{3}m$	a = 10.13
	$Fe_4[Fe(CN)_6]_3 \cdot 14H_2O$		a = 10.155
HSE	$Fe_4[Fe(CN)_6]_3$	$Fm\bar{3}m$	a = 10.25
	$Fe_4[Fe(CN)_6]_3 \cdot 14H_2O$	P1	a = 10.156, b = 10.135, c = 10.179

Figure 2.14 shows the predicted relative stability of $Fe_4[Fe(CN)_6]_3 \cdot nH_2O$ with respect to water activity. We find that when being hydrated, water molecules first fill the empty nitrogen sites and then the interstitial sites in PBA lattice. In wet electrolyte (a_{H_2O}=1), the hydrated $Fe_4[Fe(CN)_6]_3$ is more stable than its dry counterpart. These results are in line with the experimental observations that $R(CN)_6$ defects introduces more water molecules into PBA lattice in wet electrolyte.

2.12 Computed pseudo-binary phase diagrams of the predicted compounds

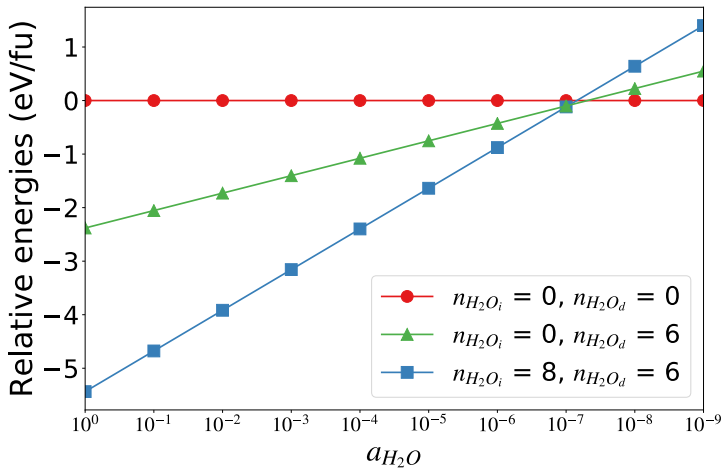

Figure 2.14: Predicted relative stability of $Fe_4[Fe(CN)_6]_3 \cdot nH_2O$ with respect to $Fe_4[Fe(CN)_6]_3$ as a function of the activity of water.

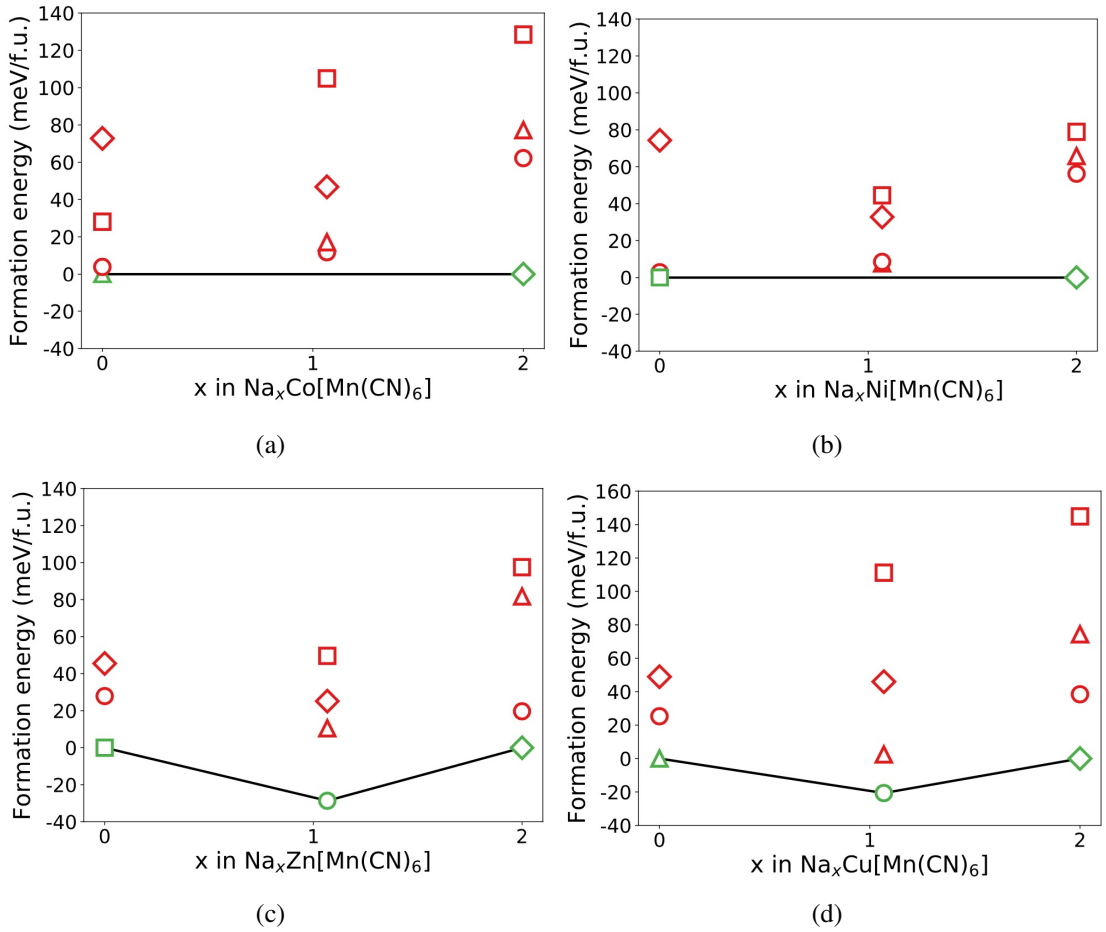

Figure 2.15: Computed pseudo-binary phase diagrams of the predicted compounds.

2.13 Integrated spin density of the predicted compounds

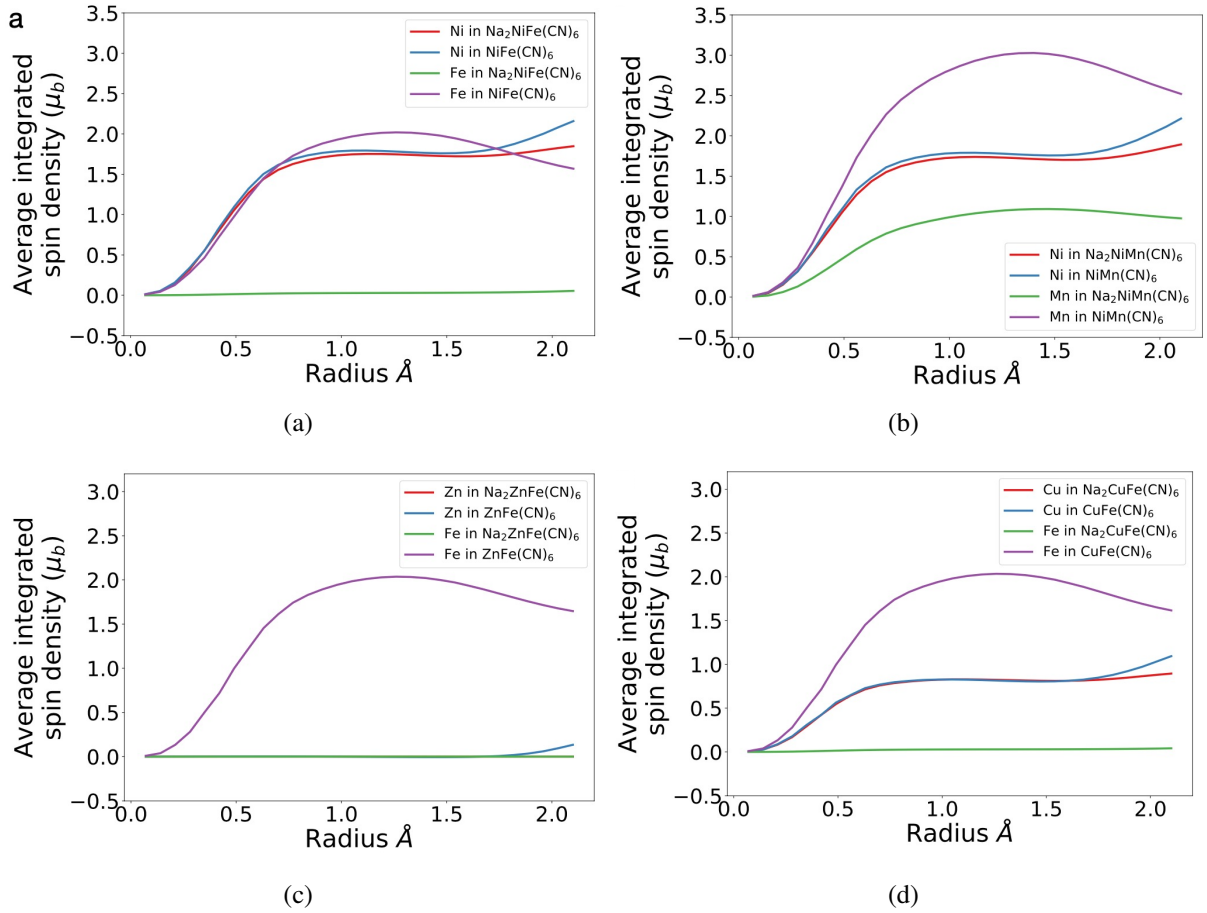

Figure 2.16: Average integrated spin density for P (R) as a function of radius from P (R), up to 2 Å.

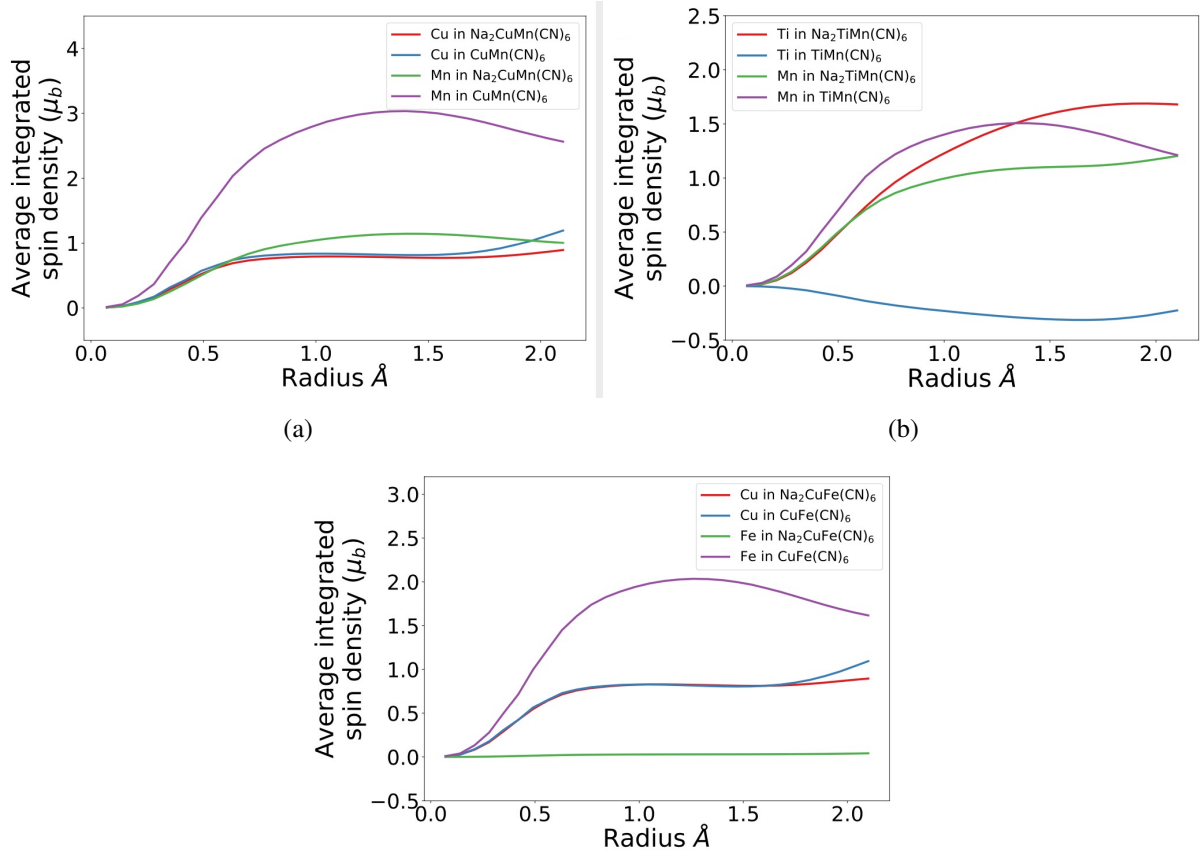

(a) (b)

(c)

Figure 2.16: (Continued) Average integrated spin density for P (R) as a function of radius from P (R), up to 2 Å.

2.14 Computed grand potential phase diagrams of the predicted compounds

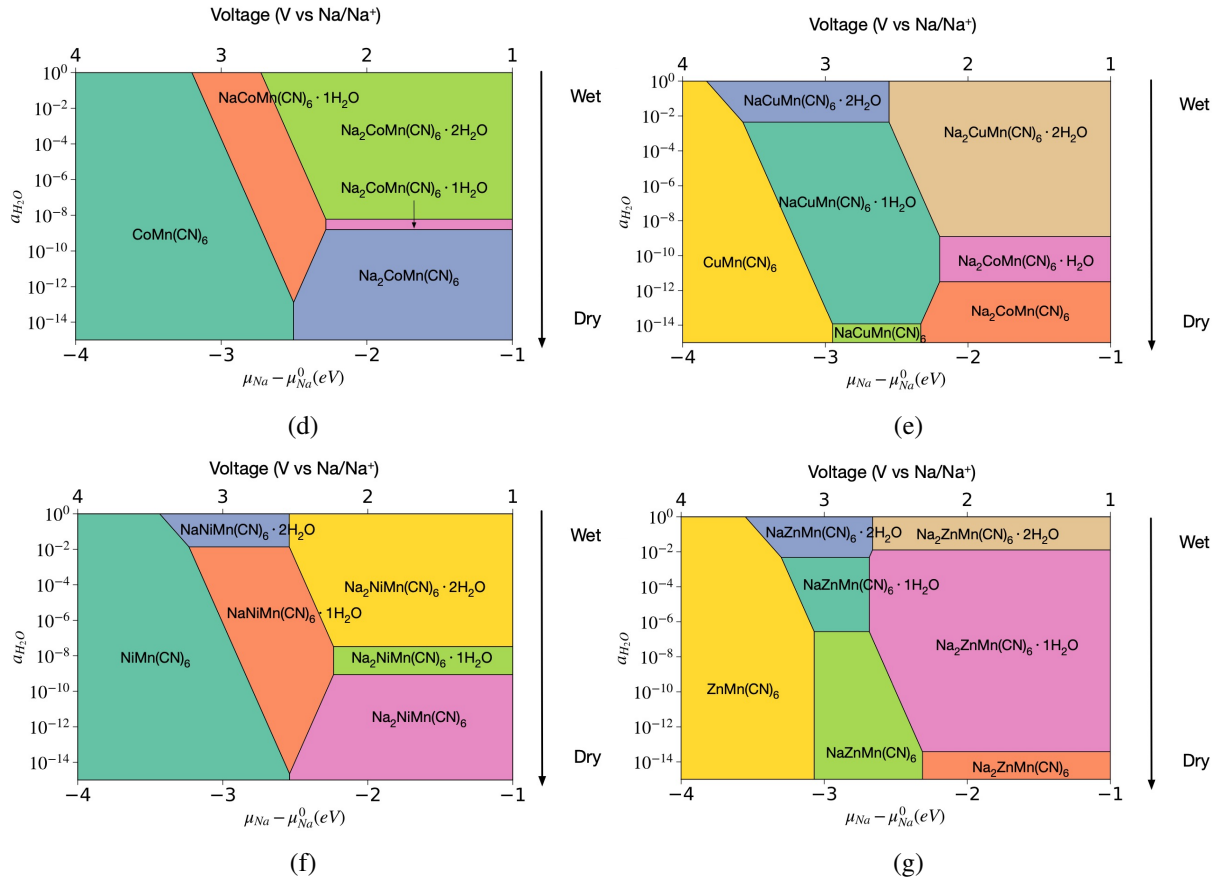

Figure 2.17: Computed grand potential phase diagram of the predicted compounds.

Chapter 3

Design Principles for Aqueous Na-ion Battery Cathodes

3.1 Introduction

Aqueous sodium-ion batteries (ASIBs) have recently gathered intensive interest for large-scale energy storage systems. [17, 74] Compared to non-aqueous batteries, the use of a non-flammable, inexpensive and environmentally-safe aqueous electrolyte in ASIBs not only offers high reliability, but also lowers the cost of manufacture and maintenance. The rapid ionic diffusion in the aqueous electrolyte, which is generally two to three orders of magnitude higher than that in a non-aqueous electrolyte, also enables high rate capability in ASIBs [70].

Much research effort has been directed toward the design of ASIBs cathodes with both higher energy densities and long term cycling stabilities. [17, 74] Figure 3.1 and Table 3.1 summarizes the main cathodes that have been studied for ASIB applications. They can be broadly categorized into four families:

1. **Mn oxides.** $Na_{0.44}MnO_2$ (Space group: *Pbam*) is among the most well-studied cathodes in ASIBs. Its electrochemical performance varies in different voltage ranges and electrolytes.

[174, 120, 169] While most Mn oxides exhibit capacitive behavior in aqueous electrolytes [142, 188, 7, 158, 135], $Na_{0.44}MnO_2$ exhibits consecutive biphasic reactions with Na^+ intercalation. [174] The inter-connected diffusion channels and the abundant vacancies in the structure facilitates Na^+ diffusion in the charge/discharge processes. [70]

2. **Natrium Super Ionic CONductor (NASICON).** The NASICON compounds have been extensively studied as SIBs cathodes due to their open framework, which enable facile Na^+ diffusion. [41] The general formula of NASICON is $Na_xMM^{'}(XO_4)_3$ and consists of a three dimensional framework of MO_6 and $M^{'}O_6$ octahedra sharing corners with XO_4 tetrahedra. $R\bar{3}c$-$Na_3V_2(PO_4)_3$ is the most widely investigated NASICON-type cathode in conventional SIBs [141]. Recently, $R\bar{3}c$-$Na_3VTi(PO_4)_3$ [166] and $Na_3MnTi(PO_4)_3$ [39] have also been investigated as electrodes in symmetric aqueous batteries and exhibits significantly improved long term cycling stability compared with $Na_3V_2(PO_4)_3$ [185].

3. **Fe phosphates.** Olivine-$NaFePO_4$, pyrophosphate-$Na_2FeP_2O_7$ and mixed anionic phosphate $Na_4Fe_3(PO_4)_2P_2O_7$ have been investigated as cathodes in ASIBs given the fact that average redox potential of Fe^{2+}/Fe^{3+} in phosphate compounds usually locates within the electrochemical stability window of aqueous electrolyte. [35, 65, 37].

4. **Prussian blue analogues (PBAs).** PBAs compounds, with a general chemical formula of $A_xP[R(CN)_6]_{1-y}\cdot nH_2O$ (A = alkali or alkaline ion, P and R = transition metals), have been demonstrated as excellent cathode materials for ASIBs because their open 3D framework enables fast ionic diffusion and superior cycling stability. [164] In particular, $K_{0.6}Ni_{1.2}Fe(CN)_6\cdot 3.6\,H_2O$ and $Na_{1.4}Cu_{1.3}Fe(CN)_6\cdot 8\,H_2O$ show great performance in aqueous electrolyte during electrochemical cycling of Na^+ ions. [173, 180]

Unlike cathodes in conventional sodium-ion batteries (SIBs), which usually operate at potential larger than 3.5 V vs Na/Na^+, cathodes in ASIBs must have working potentials within the evolution potential of O_2 and H_2 gas, i.e., $2.31 \sim 3.53$ V vs Na/Na^+ in neutral electrolyte.

Also, dissolution of electrodes and side reactions with the aqueous electrolyte, such as electrode materials reacting with H_2O/O_2 and proton intercalation into electrode materials, can adversely affect the long-term cycling stability of ASIBs. Possible strategies to mitigate these side reaction include coating the electrode, eliminating oxygen and adjusting the pH of the electrolyte. [101] However, the intrinsic instability of electrode materials in aqueous environment still leads to significant performance reduction of ASIBs. For example, Zhang et al. [185] found that the capacity of carbon-coated $Na_3V_2(PO_4)_3$ fades steadily from 94.5 mAh/g to about 10 mAh/g within only 30 cycles in 1M Na_2SO_4 electrolyte when being charged/discharged at rate of 10 C due to cathode dissolution. While first principles methods have been applied extensively to the study of battery materials [163], there have been relatively few computational studies of ASIB cathode materials, and most are focused on the PBA family. [182, 43]

In this work, we derive design rules by benchmarking first principles predictions of the working potential and aqueous stability on representative ASIB cathode materials. The scope includes all cathodes tabulated in Table 3.1, with the exception of the PBAs as these have been studied extensively previously and possible water co-intercalation in these systems complicate their analysis [43]. We then apply these design rules to the high-throughput screening of known SIB cathode materials for application in aqueous electrolytes, identifying several hitherto-unexplored candidates for further exploration.

3.2 Methods

3.2.1 Density functional theory calculations

All spin-polarized density functional theory (DFT) calculations were performed using the Vienna *ab initio* simulation (VASP) package within the projected-augmented wave method. [81, 19] The exchange-correlation functional used for structural relaxation and energy calculations was the Perdew-Burke-Ernzerhof (PBE) generalized gradient approximation (GGA) functional

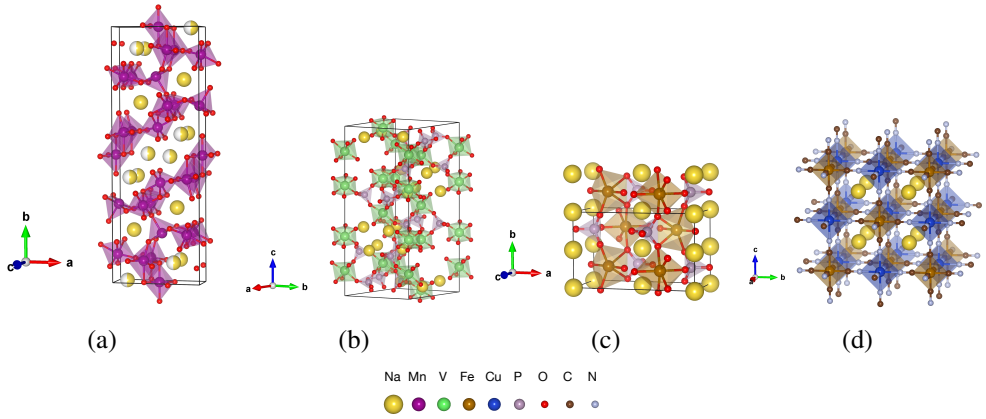

Figure 3.1: Crystal structures of representative ASIB cathodes. (a) $Na_{0.44}MnO_2$ (b) NASICON: $Na_3V_2(PO_4)_3$, (c) Fe-based phosphates: $NaFePO_4$ (d) PBAs: cubic $Na_2FeCu(CN)_6$

.

Table 3.1: Electrochemical properties of representative cathodes for ASIBs

Formula	Working Potential (V vs Na/Na^+)	Electrolyte (pH)	Current rate	Capacity (mAh/g)	Cycling voltage range (V vs Na/Na^+)	Retention(%) /Cycles	Ref
$Na_{0.44}MnO_2$	2.00 - 3.50	1 M $NaClO_4$ in 1:2 EC/DMC	5C	128	2.0 - 4.0	77/1000	24
$Na_{0.44}MnO_2$	3.35 - 3.60	1 M Na_2SO_4 (7)	4C	45	3.35 - 3.60	100/1000	174
$Na_{0.44}MnO_2$	2.91 - 3.41	1 M Na_2SO_4 (7)	2C	47	2.84 – 3.59	88/200	120
$Na_{0.44}MnO_2$	2.46 - 2.76	1 M Na_2SO_4 (13.5)	2C	32	2.31 – 2.91	100/400	169
$Na_3V_2(PO_4)_3$	3.4	1 M $NaClO_4$ in 1:2 EC/DMC	10C	106	2.3 - 3.9	84.9/1000	141
$Na_3V_2(PO_4)_3$	3.4	1 M Na_2SO_4 (7)	8.5C	209 (F/g)	2.91 – 3.84	32/30	150
$Na_2VTi(PO_4)_3$	3.33	1 M Na_2SO_4 (7)	5C	51	2.91 - 3.51	92/500	166
$Na_2VTi(PO_4)_3$	2.16	1 M Na_2SO_4 (7)	5C	50	2.11 - 2.91	94/500	166
$Na_3MnTi(PO_4)_3$	2.12 - 4.01	1 M $NaClO_4$ in 1:1 EC/PC + 5% FC	2C	119	1.5 - 4.0	92/500	190
$Na_3MnTi(PO_4)_3$	2.14 – 3.54	1 M Na_2SO_4 (7)	1C	56.5	2.14 – 3.54	98/100	39
$Na_2FeP_2O_7$	2.52 - 3.24	1 M $NaClO_4$ in PC	C/20	90	2.0 - 4.5	100/80	72
$Na_2FeP_2O_7$	2.50 - 3.30	aqueous electrolyte	1C	65	2.75 – 3.65	86/300	65
$NaFePO_4$	3.48	1 M $NaClO_4$ in 98:2 PC/FEC	C/20	125	2.2 - 4.3	90/50	112
$NaFePO_4$	2.55 - 3.2	1 M Na_2SO_4 (7)	1C	70	2.45 - 3.3	90/30	35
$Na_4Fe_3(PO_4)_2P_2O_7$	2.75 - 3.25	1 M $NaClO_4$ in EC/PC	1C	99	1.8 - 4.3	90/50	37
$Na_4Fe_3(PO_4)_2P_2O_7$	2.50 - 3.25	1 M Na_2SO_4 (6)	1C	84	2.5 - 3.4	74/50	37
$K_{0.6}Ni_{1.2}Fe(CN)_6$	3.30	1 M $NaNO_3$ (2)	8.3C	51	-	100/5000	173
$Na_{1.4}Cu_{1.3}Fe(CN)_6$	3.52	Na_2SO_4	5C	57	-	93/500	180

[127] with a Hubbard U [34] applied for $3d$ transition metals. The U parameters used were similar to those from the Materials Project [62]. For Ti and V containing compounds, calculations were also performed using the screened hybrid Heyd-Scuseria-Ernzerhof (HSE) functional [55, 40] and the strongly constrained and appropriately normed (SCAN) functional [151]. The energy cutoff of plane wave was 520 eV, and the k-point density was at least 1000/(number of atoms in the cell). All calculations were performed in a ferromagnetic configuration, initialized with low spin for Co and high spin for all other transition metals. All crystal structure manipulations, input/output file generation and data analysis were performed using the Python Materials Genomics (pymatgen) package [118].

3.2.2 Voltage profile

The average intercalation potential of Na into a host X vs Na/Na$^+$ was calculated by the equation [9]:

$$V = -\frac{E_{DFT}(\mathrm{Na_nX}) - E_{DFT}(\mathrm{Na_{n-x}X}) - xE_{DFT}(\mathrm{Na})}{xe} \tag{3.2.1}$$

where $E_{DFT}(\cdot)$ denotes the DFT calculated total energy, and e is the electron charge. In this work, the average voltage was calculated based on a one-electron-per-transition-metal redox reaction for all materials.

The voltage profiles were constructed by using all stable phases from the pseudobinary phase diagram of the sodiated and desodiated compounds (Figure 3.12), obtained using the convex hull construction [114]. All the initial sodiated structures were obtained either from the Materials Project [62] or ICSD database [16]. All the partially desodiated structures were determined by enumerating all symmetrically distinct orderings in sufficiently large supercells using the adaptor to the enumlib library [44] in pymatgen [118]. For each composition, at least 20 lowest electrostatic energy (computed via the Ewald summation method) configurations were selected for the convex hull construction.

3.2.3 Pourbaix diagram

Pourbaix diagrams were computed using the formalism developed by Persson et al. [130], which combines *ab initio* calculated solid phases with experimental aqueous reference states. In a chemical system M, the Pourbaix stable domains are determined based on the knowledge of all possible equilibrium redox reactions in M-O-H chemical space. For the following reaction in an aqueous medium at a given $pH = -log[H^+]$:

$$[Reactants] + \mathrm{H_2O} = [Products] + \mathrm{mH^+} + \mathrm{ne^-} \tag{3.2.2}$$

the Nernst equation,

$$-nFE = \Delta \mathrm{G_r} = \Delta \mathrm{G_r}^0 + 2.303 \times RT \times log\frac{[Reactants]}{[Products]} - 2.303 \times RT \times m \times pH \tag{3.2.3}$$

can be used to relate the external potential, E, to the change of the Gibbs free energy of the reaction, ΔG_r. $\Delta \mathrm{G_r}^0$ denotes the Gibbs free energy change of the reaction under standard state, F is the Faraday constant, R is the gas constant, and T is the temperature. Thus, the most stable species in aqueous environment can be determined by minimizing ($\Delta G_r + nFE$) across all possible reactions for a given pH and E.

The meta-stability of a cathode was evaluated by computing its Gibbs free energy difference (ΔG_{pbx}) with respect to the stable domains on Pourbaix diagram as a function of pH and potential (E) [136, 147]. The focus of this work is on the potential range from -2 V to 2 V versus the standard hydrogen electrode (SHE) and the pH range from 0 to 14. Unless otherwise stated, the concentration of Na^+ ion is set at 1M, and the concentrations of all other ions are set at 10^{-6} M, which are typical operating conditions for ASIBs. It should be noted that the number of non-H/O atoms are conserved in the phase transformations between cathodes and stable species in aqueous environment. Hence, ΔG_{pbx} is normalized by the total number of non-H/O atoms with

units of eV/cation.

3.2.4 Diffusion barriers

The sodium vacancy migration barriers were calculated using the climbing image nudged elastic band (CI-NEB) method [51, 50]. Here, the PBE functional without Hubbard U was adopted to avoid the possible mixing of the diffusion barrier with a charge transfer barrier. [116] The force convergence criterion was 0.05 eV/Å.

3.3 Results

3.3.1 Screening workflow

Our proposed screening workflow for ASIB cathodes given in Figure 3.2. For operation in aqueous environments, a cathode must satisfy the following criteria:

1. **Suitable working potential within the H_2 and O_2 evolution potential range (e.g. 2.31 $\sim$ 3.53 V vs Na/Na$^+$ in neutral solution).** For practical energy densities, the average working potential in literature is typically higher than 3V vs Na/Na$^+$ in neutral electrolyte (Table 3.1).

2. **High aqueous stability.** Within the potential range of interest, a cathode with low ΔG_{pbx} and form solid phases in decomposition products on Pourbaix diagram tends to exhibit superior long-term cycling stability. Based on previous work by Singh et al. [147] on photoanodes, a $\Delta G_{pbx} < 0.5$ eV/cation (ideally 0 eV/cation) indicates low reactivity in aqueous environments.

In addition to the above criteria, any cathode (for ASIBs or otherwise) must also be synthesizable and have relatively high Na$^+$ diffusivity for high rate capability. [116, 47] The synthesizability of a material is computationally estimated by its energy above the linear combination

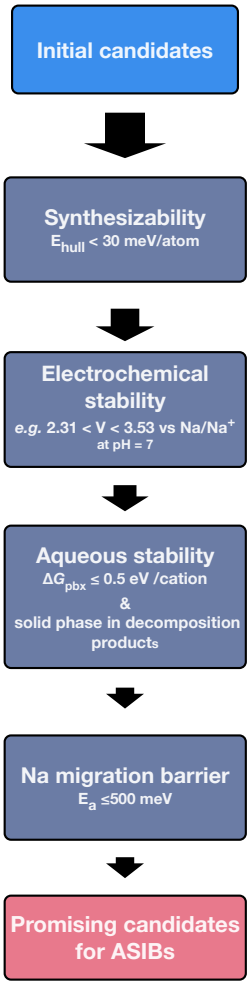

Figure 3.2: Screening workflow for high-performance ASIB cathodes

of stable phases in the DFT calculated 0K phase diagram (E_{hull}). [114] Stable phases have zero E_{hull}, and the higher its E_{hull}, the more unstable a phase is. A typical E_{hull} threshold of 30 - 50 meV/atom was used to identify synthesizable materials in previous high-throughput screening works. [47, 170] The potential for high ionic conductivity can be estimated by computing the Na ion migration barriers(E_a) for percolating Na diffusion pathways using NEB calculations. In conventional SIB cathodes, the predicted E_a values in facile Na^+ diffusion pathways are generally less than 500 meV [10].

It should be noted that the criteria were established based purely on thermodynamic considerations; kinetic factors can contribute to stabilization of the materials in aqueous environments. For example, the electrochemical stability window of the aqueous electrolyte is usually slightly larger than 1.23 V due to overpotentials. [108] Kinetic barriers (to ion diffusion for instance) may also retard cathode dissolution. While these kinetic factors are difficult to directly compute, they can be accounted for by relaxation of the thermodynamic thresholds for screening purposes. Also, we only explore the aqueous stability of bulk cathodes in this work, while surface/interface effects and particle size may have an influence on the electrochemical properties of cathodes in ASIBs. For example, nanostructured electrodes may exhibit better performance in terms of facile ion/electron transport, reduced changes of the electrodes and increased utilization of active materials during charge/discharge processes, but increased surface/interface area may also result in destabilization of the electrode in aqueous solutions. [5, 153]

We will first benchmark the DFT computed working potentials and ΔG_{pbx} for the seven well-known ASIB cathodes in Table 3.1 (excluding the PBAs).

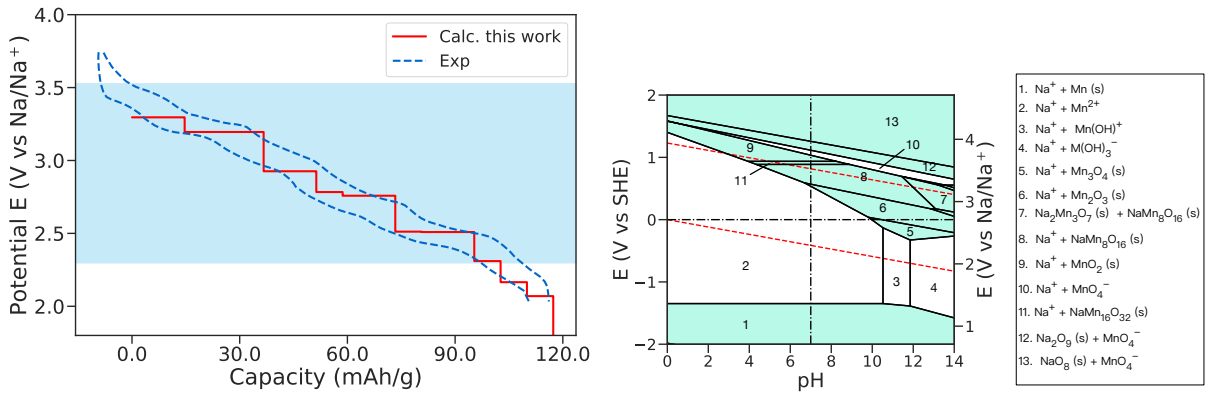

(a) (b)

Figure 3.3: (a) Calculated voltage profile of Na_xMnO_2 ($x = 0.22 - 0.66$). The electrochemical stability windows at pH = 7 are shaded blue. The experimental voltage profile is from ref 71. (b) Calculated Pourbaix diagram of $Na_{0.44}MnO_2$. Regions containing solid phases are shaded green.

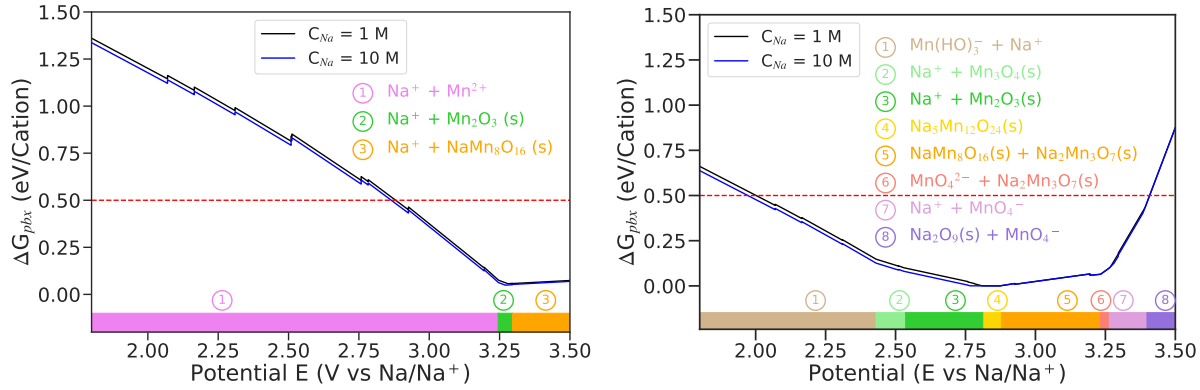

(a) pH = 7 (b) pH = 13.5

Figure 3.4: ΔG_{pbx} of Na_xMnO_2 as a function of potential (E) in (a) neutral (pH = 7) and (b) basic (pH = 13.5) aqueous electrolytes. Red dashed line indicates the limit of $\Delta G_{pbx} = 0.5$ eV/cation for materials to be stable in aqueous electrochemical environments [147].

3.3.2 Voltage and aqueous stability of known ASIB cathodes

$Na_{0.44}MnO_2$

Figure 3.3(a) shows the calculated voltage profile of Na_xMnO_2, which exhibits nine plateaus within the voltage range of 2 $\sim$ 3.3 V vs Na/Na^+. The computed profile and voltages are in good agreement with experimental observations [71]. In neutral electrolyte (pH = 7), the cathode can be cycled within the potential range of 2.31 $\sim$ 3.53 V vs Na/Na^+ (blue region) with a theoretical capacity of 100 mAh/g, while in a basic electrolyte (pH = 13.5)(orange region in Figure 3.13), the electrochemical window shifts to 1.91 $\sim$ 3.14 V vs Na/Na^+ with a smaller theoretical capacity of 80 mAh/g.

Figure 3.3(b) shows the computed Pourbaix diagram of $Na_{0.44}MnO_2$, which plots the stable species in the Na-Mn-O-H system with a Na/Mn ratio of 0.44:1 under various pH and potential. In regions within the electrochemical window of aqueous electrolytes, Na forms Na^+ ion in most regions. Mn is stable in alkaline environment at high potential (e.g. $E > 0.17$ V vs SHE at pH = 7) by forming manganese oxides while Mn^{2+} ion forms in acidic conditions (pH $<$ 4) or low potential regions. It may be observed that the solid phase $Na_{0.44}MnO_2$ does not appear in any region on the Pourbaix diagram, which suggests that it is thermodynamically metastable in an aqueous reservoir. It should be noted, however, that $Na_{0.44}MnO_2$ is a stable phase ($E_{hull} = 0$) on the non-aqueous Na-Mn-O phase diagram.

The aqueous stability of Na_xMnO_2 cathode during the cycling process was evaluated by computing ΔG_{pbx} as a function of potential in different electrolytes (pH and Na concentration). In a neutral electrolyte (Figure 3.4(a)), when being charged at high potential of 3.30 $\sim$ 3.50 V vs Na/Na^+, Na^+ ions and solid $NaMn_8O_{16}$ forms, and the ΔG_{pbx} of Na_xMnO_2 is less than 0.1 eV/cation. With Na^+ intercalating into the host structure, solid Mn_2O_3 along with Na^+ ions become more stable on Pourbaix diagram, and the ΔG_{pbx} of Na_xMnO_2 slightly increases. As the potential decreases to below 3.25 V vs Na/Na^+, the ΔG_{pbx} dramatically increases and reaches 1.0

eV/cation at 2.31 V vs Na/Na^+. In these potential regions, Na_xMnO_2 fully decomposes into Na^+ and Mn^{2+}.

In contrast, Na_xMnO_2 is predicted to be more stable in a basic electrolyte (Figure 3.4(b)), with relatively smaller ΔG_{pbx} (< 0.5 eV/cation) within $2.0 \sim 3.14$ V vs Na/Na^+. Similarly, the small ΔG_{pbx} is coupled with the formation of all solid phases on Pourbaix diagram within the potential range of $2.81 \sim 3.14$ V vs Na/Na^+. $Na_{0.42}MnO_2$ becomes stable within $2.81 \sim 2.87$ V vs Na/Na^+ in aqueous electrolytes with $\Delta G_{pbx} = 0$ eV/cation. In addition, ΔG_{pbx} starts to increase as solvated ion species become stable when potential is lower than 2.81 V vs Na/Na^+.

The change of ΔG_{pbx} with potential can be related to the cycling stability of $Na_{0.44}MnO_2$ cathode observed in experiments [120, 169, 174]. For example, in a neutral electrolyte (1M Na_2SO_4 with pH = 7), the capacity of a $Na_{0.44}MnO_2$/activated carbon cell shows no sign of decay after 1000 cycles when cycled within $3.35 \sim 3.60$ V vs Na/Na^+, whereas, a significant capacity fading was observed at lower potentials (< 3.35 V vs Na/Na^+) [174]. Pang et al. [120] also observed a 88% retention of the initial cycling after 200 cycles within the potential range of 2.91 ~ 3.41 V vs Na/Na^+. In our calculations, the ΔG_{pbx} of Na_xMnO_2 at potential larger than 3.35 V vs Na/Na^+ is lower than 0.1 eV/cation and solid phase $NaMn_8O_{16}$ forms in decomposition products. While the measured slightly lower cycling stability within lower potential ranges can be anticipated due to larger ΔG_{pbx} and the formation of all ion phases on Pourbaix diagram when $E < 3.25$ V vs Na/Na^+. In a basic electrolyte (1 M Na_2SO_4 with pH = 13.5), a stable capacity of 32 mAh/g was achieved with no significant capacity reduction after 400 cycles at 2C rate when cycled within $2.31 \sim 2.91$ V vs Na/Na^+ [169]. The stable cycling stability in basic electrolytes is inline with the low computed ΔG_{pbx} (< 0.2 eV/cation) and the formation of solid phases in decomposition products in this voltage range.

We also find that in regions where Na^+ ions are stable, increasing the concentration of Na^+ ions slightly decreases the dissolution tendency of electrodes by $\sim 0.0591 \log C_{Na^+}$ eV/Na (Figure 3.4).

3.3.3 NASICON electrodes

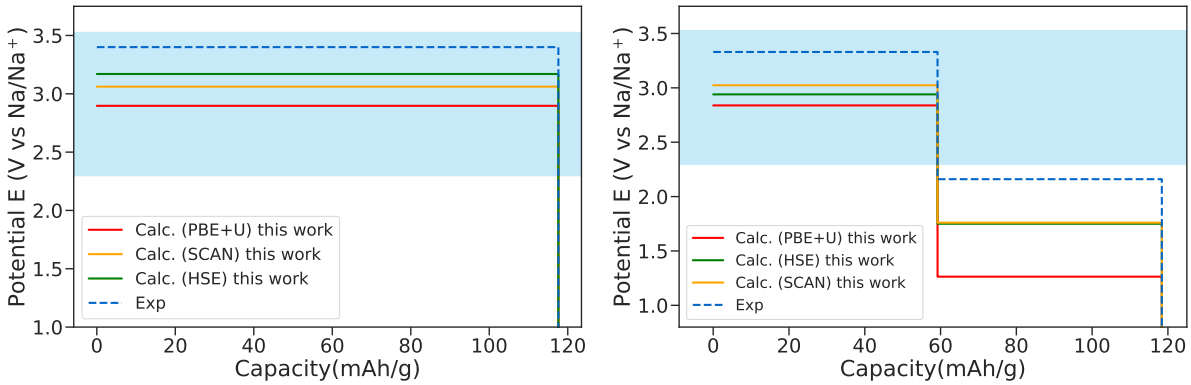

(a) (b)

Figure 3.5: Voltage profile of (a) $Na_xV_2(PO_4)_3$ ($x = 1-3$) and (b) $Na_xTiV(PO_4)_3$ ($x = 1-3$) cathode. The electrochemical stability window at pH = 7 is shaded blue. The experimental voltage profile is from ref 141 and ref 166, respectively.

Figures 3.5(a) and (b) present the calculated voltage profiles of the $Na_xV_2(PO_4)_3$ and $Na_xTiV(PO_4)_3$, respectively. In all cases, the voltages are substantially underestimated relative to experimental values, [166, 141] similar to previous DFT results on the NASICON systems. [116] While the use of the HSE and SCAN functional does substantially increase the voltage of the lower redox couples, they remain far below the experimental value. We therefore adopted the experimental redox potentials as electrochemical window of interest in the following aqueous stability analysis.

Figures 3.6(a) and 3.7(a) show the calculated Pourbaix diagram of $Na_3V_2(PO_4)_3$ and ΔG_{pbx} at pH = 7, respectively. From Figure 3.6(a), V forms solid vanadium oxides in low voltage regimes (e.g. < 0 V vs SHE at pH = 7). With an increase in the external potential, V in higher oxidation states becomes more stable as VO^{n-} ions. At pH = 7, ΔG_{pbx} increases with increase of potential and reaches 0.65 eV/cation at 3.37 V vs Na/Na^+, (Figure 3.7(a)) which is equal to the experimental redox potential of V^{3+}/V^{4+}. Thus, the observed capacity fading of $Na_3V_2(PO_4)_3$ cathode in 1M Na_2SO_4 neutral electrolyte [185] can be anticipated by the large ΔG_{pbx} and the decomposition into non-solid phases when cycled within $2.7 \sim 3.6$ V vs Na/Na^+.

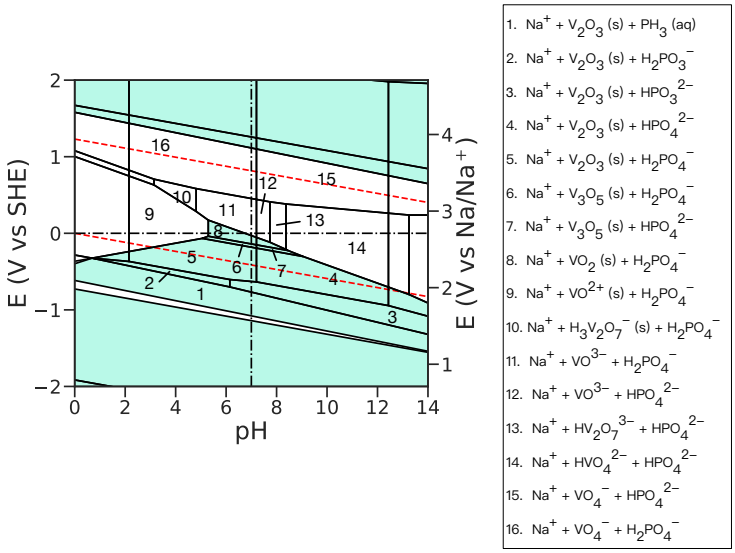

(a) Calculated Pourbaix diagram of $Na_3V_2(PO_4)_3$

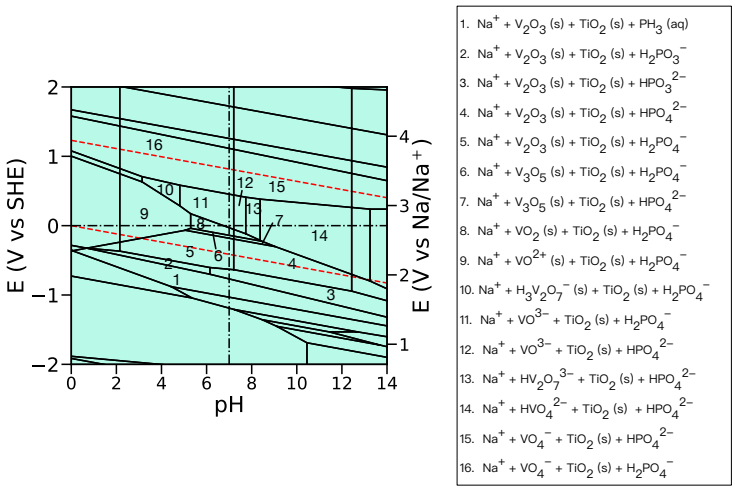

(b) Calculated Pourbaix diagram of $Na_2TiV(PO_4)_3$

Figure 3.6: Calculated Pourbaix diagram of (a) $Na_3V_2(PO_4)_3$ and (b) $Na_2TiV(PO_4)_3$. Regions containing solid phases are shaded green.

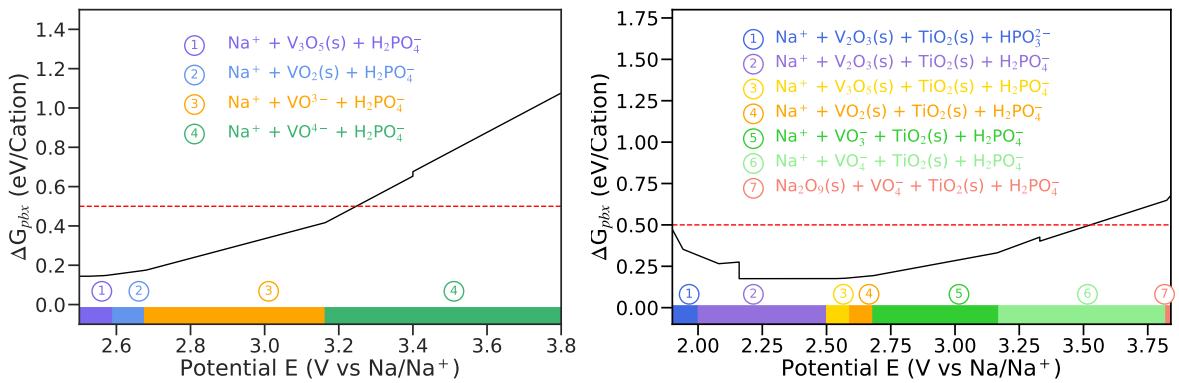

(a) (b)

Figure 3.7: ΔG_{pbx} of (a) $Na_xV_2(PO_4)_3$ and (b) $Na_xTiV(PO_4)_3$ as a function of potential (E) in neutral aqueous electrolyte (pH = 7). Red dashed line indicates the limit of $\Delta G_{pbx} = 0.5$ eV/cation for materials to be stable in aqueous electrochemical environments [147].

Compared with $Na_3V_2(PO_4)_3$, the introduction of Ti in $Na_2TiV(PO_4)_3$ leads to the formation of TiO_2 solid phases within the voltage range of 2.0 $\sim$ 3.8 V vs Na/Na$^+$ on Pourbaix diagram (Figure 3.6(b)). In a neutral electrolyte, ΔG_{pbx} of $Na_2TiV(PO_4)_3$ increases from 0.17 to 0.42 eV/cation as the potential is increased from 2.16 to 3.33 V vs Na/Na$^+$. With continued increase of potential, a biphasic reaction occurs from $Na_2TiV(PO_4)_3$ to $NaTiV(PO_4)_3$. Then the ΔG_{pbx} reaches 0.5 eV/cation at 3.53 V vs Na/Na$^+$. Unlike $Na_3V_2(PO_4)_3$ cathode, which exhibits severe capacity fading in ASIBs [185, 150], $Na_2TiV(PO_4)_3$ shows excellent cycling performance in 1M Na_2SO_4 aqueous electrolyte (pH = 7) with greater than 90% retention of its initial capacity after 500 cycles when cycled within 2.11 $\sim$ 3.51 V vs Na/Na$^+$ [166]. Both the lower ΔG_{pbx} of $Na_xTiV(PO_4)_3$ as well as the formation of solid TiO_2 in the high potential region may contribute to suppression of V dissolution. Similar results were also observed for $Na_3MnTi(PO_4)_3$ electrodes (Figure 3.14), which exhibits stable electrochemical performance experimentally. [39]

3.3.4 Fe-based phosphates

Figures 3.8(a)-(c) present the calculated voltage profile of three Fe-based cathode materials. Here, we consider the voltage profile operating on the Fe^{2+}/Fe^{3+} couple only; even though

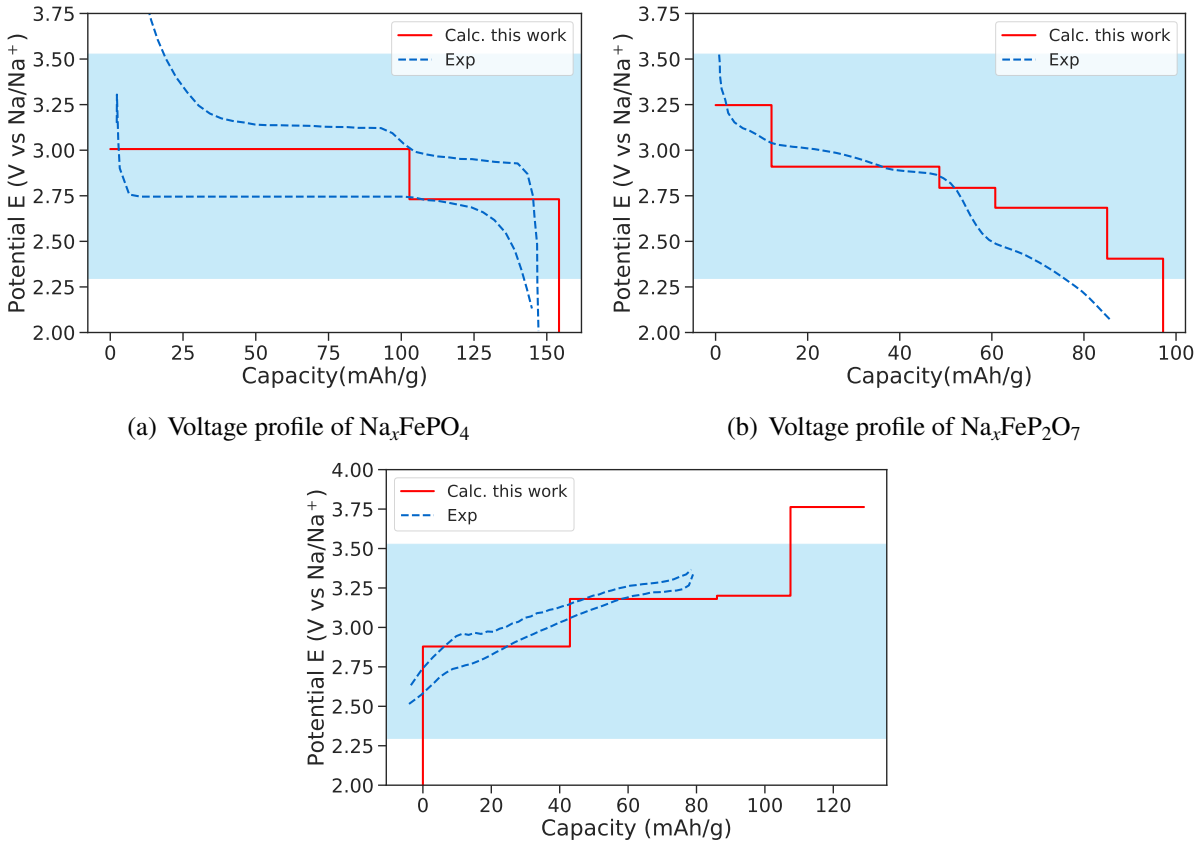

(a) Voltage profile of Na_xFePO_4

(b) Voltage profile of $Na_xFeP_2O_7$

(c) Voltage profile of $Na_xFe_3(PO_4)_2P_2O_7$

Figure 3.8: Calculated voltage profiles of (a) olivine-Na_xFePO_4 ($x = 0-1$)(b) $Na_xFeP_2O_7$ ($x = 1-2$) and (c) $Na_xFe_3(PO_4)_2P_2O_7$ ($x = 1-4$) cathode; The experimental voltage profiles are from ref 35, ref 65 and ref 37, respectively. The electrochemical stability window at pH = 7 is shaded blue.

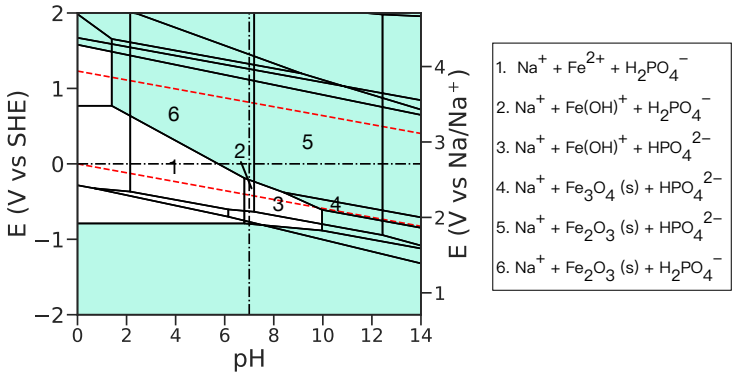

(a) Calculated Pourbaix diagram of $NaFePO_4$

Figure 3.9: Calculated Pourbaix diagram of $NaFePO_4$ Regions containing solid phases are shaded green.

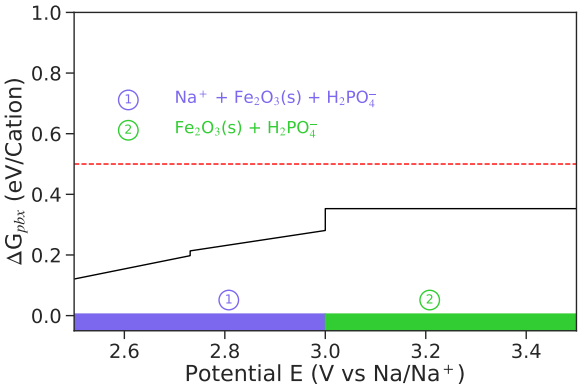

(a) ΔG_{pbx} vs E of Na_xFePO_4

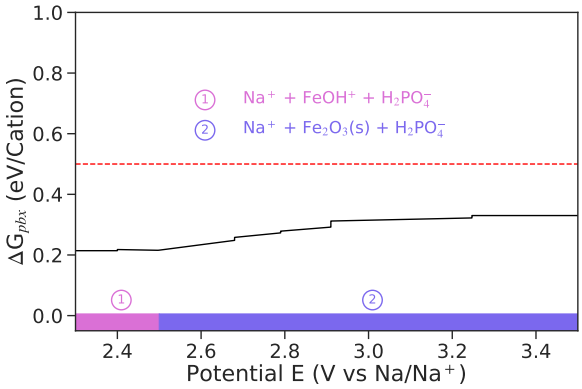

(b) ΔG_{pbx} vs E of $Na_xFeP_2O_7$

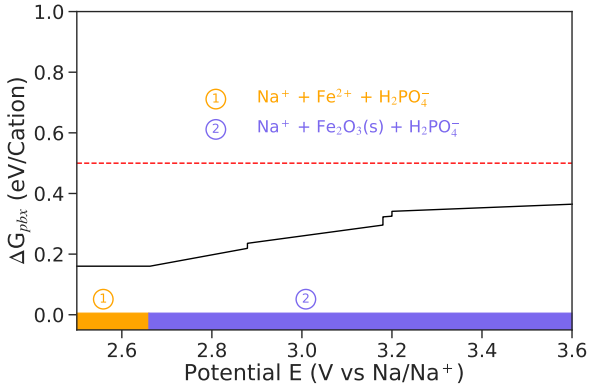

(c) ΔG_{pbx} vs E of $Na_xFe_3(PO_4)_2P_2O_7$

Figure 3.10: ΔG_{pbx} of (a) Na_xFePO_4, (b) $Na_xFeP_2O_7$ and (c) $Na_xFe_3(PO_4)_2P_2O_7$ as a function of potential in neutral aqueous solution (pH = 7 for (a)(b) and pH = 6 for (c)). Red dashed line indicates the limit of $\Delta G_{pbx} = 0.5$ eV/cation for materials to be stable in aqueous electrochemical environments [147].

additional Na can potentially be removed from $Na_2FeP_2O_7$ and $Na_4Fe_3(PO_4)_2(P_2O_7)$ to access the Fe^{3+}/Fe^{4+} couple, the voltages are far too high for ASIBs. All the three cathodes exhibits voltages within the electrochemical stability window of aqueous electrolyte (pH = 7) related to the Fe^{2+}/Fe^{3+} redox couple, and thus are able to deliver large capacities in ASIBs. Olivine-$NaFePO_4$ and $Na_2FeP_2O_7$ have theoretical capacities of 154.2 mAh/g and 97.2 mAh/g, respectively, in aqueous electrolyte, which are in good agreement with the experimentally achieved capacities. $Na_4Fe_3(PO_4)_2P_2O_7$ has a theoretical capacity of 129.0 mAh/g, but its final voltage plateau lies close to the oxygen evolution potential and therefore may not be accessible experimentally.

Figure 3.9(a) shows the Pourbaix diagram of olivine-$NaFePO_4$ cathode. Within the electrochemical stability window of aqueous electrolyte, Fe forms solid Fe_2O_3 in most regions (e.g. E > -0.2 V vs SHE at pH = 7). In the low potential region (near the H_2 gas evolution potential), Fe^{2+}, $Fe(OH)^+$ and solid Fe_3O_4 are stable in acidic, neutral and alkaline electrolyte, respectively. P forms $H_xPO_y^{n-}$ ions within the water splitting window in aqueous environment and does not affect the formation of Fe and Na-based stable species on Pourbaix diagram. Similar observations can be made in the Pourbaix diagrams of $Na_2FeP_2O_7$ and $Na_4Fe_3(PO_4)_2P_2O_7$ (Figures 3.15(a) and (b), respectively).

All three cathodes exhibit low ΔG_{pbx} ($\leq$ 0.32 eV/cation) in the range of their working potential and a solid phase of Fe_2O_3 forms in high potential regions (> 2.67 V vs Na/Na^+) in a neutral electrolyte (Figure 3.10(a)-(c)). Both the olivine- $NaFePO_4$ and $Na_2FeP_2O_7$ cathodes exhibit stable cycling behaviors in experiments [35, 65]. For $Na_4Fe_3(PO_4)_2P_2O_7$, Fernández-Ropero et al. [37] detected a small component of dissolved Fe (0.1%) along with a thin layer of solid Fe_3O_4 after immersing the sample in 1M Na_2SO_4 solutions (pH = 6) for 72h. Furthermore, the oxidation of electrodes in aqueous solution was confirmed by PXRD and ICP analysis after the stability tests and the authors ascribed its modest cycling stability to the oxidation and dissolution of electrode materials.

3.4 Screening for new ASIB cathodes

The screening workflow in Figure 3.2 was applied to well-known cathodes in the following chemistries:

1. **Phosphates.** Phosphate-based electrodes are known for their stable open frameworks and high working potential due to the strong covalent bonding and inductive effect of the phosphate anion [47]. The following compounds were selected: NASICON-$Na_3Me_2(PO_4)_3$ (Me = Fe, V) [137, 185], olivine-$NaMePO_4$ (Me = Fe) [35]; pyrophosphate $Na_2MeP_2O_7$ (Me = Mn, Fe, Co) [65, 12, 75]; mixed anion phosphates $Na_4Me_3(PO_4)_2P_2O_7$ (Me = Fe, Mn, Co, Ni) [37, 104]; alluaudite $Na_2Me_3(PO_4)_3$ (Me = Fe) [59]; α- and β-$NaVOPO_4$ [148, 48].

2. **Carbonophosphates.** The sidorenkite $Na_3Me(CO_3)(PO_4)$ was first proposed by Hautier et al. [45] from high-throughput calculation as potential cathode materials for Na-ion batteries. Among the predicted structures, $Na_3Mn(CO_3)(PO_4)$ and $Na_3Fe(CO_3)(PO_4)$ have been successfully synthesized and investigated as cathodes in Na ion batteries with high capacity [28, 58].

3. **Sulphates.** A new alluadite $Na_2Me_2(SO_4)_3$ (Me = Fe) was reported as an SIB cathode with high redox potential (3.8 V vs Na/Na^+) and Na ion conductivity. [13]

4. **Oxyfluorides.** Oxyfluorides have the potential to enable cathodes with high working potential due to the highly electronegative fluoride anion. The oxyfluorides investigated in this work include Pbcn - Na_2MePO_4F (Me = Fe, Co) [69, 83], $P2_1/c$ - Na_2MePO_4F (Me = Mn) [189], $Pna2_1$ - $NaVPO_4F$ [100] and $Na_3(VO_x)_2(PO_4)_2F_{3-2x}$ (x = 0, 1) [123].

Figure 3.11 summarizes the aqueous electrochemical properties of all compounds investigated. It may be observed that the average redox potential of Co and Ni-based phosphates are too high ($>$ 3.94 V vs Na/Na^+) to be used in ASIBs.

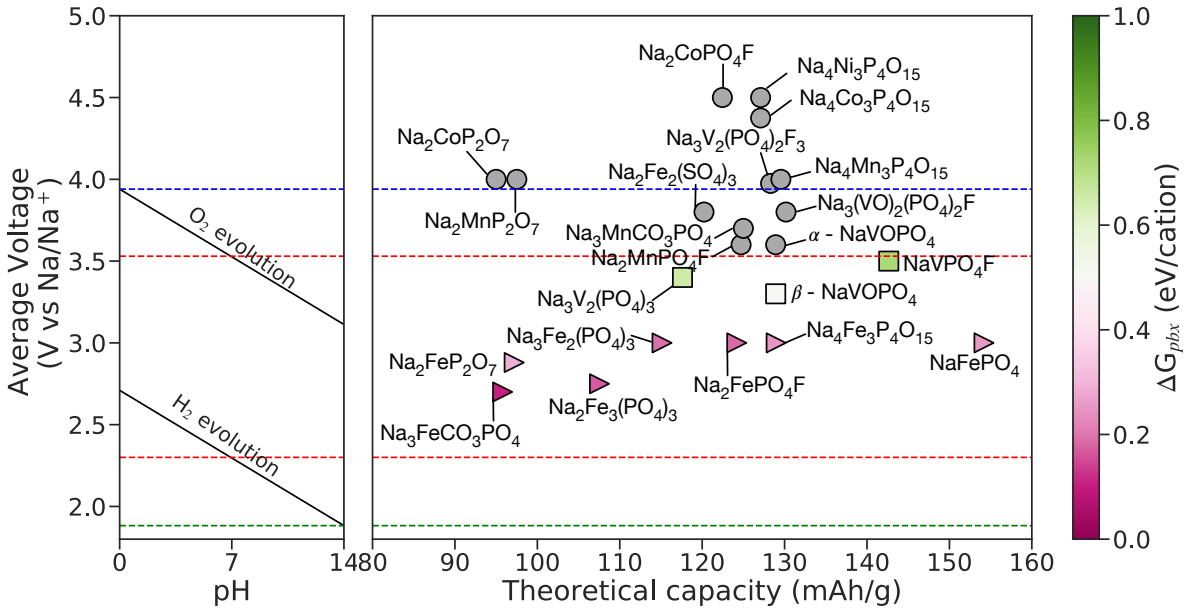

Figure 3.11: Left: O_2/H_2 evolution potential vs pH in water. Right: Experimentally measured average voltage vs theoretical capacity of known sodium-ion battery cathodes. The marker are colored by the calculated ΔG_{pbx} at C_{Na+} = 1 M and pH = 7. Triangle markers indicate the solid phases in decomposition products with H_2O, while square markers indicate non-solid phases in decomposition products. ΔG_{pbx} of cathodes with an average voltage larger than 3.53 V vs Na/Na^+ were not computed due to the evolution of O_2 and are represented in grey round markers. Red dashed lines indicate the electrochemical window of neutral aqueous electrolytes. Blue and green dashed line indicate the upper limit of O_2 evolution potential in acidic aqueous electrolyte (pH = 0) and lower limit of H_2 evolution potential in basic aqueous electrolyte (pH = 14), respectively.

Among the cathodes with average voltage within the electrochemical window of *neutral* aqueous electrolytes, the V-based cathodes generally exhibit high reactivity with water (high $\Delta G_{pbx} \geq 0.5$ eV/cation) and lack of solid decomposition products in aqueous solution, which suggests that they are intrinsically unstable in aqueous environments. This observation is in line with experimental observations. [185] The Fe-based cathodes generally exhibit far better aqueous stability, though with somewhat lower average voltages. $Na_2FeP_2O_7$, olivine-$NaFePO_4$, $Na_4Fe_3(PO_4)_2P_2O_7$ have already been studied as cathodes in ASIBs. NASICON-$Na_3Fe_2(PO_4)_3$ has been investigated as an anode in ASIBs with Fe^{2+}/Fe^{3+} redox potential at 2.5 V vs Na/Na^+ [134]. Our results showed that it can be used as cathodes in ASIBs with the activated Fe^{3+}/Fe^{4+} redox pair at a potential of $\sim$ 3.0 V vs Na/Na^+ [137]. Na_2FePO_4F, which shows an average voltage at around 3.0 V vs Na/Na^+ with theoretical capacity of 124.2 mAh/g [69], is a promising candidate for cathodes in ASIBs due to its high average working potential as well as high aqueous stability (ΔG_{pbx} = 0.2 eV/cation at 3.0 V vs Na/Na^+). The average voltages of alluadite-$Na_2Fe_3(PO_4)_3$ and sidorenkite-$Na_3Fe(CO_3)(PO_4)$ are somewhat too low in neutral electrolytes, resulting in a significant compromise in energy density in ASIBs. Nevertheless, they are potentially interesting cathodes in *basic* electrolytes when paired with appropriate lower-voltage anodes. Fe-based cathodes tend to form solid phases within 2.5 $\sim$ 3.53 V vs Na/Na^+ in aqueous solution and most compounds with Fe^{2+}/Fe^{3+} redox pairs are electrochemically active within this voltage range. Thus, looking for novel structures containing Fe^{2+}/Fe^{3+} redox pairs may achieve new cathodes in ASIBs.

In *acidic* aqueous electrolytes, several other cathodes - $Na_3MnCO_3PO_4$, Na_2MnPO_4F, $NaVOPO_4$ and $Na_3(VO)_2(PO_4)_2F$ - are predicted to have average voltage below the increased O_2 evolution potential. $Na_2Fe_2(SO_4)_3$ and the two V-containing cathodes - $NaVOPO_4$ and $Na_3(VO)_2(PO_4)_2F$ - exhibit high reactivity with water (similar to the other V containing cathodes) (See Figure 3.16(b)). Further, the the observed charge potential of Na_2MnPO_4F cathode in non-aqueous electrolyte is very high ($\sim$ 3.8 V vs $NaNa^+$), and the Pourbaix diagram analysis

predicts that Na_2MnPO_4F is highly unstable in acidic solutions, making it less promising for ASIB applications (see Figure S3). Hence, only $Na_3MnCO_3PO_4$, which has multiple voltage plateaus, has been selected for detailed analysis.

3.5 Detailed studies of promising candidates

Table 3.2: Calculated electrochemical properties of promising candidates for cathodes in ASIBs. The voltage range refers to the range where the materials is stable in solution. ΔG_{pbx}^{max} and Capacity refer to the maximum ΔG_{pbx} and accessible capacity in this voltage range, respectively. Barrier is the highest Na^+ migration barrier in the facile pathways

Formula	Space group	E_{hull} (meV/atom)	Voltage range (V vs Na/Na^+)	ΔG_{pbx}^{max} (eV/cation)	pH	Capacity (mAh/g)	Barrier (meV)
$Na_3Fe_2(PO_4)_3$	Cc	2	$2.5 \sim 3.53$	0.5	7	90	383
Na_2FePO_4F	$Pbcn$	0	$2.5 \sim 3.53$	0.2	7	124	277
$Na_2Fe_3(PO_4)_3$	$C2/c$	21	$2.12 \sim 3.35$	0.5	10	110	419
$Na_3FeCO_3PO_4$	$P2_1/m$	0	$2.39 \sim 3.23$	0.3	14	95.8	531
$Na_3MnCO_3PO_4$	$P2_1/m$	0	$2.39 \sim 3.23$	0.3	12	96	446

Table 3.2 summarizes the computed electrochemical properties of the five promising ASIB cathode candidates. A detailed discussion of each material is presented here.

NASICON-$Na_3Fe_2(PO_4)_3$ and Na_2FePO_4F. The calculated redox potential of Fe^{3+}/Fe^{4+} couple in NASICON-$Na_3Fe_2(PO_4)_3$ is $4.2 \sim 4.3$ V vs Na/Na^+. The experimental values were reported to be $3.0 \sim 3.6$ V vs Na/Na^+ with a solid solution behavior [137], making part of the Fe^{3+}/Fe^{4+} capacity accessible in aqueous electrolyte (Figure 3.18(a)). The low ΔG_{pbx} and solid Fe_2O_3 formed at potential $E > 2.5$ V vs Na/Na^+ means that a stable capacity of ~ 90 mAh/g should be achievable in neutral aqueous electrolytes (Figure 3.18(c)). A facile 1D diffusion mechanism with a barrier of 383 meV is observed from the CI-NEB calculations (Figure 3.19), suggesting high rate capability for $Na_3Fe_2(PO_4)_3$ cathode in ASIBs.

Sharma et al. [144] have previously reported Na_2FePO_4F as a cathode in a 17 M $NaClO_4$ "water-in-salt" electrolyte with a reversible capacity of 85 mAh/g and no significant capacity loss after 100 cycles. While the highly concentrated aqueous electrolyte shows relatively high

viscosity (5 mm^2s^{-1}), high cost and complex electrolyte/electrode interface phenomena [23], our results suggest that Na_2FePO_4F may also exhibit excellent electrochemical performance in standard low-cost, high diffusivity aqueous electrolytes (Figures 3.20-3.21).

$Na_3FeCO_3PO_4$ and Alluadite-$Na_2Fe_3(PO_4)_3$. The calculated voltage profile of the $Na_3FeCO_3PO_4$ (Figure 3.22(a)) shows one plateau at 2.66 V vs Na/Na^+, which is in line with previous experimental results [58] in non-aqueous electrolytes. $Na_3FeCO_3PO_4$ is predicted to be stable in basic solution with small ΔG_{pbx} (< 0.3 eV/cation). Similarly, alluadite-$Na_2Fe_3(PO_4)_3$ exhibits three computed voltage plateaus at 3.24, 3.23 and 2.23 V vs Na/Na^+(Figure 3.24(a)), while a solid-solution behavior was observed with an average working potential of 2.75 V vs Na/Na^+ [59]. Here, we propose alluadite-$Na_2Fe_3(PO_4)_3$ can be cycled within the potential range of $2.12 \sim 3.35$ V vs Na/Na^+ in basic electrolyte with pH of 10.(Figure 3.24(c)) Both cathode candidates exhibit reasonable diffusion barriers of 400-500 meV.(Figure 3.23 and 3.25) An anode with low working potential should be coupled with these cathodes in basic solution to achieve a high energy density in ASIBs.

$Na_3MnCO_3PO_4$. $Na_3MnCO_3PO_4$ was reported to exhibit a large charge/discharge potential gap in non-aqueous electrolyte [28]. Our calculations (Figure 3.27(a)) indicate that $Na_3MnCO_3PO_4$ have three voltage plateaus at 4.08, 3.80 and 3.04 V vs Na/Na^+. While the $Na_3MnCO_3PO_4$ compound is predicted to be unstable in acidic aqueous solution within high potential regime (Figure 3.27(c)), the aqueous stability analysis ((Figure 3.27(d))) predicts that it is stable within the potential range of $2.39 \sim 3.23$ V vs Na/Na^+ in a basic electrolyte (pH = 12) with facile Na^+ conductivity. (Figure 3.28)

All five cathodes are predicted to exhibit high aqueous stability across wide voltage ranges, and thus may have large accessible capacities in aqueous electrolytes. In particular, Na_2FePO_4F and $Na_2Fe_3(PO_4)_3$ cathodes are predicted to have theoretical capacities of 124 mAh g^{-1} and 110 mAh g^{-1} in aqueous solution, respectively, which outperform most of the known ASIBs cathodes in the literature (see Table 3.1). Also, the excellent electrochemical properties of the two

promising sidorenkites, $Na_3FeCO_3PO_4$ and $Na_3MnCO_3PO_4$, show that the easily synthesizable, low cost carbonophosphates family are a potential new class of for ASIB cathodes.

3.6 Conclusion

To conclude, we have performed a comprehensive investigation of the working potential and aqueous stability of well-established ASIB cathodes using DFT calculations. A set of rigorous design rules and a screening workflow to identify potentially promising ASIB cathodes were developed. By applying this screening workflow to a large database of known Na-ion battery cathode materials, five promising cathode materials - $Na_3Fe_2(PO_4)_3$, Na_2FePO_4F, $Na_3MnCO_3PO_4$, $Na_3FeCO_3PO_4$ and alluadite-$Na_2Fe_3(PO_4)_3$ were identified that exhibit high voltage, good capacity, high stability in aqueous environments and facile Na-ion migration. These findings pave the way the practical cathode development for large-scale energy-storage systems based on aqueous Na-ion chemistry.

Chapter 3 is, in full, a reprint of the material "Design principles for aqueous Na-ion battery cathodes." Chemistry of Materials 32, no. 16 (2020): 6875-6885. Xingyu Guo, Zhenbin Wang, Zhi Deng, Bo Wang, Xi Chen, and Shyue Ping Ong. The dissertation author was the primary investigator and author of this paper.

Appendix: Supplementary Design Principles for Aqueous Na-ion Battery Cathodes

3.7 Calculated binary phase diagrams of all compounds

3.7.1 Notes on the calculated convex hulls and voltage profiles

$Na_{0.44}MnO_2$. In experiment, there are at least six intermediate phases identified for $Na_{0.44}MnO_2$ during charge/discharge processes.[24] In our calculations, we predicted eight intermediate stable phases within the composition range of $Na_{0.22}MnO_2 \sim Na_{0.66}MnO_2$. Similarly, Kim et al. [71] reported six calculated intermediate stable phases within the same composition range. Our calculated voltage profile is consistent with the experimental results. (Figure 3(a))

$Na_3V_2(PO_4)_3$. NASICON-type $Na_3V_2(PO_4)_3$ was reported to exhibit reversible phase transition from $NaV_2(PO_4)_3$ to $Na_3V_2(PO_4)_3$ during charge/discharge processes with a single voltage plateau at 3.39 V vs Na/Na^+[141]. According to our calculated convex hull, no stable intermediate phase is found between $NaV_2(PO_4)_3$ and $Na_3V_2(PO_4)_3$, which is also in line with the computational results by Lim et al. [93].

$Na_2FeP_2O_7$. *Ex situ* XRD characterization indicates that $Na_2FeP_2O_7$ undergoes successive

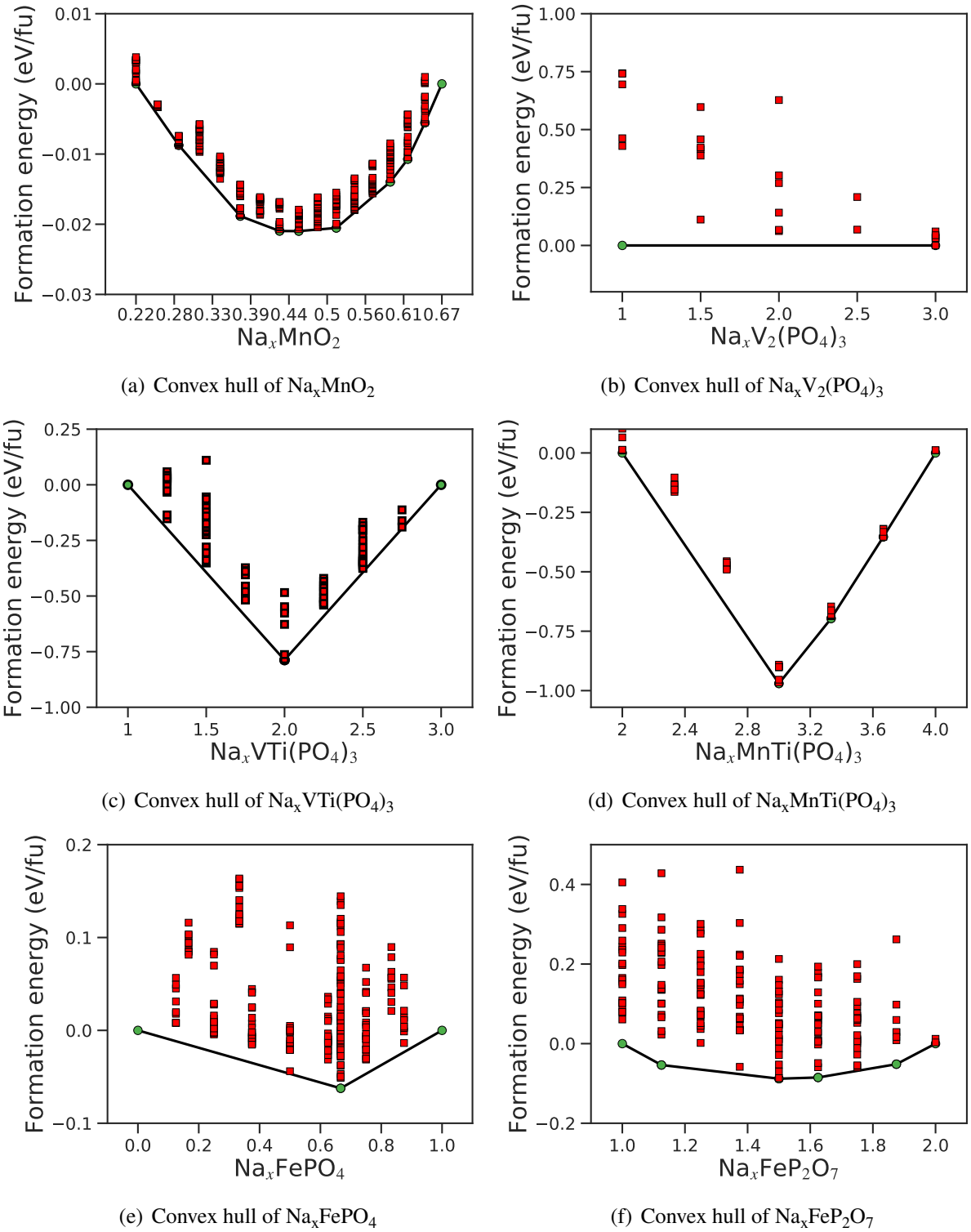

(a) Convex hull of Na_xMnO_2

(b) Convex hull of $Na_xV_2(PO_4)_3$

(c) Convex hull of $Na_xVTi(PO_4)_3$

(d) Convex hull of $Na_xMnTi(PO_4)_3$

(e) Convex hull of Na_xFePO_4

(f) Convex hull of $Na_xFeP_2O_7$

Figure 3.12: Calculated convex hull of cathodes in aqueous sodium ion batteries.

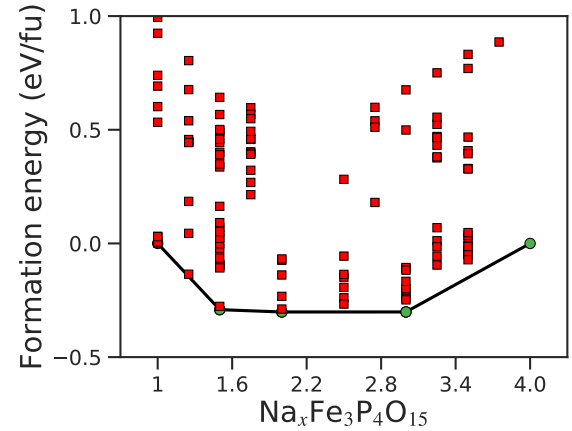

(a) Convex hull of $Na_xFe_3P_4O_{15}$

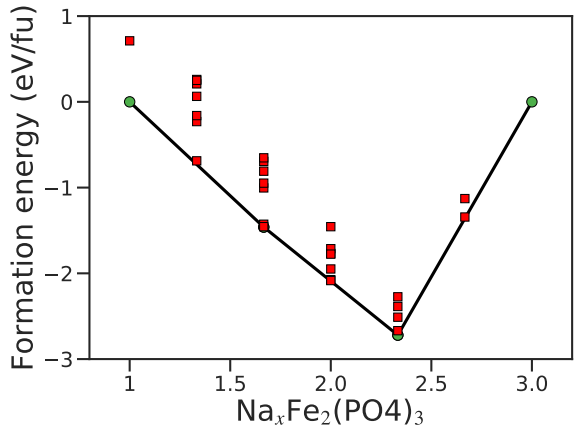

(b) Convex hull of $Na_xFe_2(PO_4)_3$

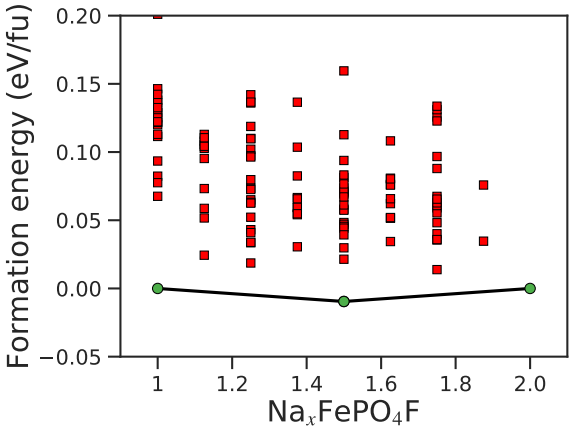

(c) Convex hull of Na_xFePO_4F

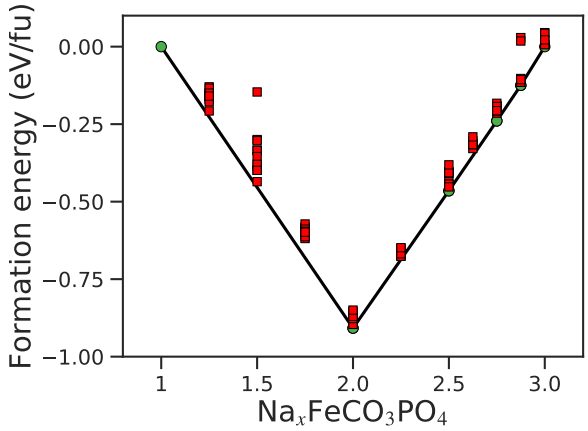

(d) Convex hull of $Na_xFeCO_3PO_4$

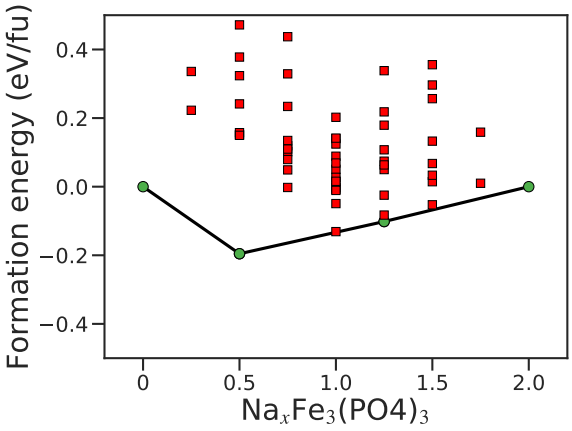

(e) Convex hull of $Na_xFe_3(PO_4)_3$

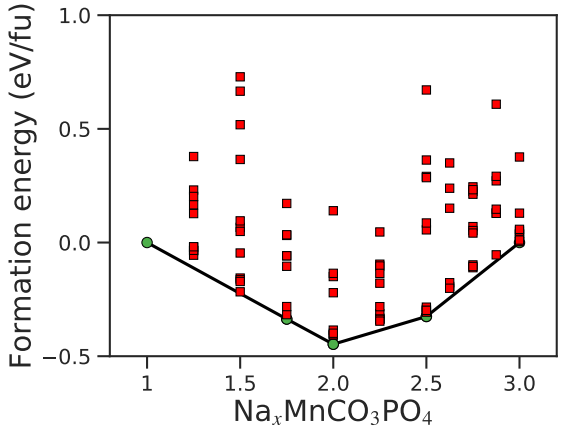

(f) Convex hull of $Na_xMnCO_3PO_4$

Figure 3.12: (Continued) Calculated convex hull of cathodes in aqueous sodium ion batteries.

biphasic transitions via various intermediate phases.[72] Four voltage plateaus located at 2.52, 2.99, 3.08 and 3.24 V vs Na/Na^+ have been observed in experiments. Our calculations showed that four intermediate stable phases with respect to $Na_2FeP_2O_7$ and $NaFeP_2O_7$ and the calculated voltage profile shows five plateaus at 2.405, 2.694, 2.793, 2.910 and 3.247V vs Na/Na^+, which are close to the experimental results. The only difference is that the experimental capacity drops rapidly when the voltage is lower than 2.99 V vs Na/Na^+. Previous calculations by Kim et al. [72] also suggested four intermediate stable phases but with slightly different compositions.

$NaFePO_4$. In our calculation, there is a stable phase at $Na_{2/3}FePO_4$, which is in line with the previous experimental[20] and calculation results.[140] The calculated voltage profiles show two plateaus at 3.0 V and 2.73 V vs Na/Na^+, which is close to the voltages reported experimentally[112].

Na_2FePO_4F. Li et al. [91] have shown that Na_2FePO_4F exhibits two two-phase reactions and form $Na_{1.5}FePO_4F$ intermediate phase at low C rate (0.1 C $\sim$ 1 C). In our calculations, we predicted there is only one stable phase at $Na_{1.5}FePO_4F$, which is in line with experimental[91] and the computational results[146]. The calculated voltage profile shows two plateau at 2.87 and 2.91 V vs Na/Na^+, which is close to the experimental results of 2.91 and 3.06 V vs Na/Na^+.[91]

3.8 Calculated voltage profile of Na_xMnO_2 in basic electrolyte

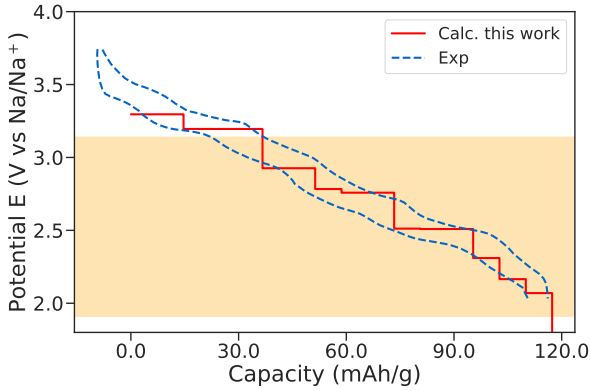

Figure 3.13: Calculated voltage profile of Na_xMnO_2 ($x = 0.22 - 0.66$). The electrochemical stability windows at pH = 13.5 are shaded orange. The experimental voltage profile is from ref 71.

3.9 Calculated voltage profiles, Pourbaix diagram and ΔG_{pbx} of NASICON $Na_3MnTi(PO_4)_3$ cathode

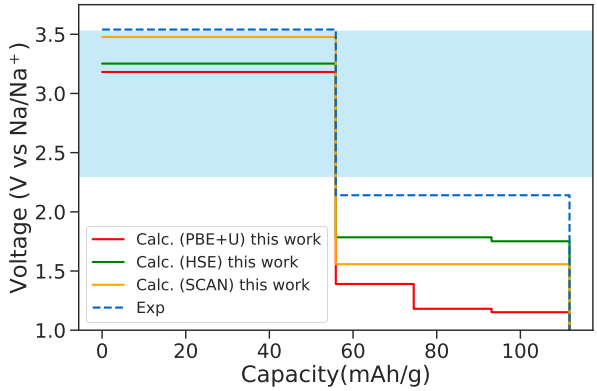

(a)

Figure 3.14: (a) Voltage profile of $Na_xMnTiP_3O_{12}$. Electrochemical window (pH = 7) is shaded with blue color.

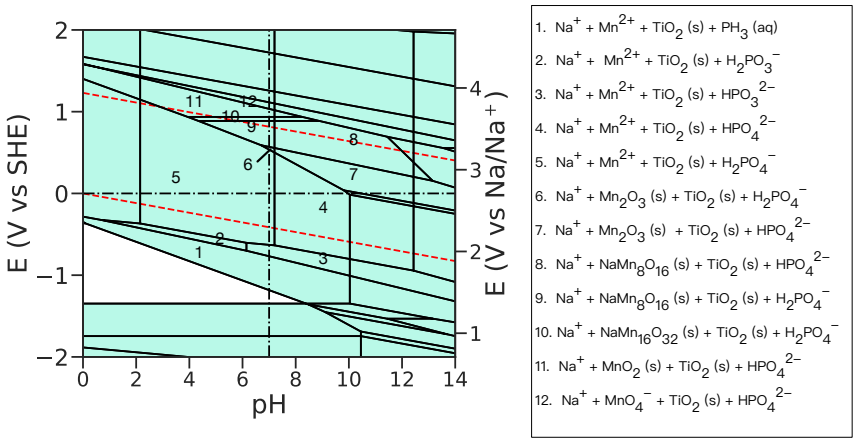

(a)

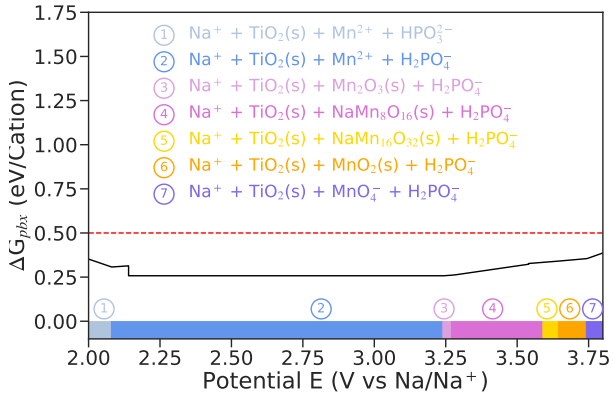

(b)

Figure 3.14: (Continued) (b) Calculated Pourbaix diagram of $Na_3MnTiP_3O_{12}$. Regions containing solid phases are shaded with green color. (c) ΔG_{pbx} of $Na_xMnTiP_3O_{12}$ as a function of potential in neutral aqueous solution (pH = 7).

3.10 Pourbaix diagram of $Na_2FeP_2O_7$ and $Na_4Fe_3P_4O_{15}$ cathode

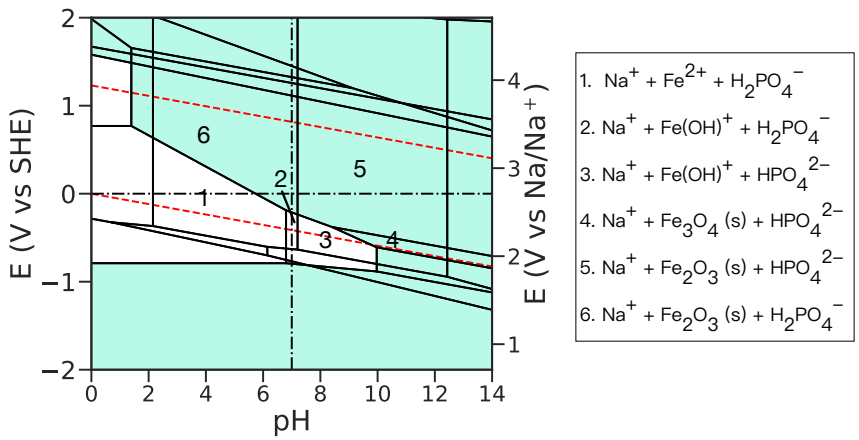

(c) Calculated Pourbaix diagram of $Na_2FeP_2O_7$

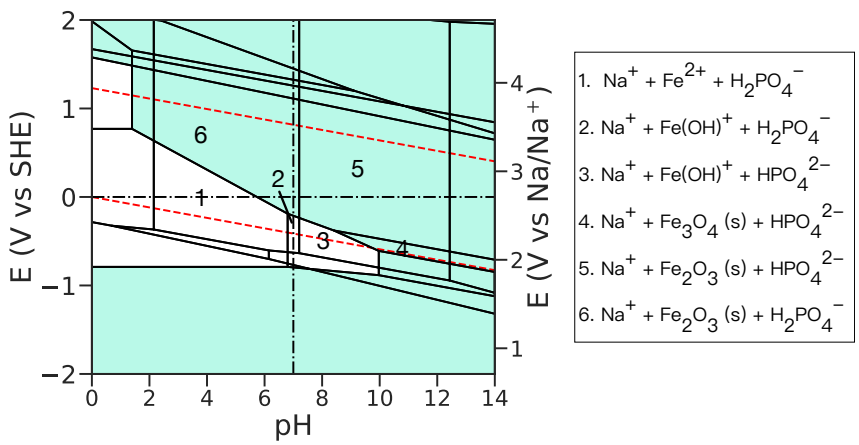

(d) Calculated Pourbaix diagram of $Na_4Fe_3P_4O_{15}$

Figure 3.15: Calculated Pourbaix diagram of (a) $Na_2FeP_2O_7$ and (b) $Na_4Fe_3P_4O_{15}$. Regions containing solid phases are shaded green.

3.11 Calculated ΔG_{pbx} as a function of pH of selected cathodes at their average voltage

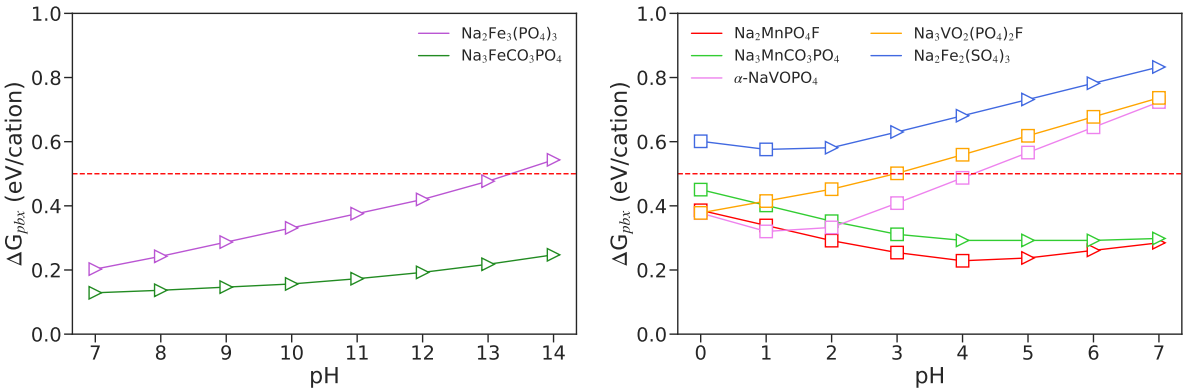

(a) (b)

Figure 3.16: Calculated ΔG_{pbx} vs pH of selected cathodes in (a) basic electrolytes (pH = 7 $\sim$ 14) (b) acidic electrolytes (pH = 0 $\sim$ 7). Triangle markers indicate the solid phases in decomposition products with H_2O, while square markers indicate non-solid phases in decomposition products.

3.12 Aqueous stability analysis of Na_2MnPO_4F

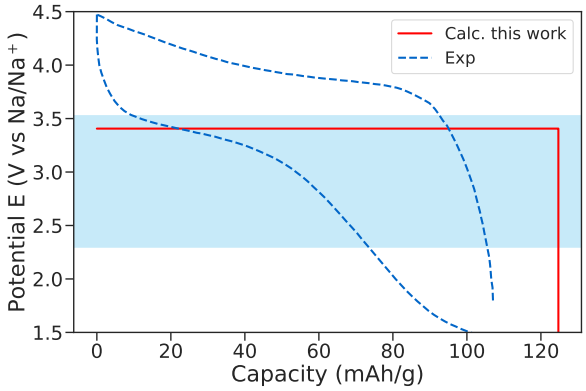

(a) Voltage profile of Na_xMnPO_4F

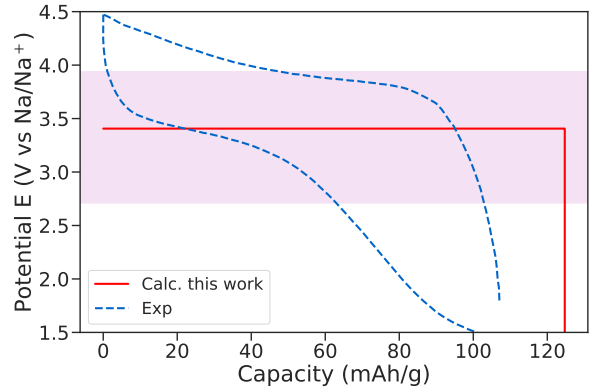

(b) Voltage profile of Na_xMnPO_4F

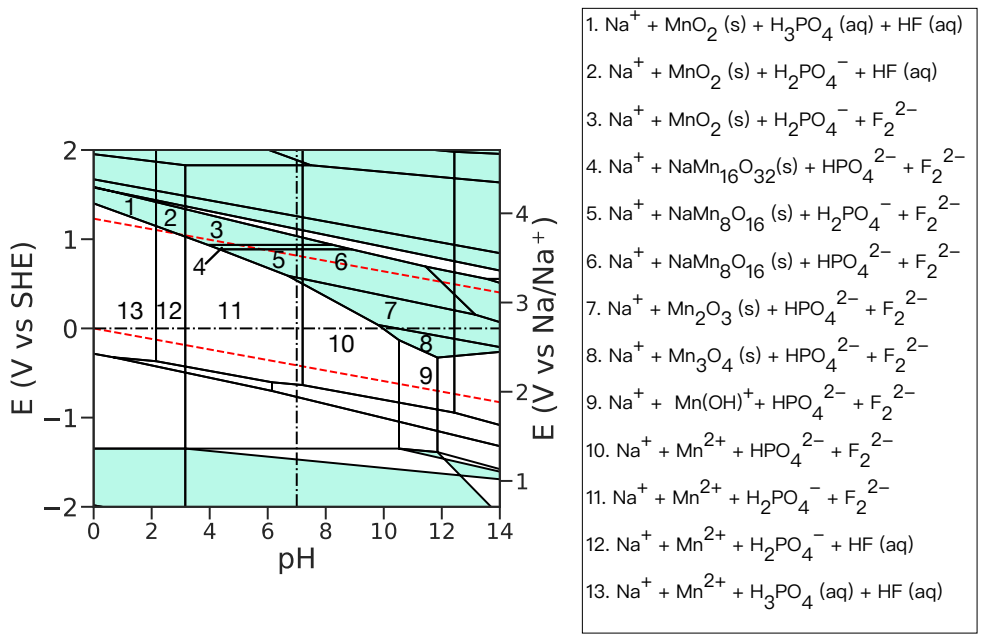

(c) Calculated Pourbaix diagram of Na_2MnPO_4F

Figure 3.17: Voltage profile of Na_xMnPO_4F. Electrochemical window at (a) pH =7 and (b) pH = 0 is shaded with blue and pink color, respectively. The experimental voltage profile is from ref 65 (c) Calculated Pourbaix diagram of Na_2MnPO_4F. Regions containing solid phases are shaded with green color.

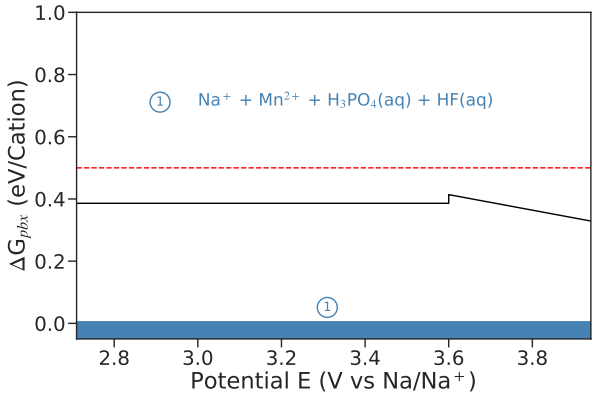

(a) ΔG_{pbx} vs E of Na_xMnPO_4F

Figure 3.17: (Continued) (d) ΔG_{pbx} of Na_xMnPO_4F as a function of potential in acidic aqueous solution (pH = 0).

3.13 Detailed calculations of the selected promising candidates as cathodes in ASIBs

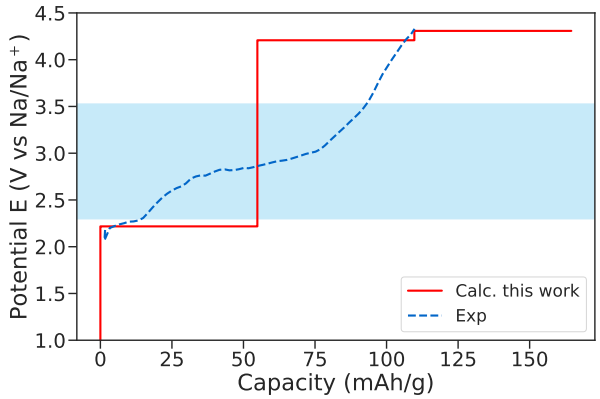

(b) Voltage profile of $Na_xFe_2(PO_4)_3$

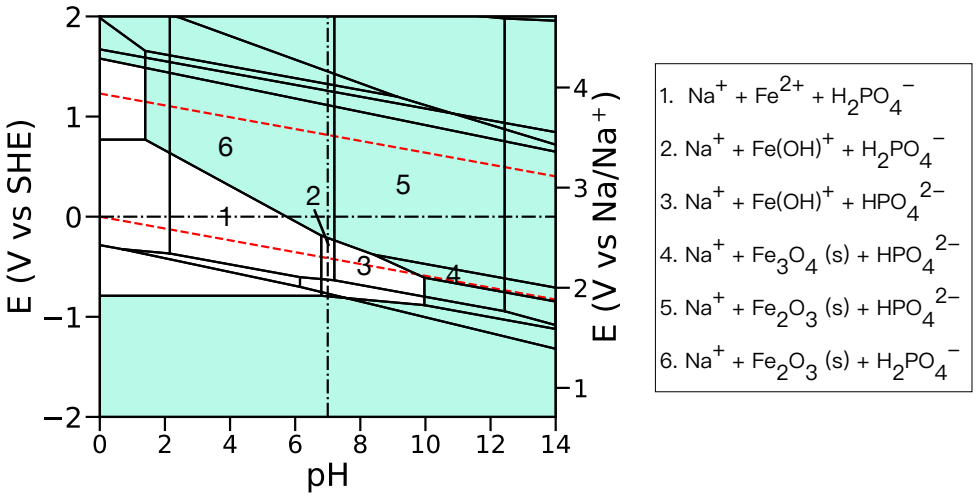

(c) Calculated Pourbaix diagram of $Na_3Fe_2(PO_4)_3$

Figure 3.18: (a) Voltage profile of $Na_xFe_2(PO_4)_3$. Electrochemical window (pH = 7) is shaded with blue color. The experimental voltage profile is from ref 137 (b) Calculated Pourbaix diagram of $Na_3Fe_2(PO_4)_3$. Regions containing solid phases are shaded with green color.

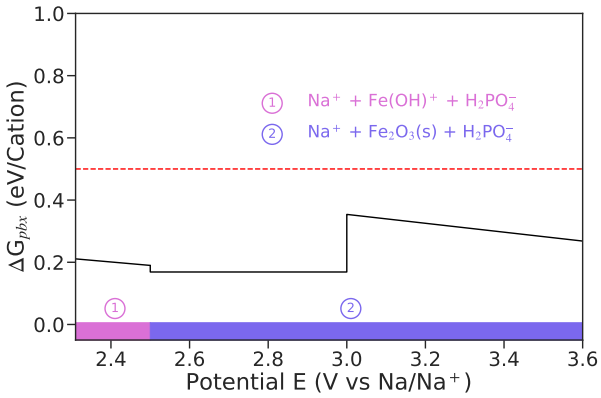

(a) ΔG_{pbx} vs E of $Na_xFe_2(PO_4)_3$

Figure 3.18: (Continued) (c) ΔG_{pbx} of $Na_xFe_2(PO_4)_3$ as a function of potential in neutral aqueous solution (pH = 7).

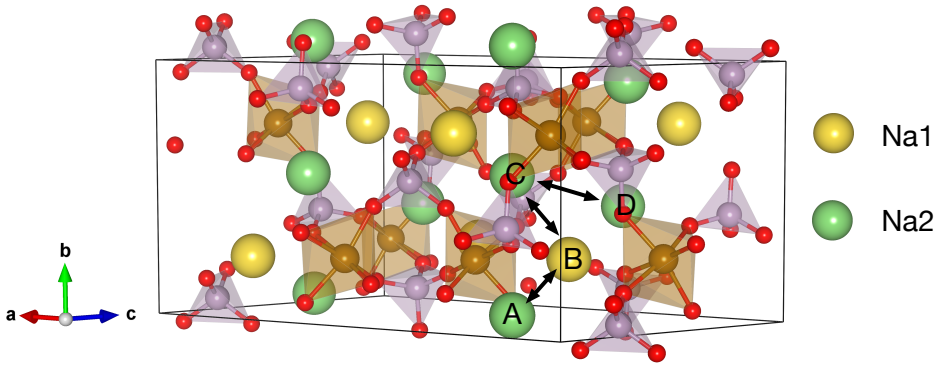

(b) Migration path

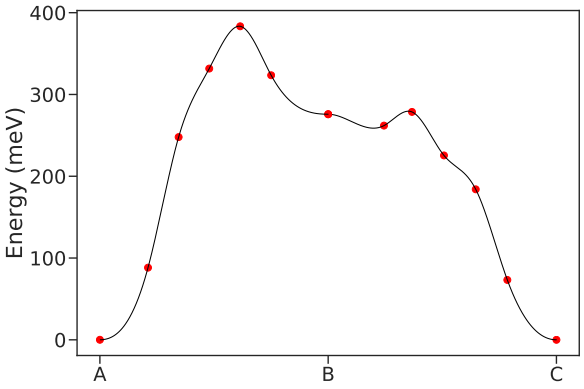

(c) A→B→ C

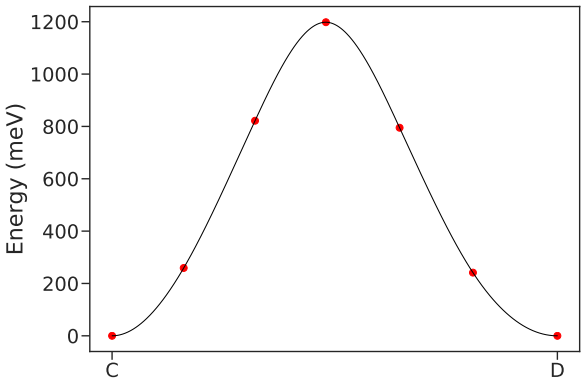

(d) C→D

Figure 3.19: (a) Investigated Na vacancy diffusion paths in $Na_3Fe_2(PO_4)_3$. Symmetrically distinct Na1 and Na2 are represented by green and yellow spheres, respectively. Purple tetrahedra and brown octahedra indicate PO_4 and FeO_6. (b)(c) Calculated CI-NEB migration barriers for selected percolating path.

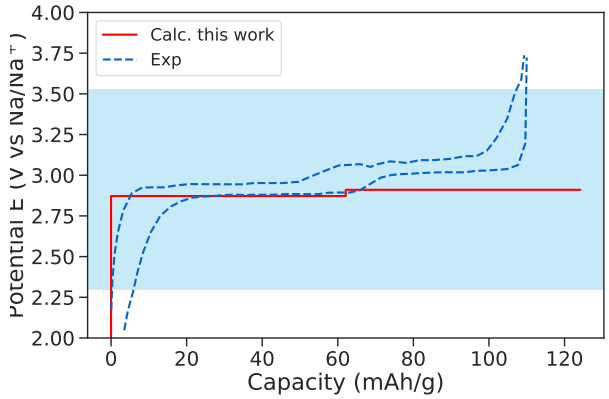

(a) Voltage profile of Na_xFePO_4F

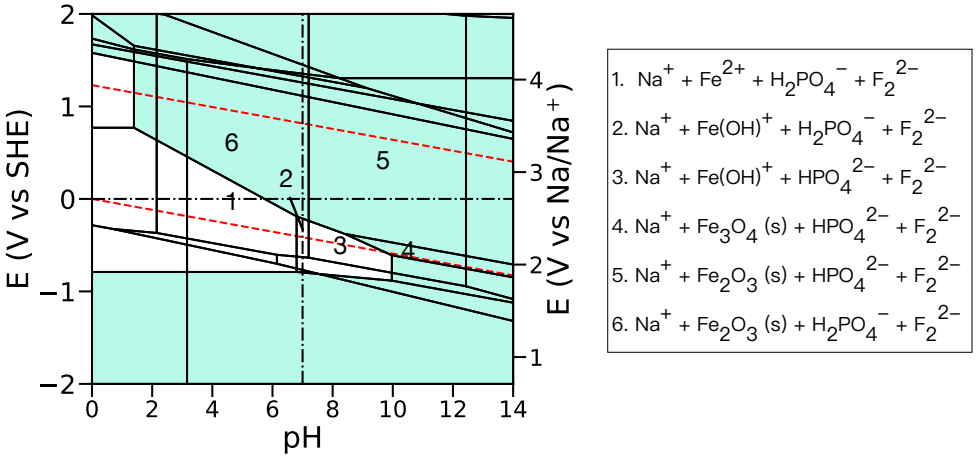

(b) Calculated Pourbaix diagram of Na_2FePO_4F

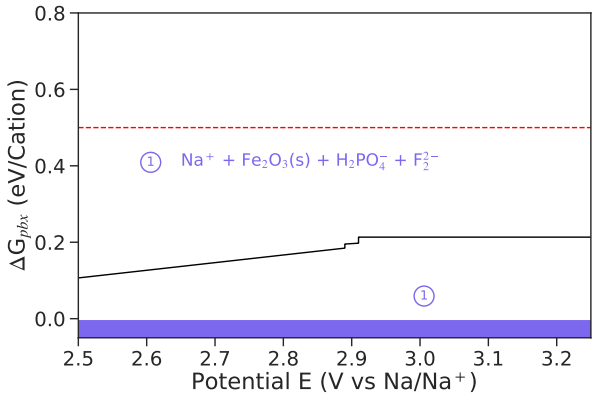

(c) ΔG_{pbx} vs E of Na_xFePO_4F

Figure 3.20: (a) Voltage profile of Na_2FePO_4F. Electrochemical window (pH = 7) is shaded with blue color. The experimental voltage profile is from ref 69. (b) Calculated Pourbaix diagram of Na_2FePO_4F. Regions containing solid phases are shaded with green color. (c) ΔG_{pbx} of Na_xFePO_4F as a function of potential in neutral aqueous solution (pH = 7).

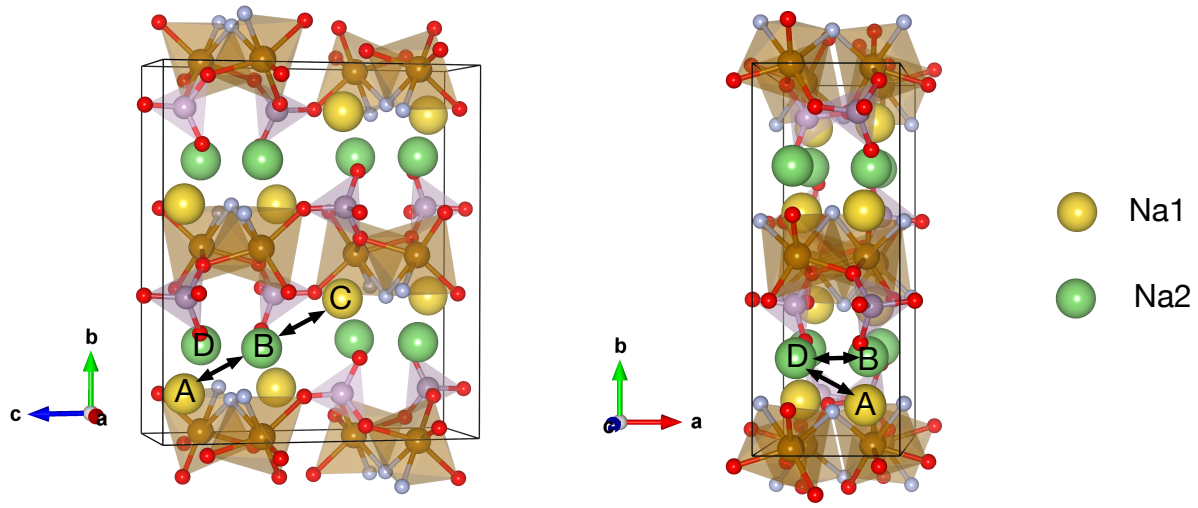

(a) Migration path

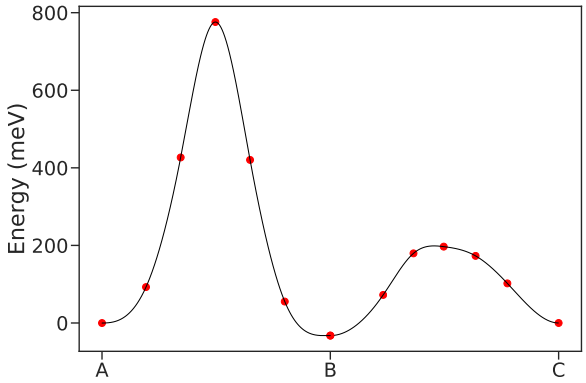

(b) A→B→C

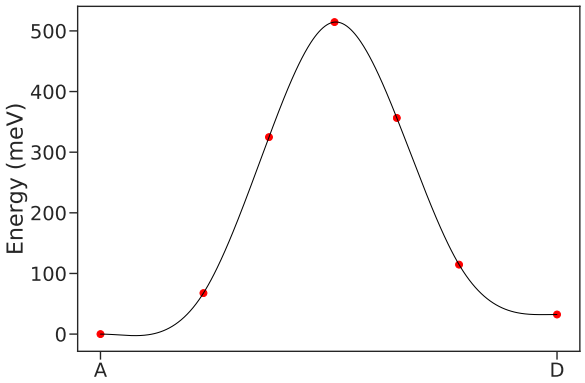

(c) A→D

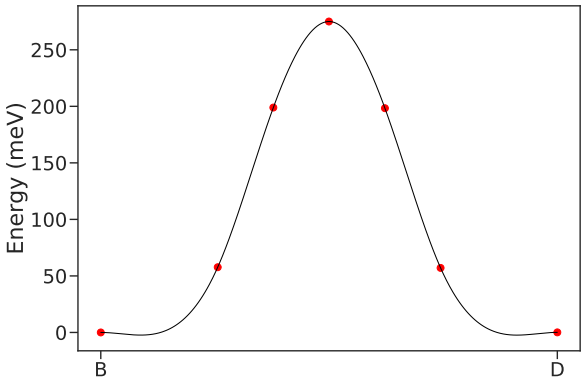

(d) B→D

Figure 3.21: (a) Investigated Na vacancy diffusion paths in Na_2FePO_4F. Symmetrically distinct Na1 and Na2 are represented by green and yellow spheres, respectively. Purple tetrahedra and brown octahedra indicate PO_4 and FeO_4F_2. (b)(c)(d) Calculated CI-NEB migration barriers for selected percolating path.

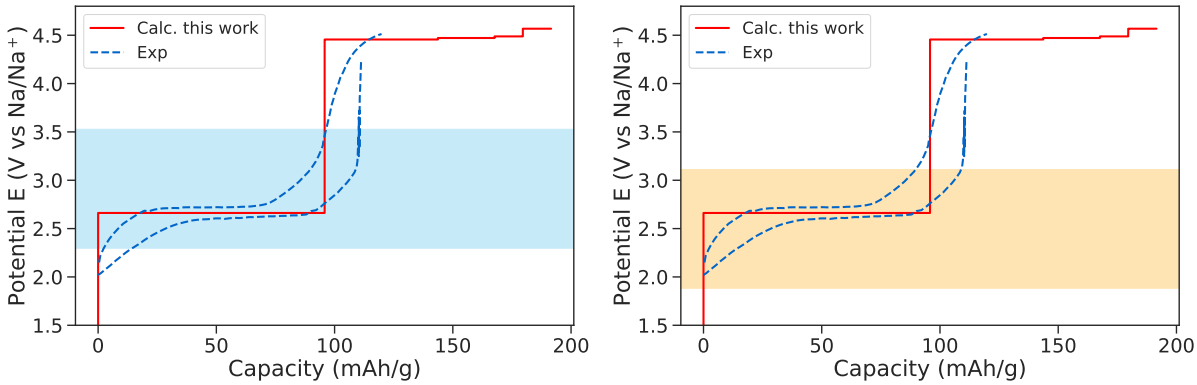

(a) Voltage profile of $Na_xFeCO_3PO_4$

(b) Voltage profile of $Na_xFeCO_3PO_4$

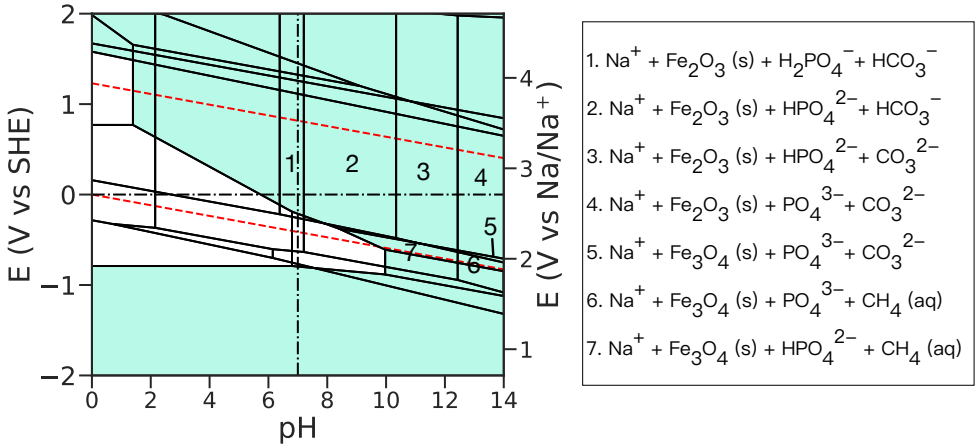

(c) Calculated Pourbaix diagram of $Na_3FeCO_3PO_4$

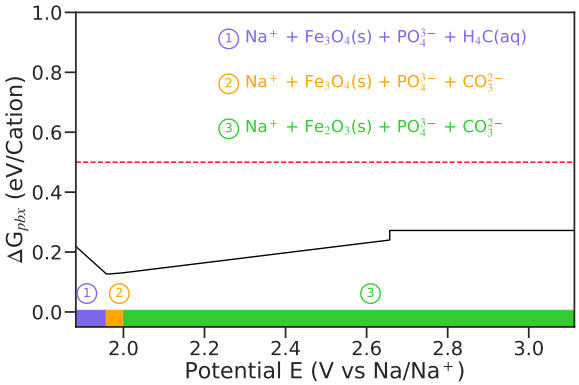

(d) ΔG_{pbx} vs E of $Na_xFeCO_3PO_4$

Figure 3.22: (a) Voltage profile of $Na_xFeCO_3PO_4$. Electrochemical window at pH =7 and pH = 14 is shaded with blue and orange color, respectively. The experimental voltage profile is from ref 58 (b) Calculated Pourbaix diagram of $Na_3FeCO_3PO_4$. Regions containing solid phases are shaded with green color. (c) ΔG_{pbx} of $Na_xFeCO_3PO_4$ as a function of potential in basic aqueous solution (pH = 12).

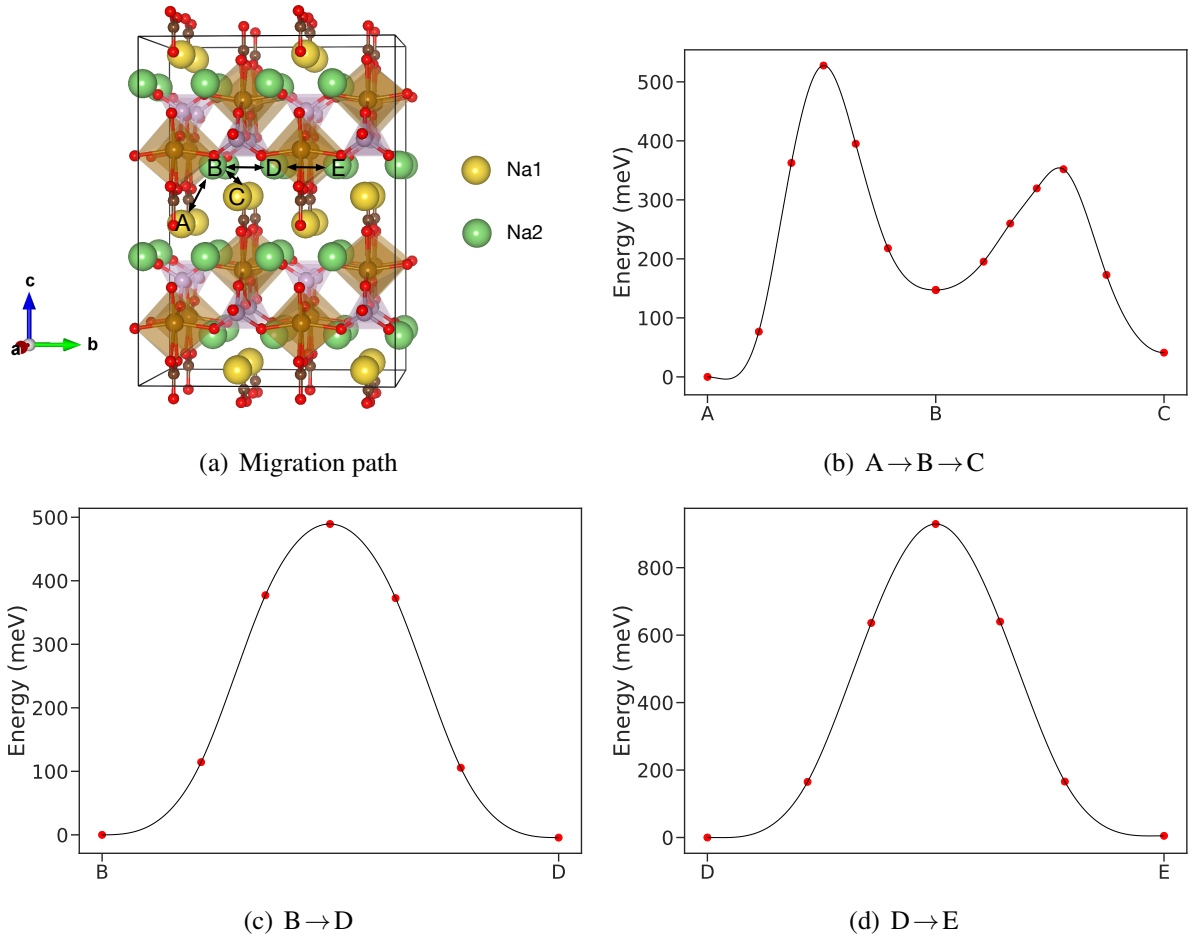

(a) Migration path

(b) A→B→C

(c) B→D

(d) D→E

Figure 3.23: (a) Investigated Na vacancy diffusion paths in $Na_3FeCO_3PO_4$. Symmetrically distinct Na1 and Na2 are represented by green and yellow spheres, respectively. Purple tetrahedra and brown octahedra indicate PO_4 and FeO_6. (b)(c)(d) Calculated CI-NEB migration barriers for selected percolating path.

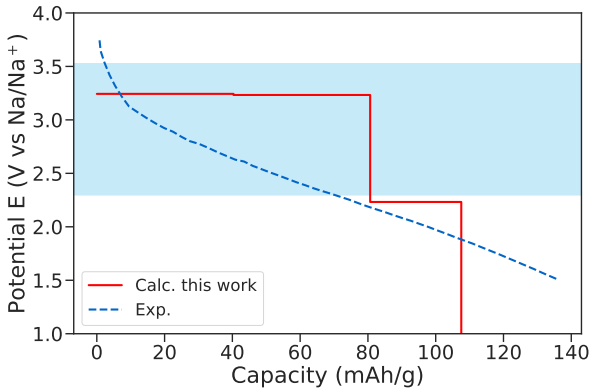

(a) Voltage profile of $Na_xFe_3(PO_4)_3$

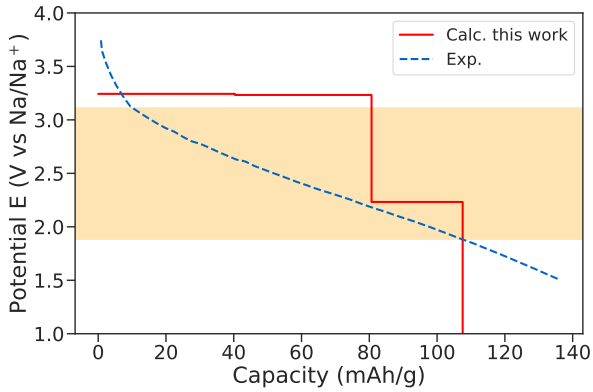

(b) Voltage profile of $Na_xFe_3(PO_4)_3$

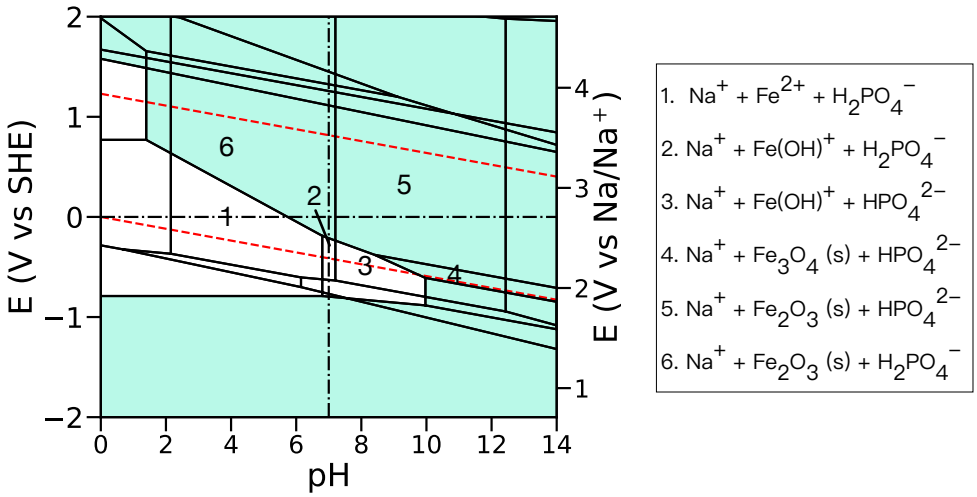

(c) Calculated Pourbaix diagram of $Na_2Fe_3(PO_4)_3$

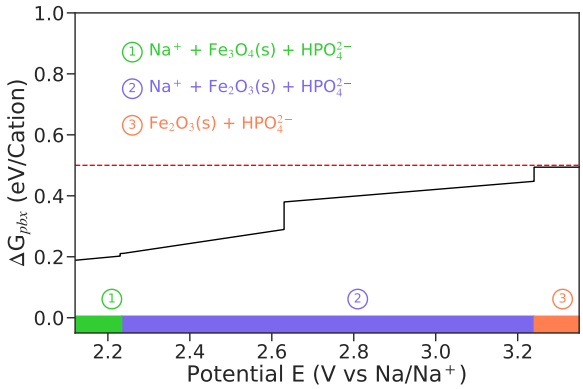

(d) ΔG_{pbx} vs E of $Na_xFe_3(PO_4)_3$

Figure 3.24: Voltage profile of $Na_xFe_3(PO_4)_3$. Electrochemical window at (a) pH =7 and (b) pH = 14 is shaded with blue and orange color, respectively. The experimental voltage profile is from ref 59. (b) Calculated Pourbaix diagram of $Na_2Fe_3(PO_4)_3$. Regions containing solid phases are shaded with green color. (c) ΔG_{pbx} of $Na_xFe_3(PO_4)_3$ as a function of potential in basic aqueous solution (pH = 14).

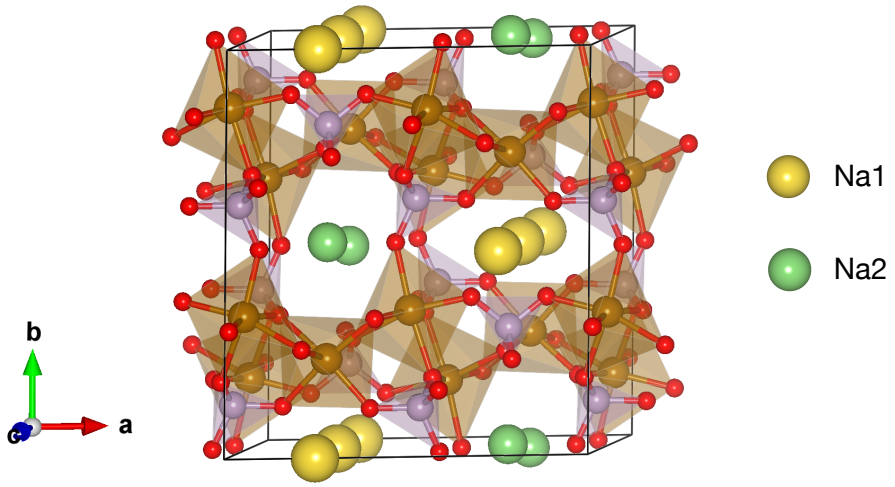

(a) Migration path

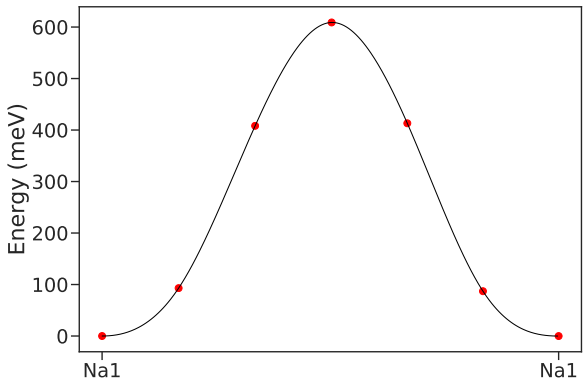

(b) Na1 → Na1

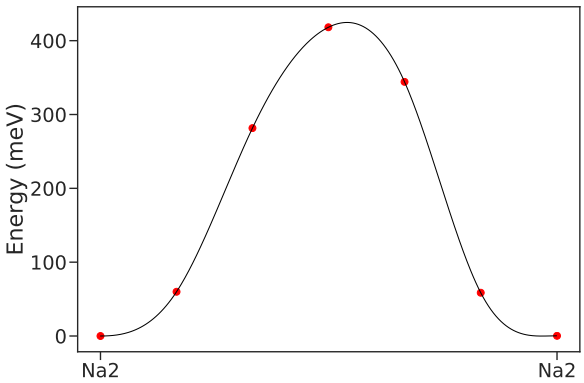

(c) Na2 → Na2

Figure 3.25: (a) Investigated Na vacancy diffusion paths in $Na_2Fe_3(PO_4)_3$. Symmetrically distinct Na1 and Na2 are represented by green and yellow spheres, respectively. Purple tetrahedra and brown octahedra indicate PO_4 and FeO_6. (b)(c) Calculated CI-NEB migration barriers for selected percolating path.

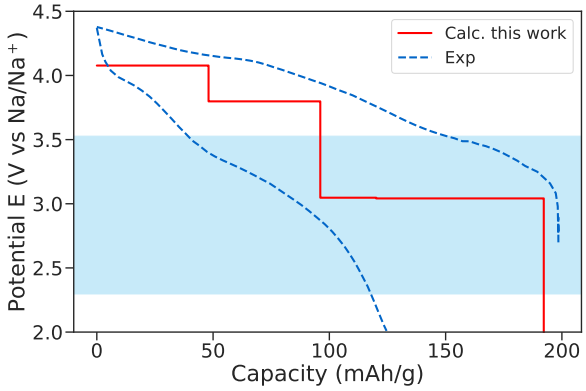

(a) Voltage profile of $Na_xMnCO_3PO_4$

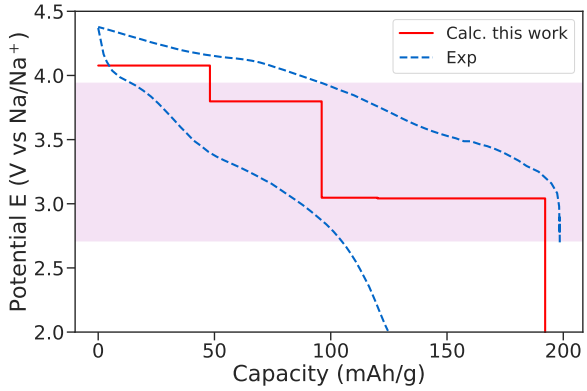

(b) Voltage profile of $Na_xMnCO_3PO_4$

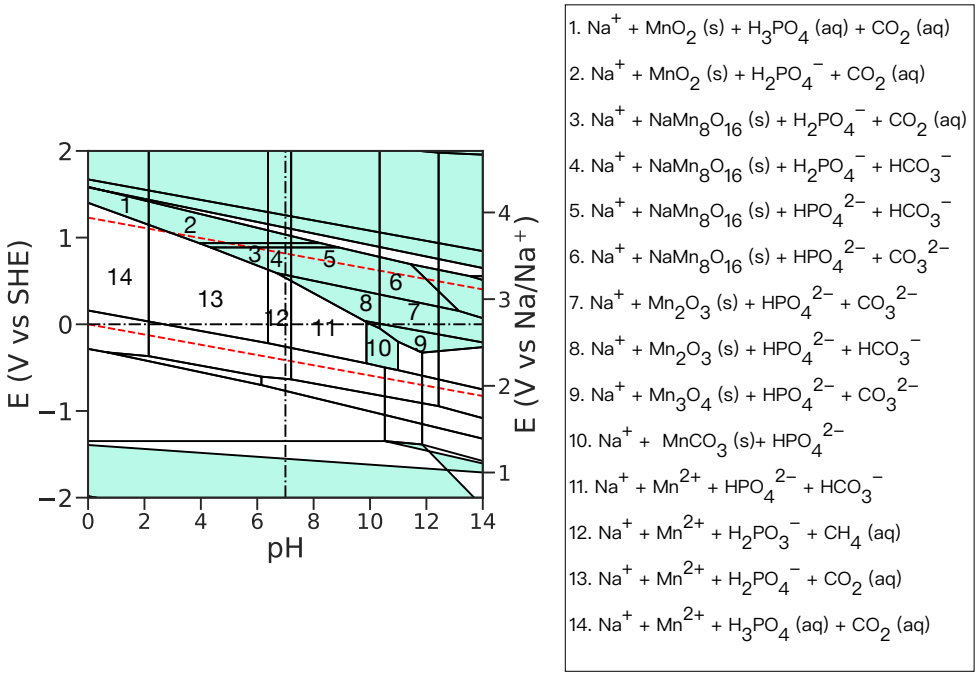

(c) Calculated Pourbaix diagram of $Na_3MnCO_3PO_4$

Figure 3.26: Voltage profile of $Na_xMnCO_3PO_4$. Electrochemical window at (a) pH =7 and (b) pH = 0 is shaded with blue and pink color, respectively. The experimental voltage profile is from ref 28. (c) Calculated Pourbaix diagram of $Na_3MnCO_3PO_4$. Regions containing solid phases are shaded with green color.

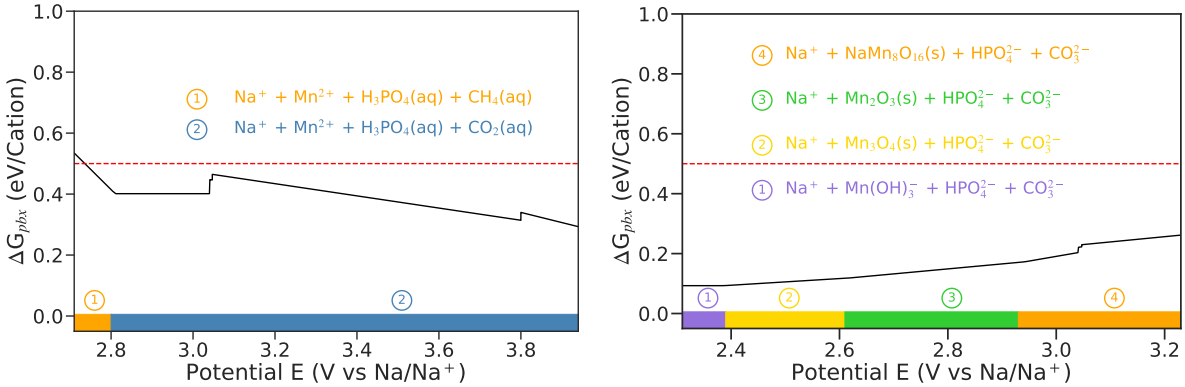

(a) ΔG_{pbx} vs E of $Na_xMnCO_3PO_4$ at pH = 1

(b) ΔG_{pbx} vs E of $Na_xMnCO_3PO_4$ at pH = 12

Figure 3.27: (Continued) ΔG_{pbx} of $Na_xMnCO_3PO_4$ as a function of potential (d) in acidic aqueous solution (pH = 1)and (e)in basic aqueous solution (pH = 12).

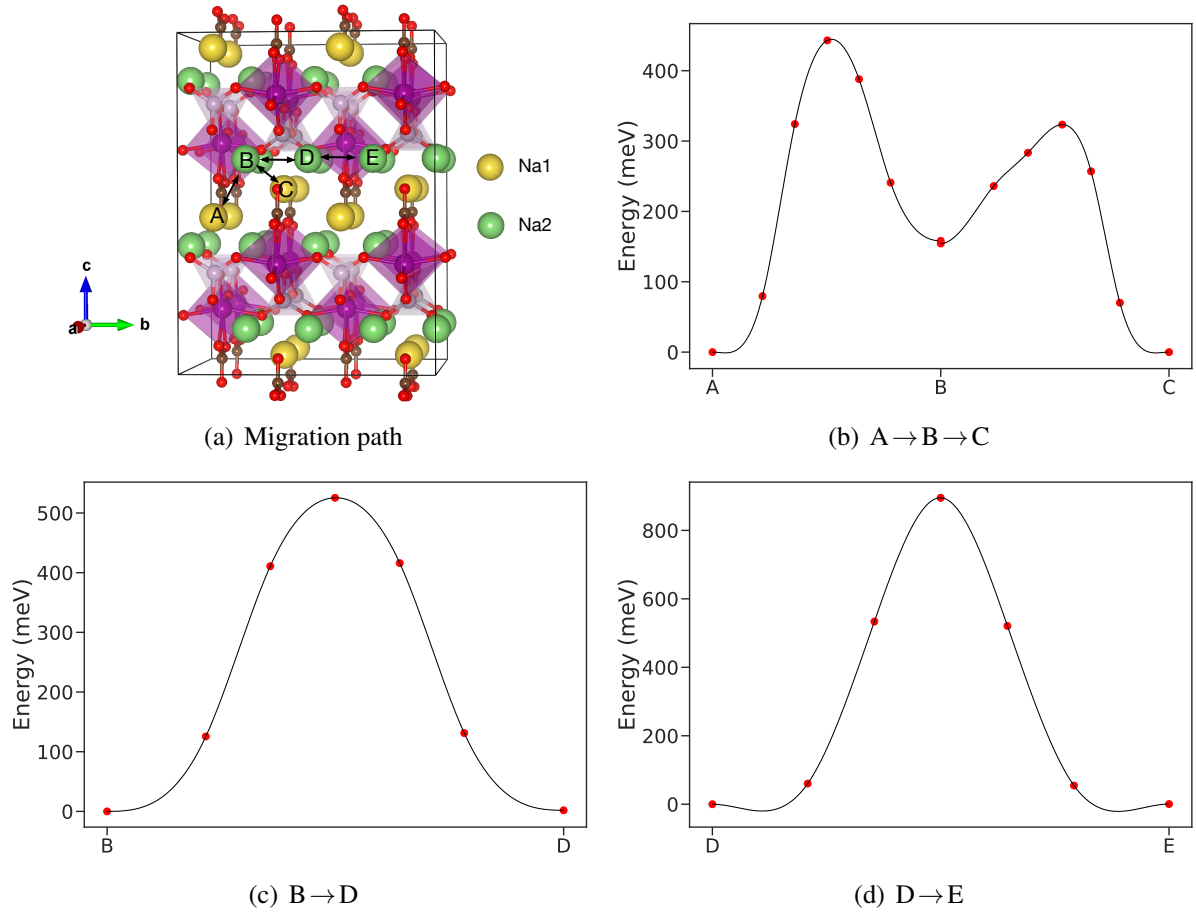

(a) Migration path

(b) A→B→C

(c) B→D

(d) D→E

Figure 3.28: (a) Investigated Na vacancy diffusion paths in $Na_3MnCO_3PO_4$. Symmetrically distinct Na1 and Na2 are represented by green and yellow spheres, respectively. Purple tetrahedra and violet octahedra indicate PO_4 and MnO_6. (b)(c)(d) Calculated CI-NEB migration barriers for selected percolating path.

Chapter 4

High-throughput modeling of sodium ion battery electrode materials with good performance

4.1 Introduction

The aim of this project is to design and optimize novel cathodes for aqueous rechargeable sodium-ion batteries (ASIBs) using a data-driven approach that integrates high-throughput first principles modeling with experimental synthesis and characterization. The target is to develop materials that demonstrate redox potentials in the suitable range of electrochemical stability in aqueous electrolytes, as well as good chemical stability in water, i.e., does not react with water and/or forms a stable passivation interface. The high-throughput framework developed in Chapter 3 is used to automate accurate first principles calculations of key properties of ASIB candidates, such as voltage, capacity, Na^+ conductivity, and aqueous stability. Furthermore, using this framework, a large database of known and novel aqueous Na-ion battery cathodes (Na-ion Aqueous Electrode Database, or NAED) was developed, and then screened to identify promising

candidates for synthesis and experimentation.

4.2 Construction of Na-ion aqueous electrode (NEAD) database

4.2.1 Generation of initial candidate cathodes

Our list of redox active elements and allowed oxidation state consists of Ti (+2 to +4), V (+2 to +5), Cr (+2 to +6), Mn (+2 to +4), Fe (+2 to +4), Co (+2 to +4), Ni (+2 to +4), Cu (+1 to +3), Nb (+3 to +5), Mo (+3 to +6), Sn (+2 to +4), Sb (+3 to +5) and Bi (+3 to +5). Our set of initial candidate cathodes was obtained from the 2017 version of Inorganic Crystal Structure database (ICSD) [15] and Materials Project database (v2019.02) [61]. All compounds containing sodium and at least one redox active metal were considered. Compounds containing lanthanides or actinides were excluded in this work due to their relatively high costs. In total, our database contains 2847 compounds at the current juncture.

4.2.2 Computation methods

DFT calculations

All density functional theory (DFT) calculations were performed using the Vienna *ab initio* simulation (VASP) package within the projected-augmented wave method. [81, 19] The exchange-correlation functional used for structural relaxation and energy calculations was the Perdew-Burke-Ernzerhof (PBE) generalized gradient approximation (GGA) functional [127] with a Hubbard U [34] applied for $3d$ transition metals. The U parameters used were similar to those from the Materials Project [62].

Phase stability

The phase stability of all compounds was estimated by calculating the energy above the linear combination of stable phases in the 0 K DFT phase diagram, also known as the energy above hull, Ehull.[114] For phase diagram construction, the energies of all compounds other than those of direct interest in this project are obtained from the MP via the Materials Application Programming Interface (API). [61]

Average voltage

The average intercalation potential of Na into a host X vs Na/Na^+ was calculated by the equation [9]:

$$V = -\frac{E_{DFT}(\mathrm{Na_nX}) - E_{DFT}(\mathrm{Na_{n-x}X}) - xE_{DFT}(\mathrm{Na})}{xe} \tag{4.2.1}$$

where $E_{DFT}(\cdot)$ denotes the DFT calculated total energy, and e is the electron charge. In this work, the average voltage was calculated based on a one-electron-per-transition-metal redox reaction for all materials.

Aqueous stability

The aqueous stability of a cathode was evaluated by computing its Gibbs free energy difference (ΔG_{pbx}) with respect to the stable domains on Pourbaix diagram as a function of pH and potential (E)[136, 147].

4.2.3 Diffusion barriers

The sodium vacancy migration barriers were calculated using the climbing image nudged elastic band (CI-NEB) method[51, 50]. Here, the PBE functional without Hubbard U was adopted to avoid the possible mixing of the diffusion barrier with a charge transfer barrier.[116] The force convergence criterion was 0.05 eV/Å.

4.2.4 Data records

A user-friendly web application has been developed to allow users to efficiently explore the Ehull, theoretical capacity, average voltage, ΔG_{pbx} at average voltage (pH = 7) and the volume change during charge/discharge processes of the compounds investigated. This web application is at https://aqna.herokuapp.com/ (a screen shot is given in Figure 4.1).

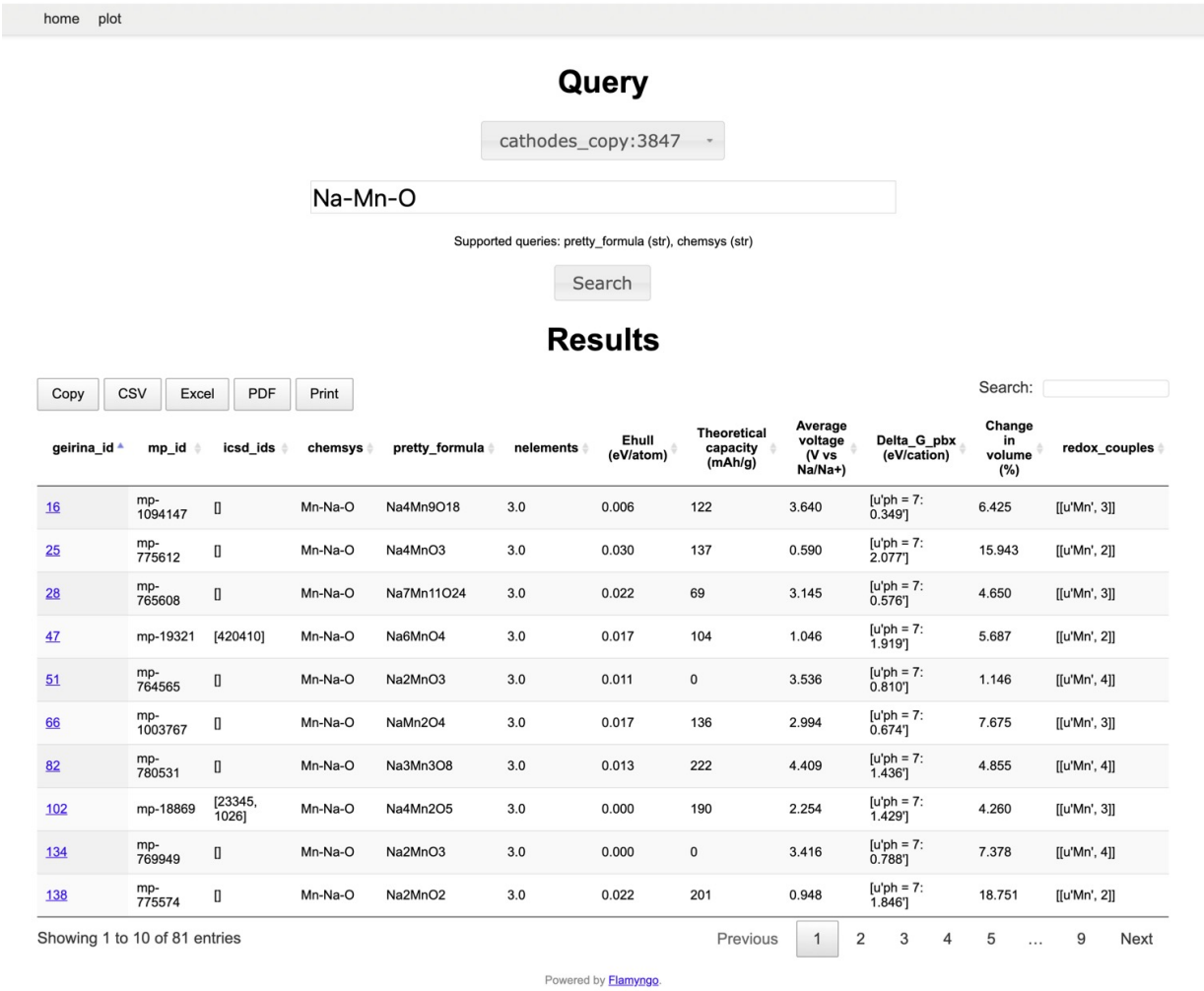

geirina_id	mp_id	icsd_ids	chemsys	pretty_formula	nelements	Ehull (eV/atom)	Theoretical capacity (mAh/g)	Average voltage (V vs Na/Na+)	Delta_G_pbx (eV/cation)	Change in volume (%)	redox_couples
16	mp-1094147	[]	Mn-Na-O	Na4Mn9O18	3.0	0.006	122	3.640	[u'ph = 7: 0.349']	6.425	[[u'Mn', 3]]
25	mp-775612	[]	Mn-Na-O	Na4MnO3	3.0	0.030	137	0.590	[u'ph = 7: 2.077']	15.943	[[u'Mn', 2]]
28	mp-765608	[]	Mn-Na-O	Na7Mn11O24	3.0	0.022	69	3.145	[u'ph = 7: 0.576']	4.650	[[u'Mn', 3]]
47	mp-19321	[420410]	Mn-Na-O	Na6MnO4	3.0	0.017	104	1.046	[u'ph = 7: 1.919']	5.687	[[u'Mn', 2]]
51	mp-764565	[]	Mn-Na-O	Na2MnO3	3.0	0.011	0	3.536	[u'ph = 7: 0.810']	1.146	[[u'Mn', 4]]
66	mp-1003767	[]	Mn-Na-O	NaMn2O4	3.0	0.017	136	2.994	[u'ph = 7: 0.674']	7.675	[[u'Mn', 3]]
82	mp-780531	[]	Mn-Na-O	Na3Mn3O8	3.0	0.013	222	4.409	[u'ph = 7: 1.436']	4.855	[[u'Mn', 4]]
102	mp-18869	[23345, 1026]	Mn-Na-O	Na4Mn2O5	3.0	0.000	190	2.254	[u'ph = 7: 1.429']	4.260	[[u'Mn', 3]]
134	mp-769949	[]	Mn-Na-O	Na2MnO3	3.0	0.000	0	3.416	[u'ph = 7: 0.788']	7.378	[[u'Mn', 4]]
138	mp-775574	[]	Mn-Na-O	Na2MnO2	3.0	0.022	201	0.948	[u'ph = 7: 1.846']	18.751	[[u'Mn', 2]]

Figure 4.1: Screen shot of the web application of NEAD

4.3 Results

4.3.1 statistics of the screening

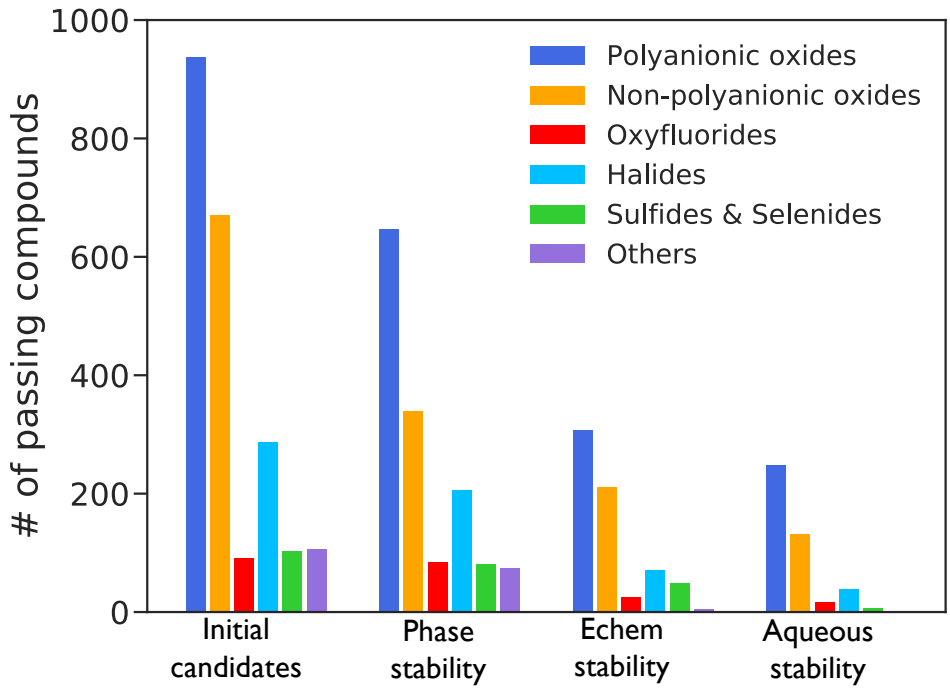

Figure 4.2: Statistics of each screening step

In total, 3847 materials were evaluated for their phase stability, theoretical capacity, average deintercalation voltage and aqueous stability. To better understand the composition-property relationship, we categorized materials according to their anion chemistry: non-polyanionic oxides, polyanionic oxides, oxyfluorides, halides, sulfates, selenides and others (nitrides, Phosphide etc). Figure 4.2 summarizes the number of electroactive materials (Theoretical capacity > 0 mAh/g) that pass the phase stability filter ($E_{hull} < 30$ meV/atom)), electrochemical stability filter (2.30 $<$ average voltage $<$ 3.53 V vs $NaNa^{+}$), aqueous stability filter (aqueous stability $\Delta G_{pbx} < 0.5$ eV/cation at pH = 7).

The phase stability filter returned 1879 compounds with unique compositions for further consideration of the electrochemical stability. Nearly 80 % of the 1879 phase stable materials

that pass the filter are oxides, implying that oxides have a rich chemical space for property optimization.

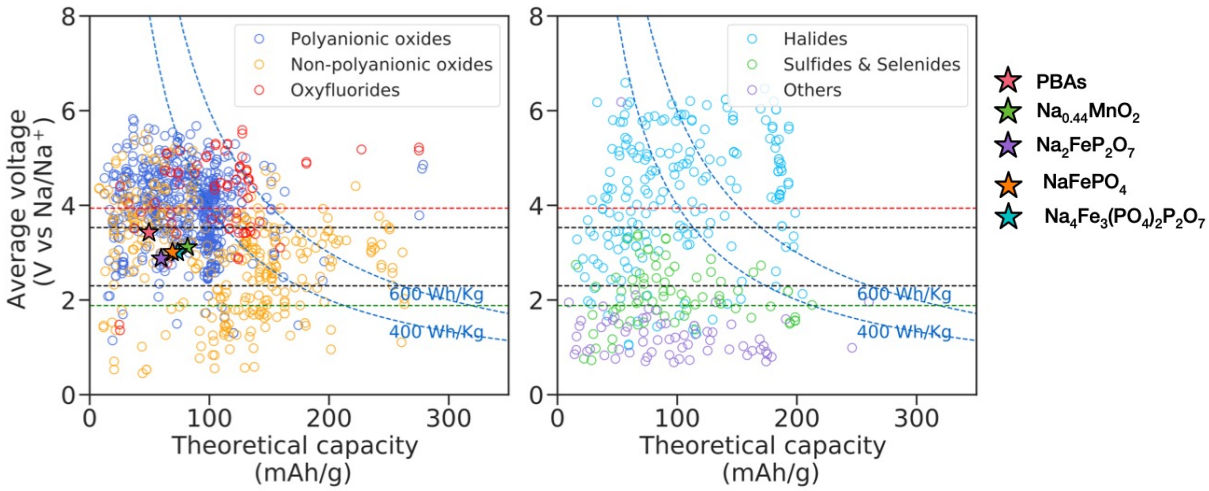

Figure 4.3: Average voltage versus theoretical capacity. Specific energy curves at 400 and 600 Wh/kg are drawn on the plot (blue dashed lines). The black dashed lines indicate the evolution limit of H_2 and O_2 of water at pH = 7. The green and red dashed line refers to the evolution limit of O_2 at pH = 14 and H_2 at pH = 0, respectively.

From Figure 4.3, we can see that the specific energy density of the compounds is largely influenced by anion chemistry. Pure oxides exhibit a wide range of average voltage and theoretical capacity due to its rich chemical space. Explicitly, within the electrochemical stability window, the energy densities of 20 pure oxides are larger than 600 Wh/kg, indicating great potential of oxides as cathodes in ASIBs. Many polyanionic oxides have average voltage higher than the oxygen evolution limit due to inductive effects. The voltages of 59 polyanionic oxides are found to be within the water stability window with theoretical capacities around 100 mAh/g. We note that, the average voltages of most sulfates and other compounds are lower than the evolution limit of hydrogen gas in water, making them less appropriate for applications in ASIBs. Although several halides also exhibit high specific capacity ($>$ 800 mAh/g), their average voltage are beyond the stability window of water. Other than anion chemistry, another important factor that influence the deintercalation voltage of cathodes is the redox couple as analyzed by Hautier et al in phosphate materials.[46]

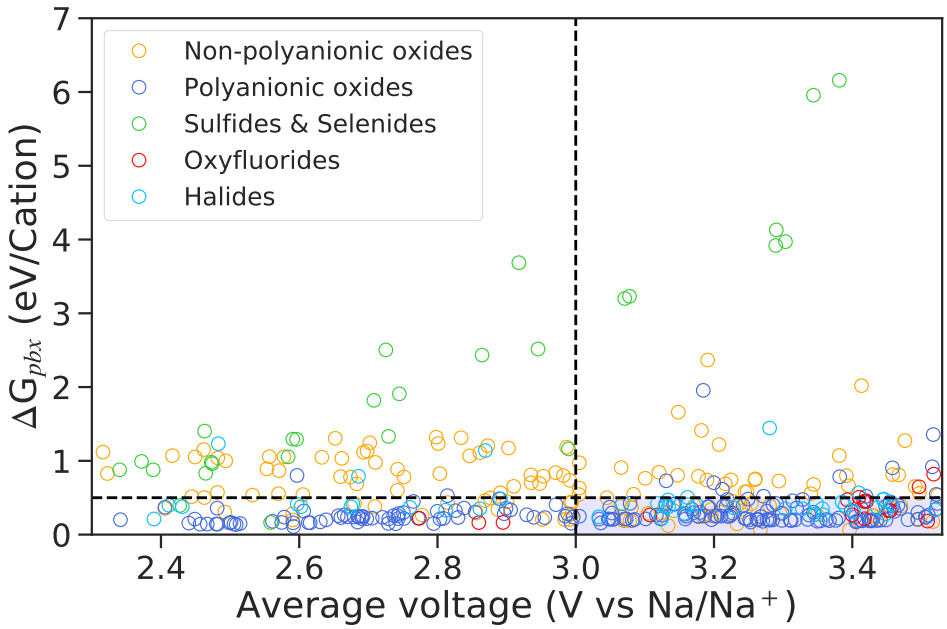

Figure 4.4: Distribution of the calculated ΔG_{pbx} vs average voltage of materials passes the electrochemical stability filter

Figure 4.4 (a) shows the distribution of the calculated ΔG_{pbx} vs average voltage of materials passes the electrochemical stability filter. From the plot, we can see that sulfides and selenides are very unstable against aqueous environment, especially at high voltage ($>$ 3.0 V vs $NaNa^+$). Both oxides, oxyfluorides and halides show good aqueous stability at high voltage, making them promising candidates for cathodes in ASIBs. The aqueous stability of oxides are found to be highly dependent on the type of transition metals. As shown in Figure 4.4 (b), Fe- and Mn-based compounds are shown to be electrochemical active within the electrochemical stability window and stable in aqueous solutions.

In summary, we identified 109 compounds that exhibit good aqueous stability and 78 of them exhibit an average voltage higher than 3V (vs Na/Na^+). Among them, two to alluadite-type structures, two tunneled oxide structures and a group of sidorenkite structures are of great potential for applications in ASIBs with facile Na^+ diffusion channels. The structure of the proposed promising candidate compounds are shown in Figure 4.5 and their electrochemical properties are shown in Table 4.1.

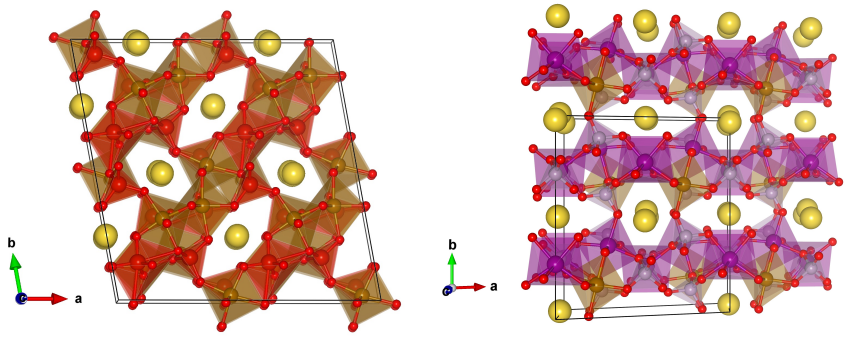

$Na_2V_3(FeO_4)_3$ (P1) $Na_2Mn_2Fe(PO_4)_3$ (C2)

(a) Alluadite structures

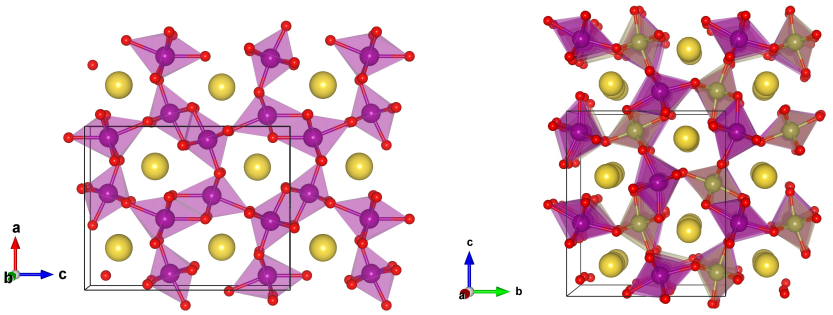

$NaMn_2O_4$ (Pnma) $Na_3Mn_4(TeO_6)_2$ (Pnma)

(b) Tunneled oxides

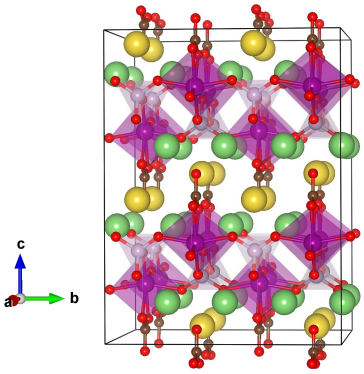

$A_xMe(YO_3)(XO_4)$ ($P2_1/m$)
(A=Na, Li; X=Si, As, P; Y=C, B)

(c) Sidorenkite structures

Figure 4.5: Crystal structures of the promising candidates. (a) Alluadite type structures, (b) Tunneled oxides structures, (c) Sidorenkite structures

.

Table 4.1: Electrochemical properties of promising candidates as cathodes in ASIBs

Formula	Space Group	E_{hull} (meV/atom)	Theoretical capacity (mAh/g)	Average voltage (V vs Na/Na^+)	ΔG_{pbx} (eV/Cation)
$Na_2V_3(FeO_4)_3$	$P1$	0	98.0	3.13	0.07
$Na_2Mn_2Fe(PO_4)_3$	$C2$	6	108	3.73	0.28
$NaMn_2O_4$	*Pnma*	0	136	3.23	0.11
$Na_3Mn_4(TeO_6)_2$	*Pnma*	0	109	2.98	0.10
$Na_3Mn(CO_3)(PO_4)$	$P2_1/m$	0	97	3.25	0.18

4.3.2 Detailed study of proposed promising candidates for cathodes in ASIBs.

In this section, we presents detailed studies of the two most promising candidates, $Na_2V_3(FeO_4)_3$ and $NaMn_2O_4$, as cathodes in ASIBs.

$Na_2V_3(FeO_4)_3$ adopts an alluadite-type structure and is predicted to be stable at 0 K with E_{hull} = 0 meV/atom. The calculated voltage profile of $Na_2V_3(FeO_4)_3$, shown in Figure 4.6 (a), exhibits two voltage steps at around $\sim$ 3.2 and $\sim$ 2.5 V vs $NaNa^+$. We further analyzed the aqueous stability of $Na_2V_3(FeO_4)_3$ cathodes in basic solutions (pH = 12) within the voltage range of 1.8 to 4.0 V vs Na/Na^+. As can be seen in Figure 4.6 (b), the predicted ΔG_{pbx} is well below the threshold of 0.5 eV/cation as the potential E is lower than 3.2 V vs Na/Na^+, indicating its high stability as cathodes in basic electrolyte.

The diffusivity properties of $Na_2V_3(FeO_4)_3$ was examined by NEB calculations and the results are shown in Figure 4.8 and Figure 4.7. In $Na_2V_3(FeO_4)_3$, the Na^+ migration barrier in tunnel 1, which is larger in size, is 268 meV. And the Na^+ migration barrier in the narrower tunnel 2 is much higher to be 470 meV. While being desodiated, in $NaV_3(FeO_4)_3$, the migration barrier of Na^+ is 300 meV. These NEB results indicate that $Na_2V_3(FeO_4)_3$ is of great potential as cathodes in ASIBs with theoretical capacity of 98 mAh/g, comparable to $NaFePO_4$, high aqueous stability in basic electrolyte and facile Na^+ diffusivities.

$NaMn_2O_4$ crystallize in an orthorhombic structure with a space group of *Pnma*. The

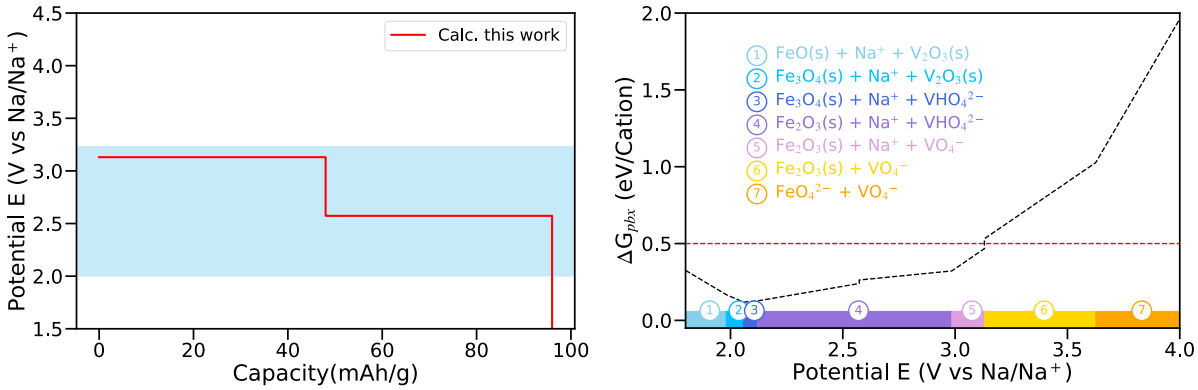

(a) (b)

Figure 4.6: Calculated (a) voltage profile and (b) ΔG_{pbx} as a function of voltage of $NaV_3(FeO_4)_3$ cathodes at pH = 12

.

calculated voltage profile, shown in Figure 4.9 (a), shows a plateau at around $\sim$ 3.25 V vs Na/Na^+, reaching a theoretical capacity of 136 mAh/g. As shown in Figure 4.9 (b), $NaMn_2O_4$ is shown to be stable in neutral electrolyte with a ΔG_{pbx} = 0 eV/cation within the potential range of 3.3 $\sim$ 3.8 V. Furthermore, the tunneled structure of $NaMn_2O_4$ make the migration of Na^+ facile with a energy barrier of only 262 meV. These results shows that $NaMn_2O_4$ is a promising candidates for cathodes in ASIBs due to its large theoretical capacity, high working potential, high stability in aqueous solution and fast Na^+ conductivities.

4.4 Conclusion

In this project, we first developed a constructed Na-ion aqueous electrode database (NAED) using the previously developed screening descriptors for aqueous Na-ion cathodes. There are in total 3847 compounds in NAED and a user-friendly web application has been developed to allow users to efficiently explore the properties of the compounds. We performed automated accurate first principles calculations of key properties for ASIB candidates, including phase stability. average voltage, theoretical capacity, aqueous stability and Na^+ conductivity. In the end, we proposed two candidates, $Na_2V_3(FeO_4)_3$ and $NaMn_2O_4$, for further experimental

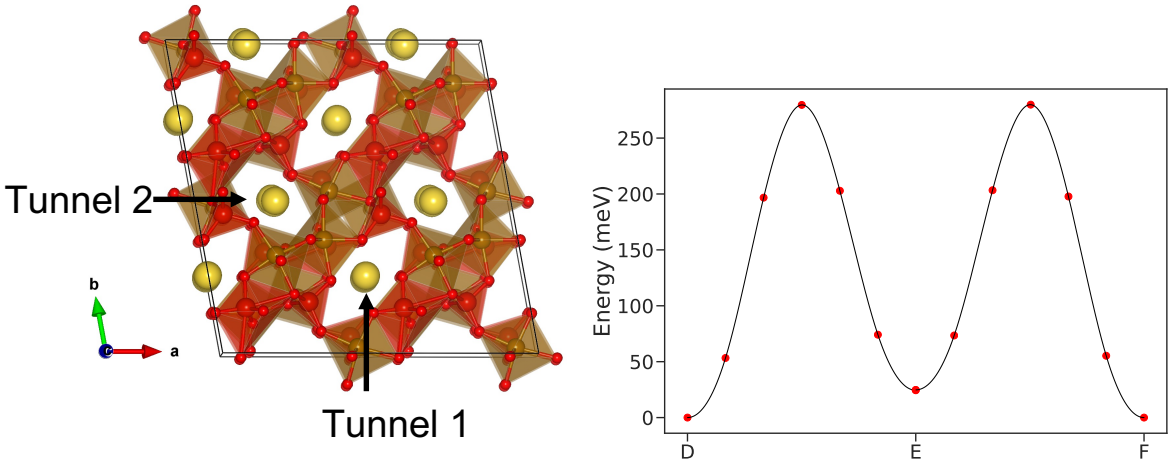

(a)

(b) Tunnel 1

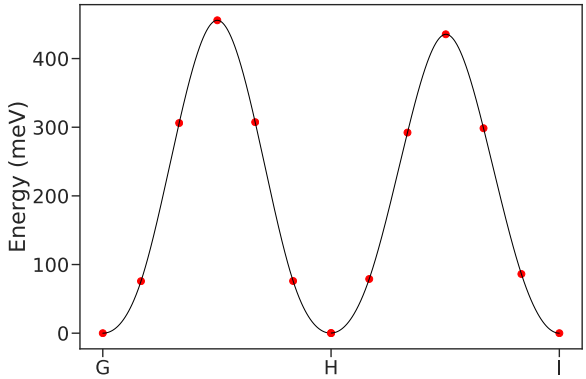

(c) Tunnel 2

Figure 4.7: (a) Crystal structure of $Na_2V_3(FeO_4)_3$ and the diffusion tunnels. Calculated NEB barriers of Na^+ in (b) tunnel 1 and (c) tunnel 2

.

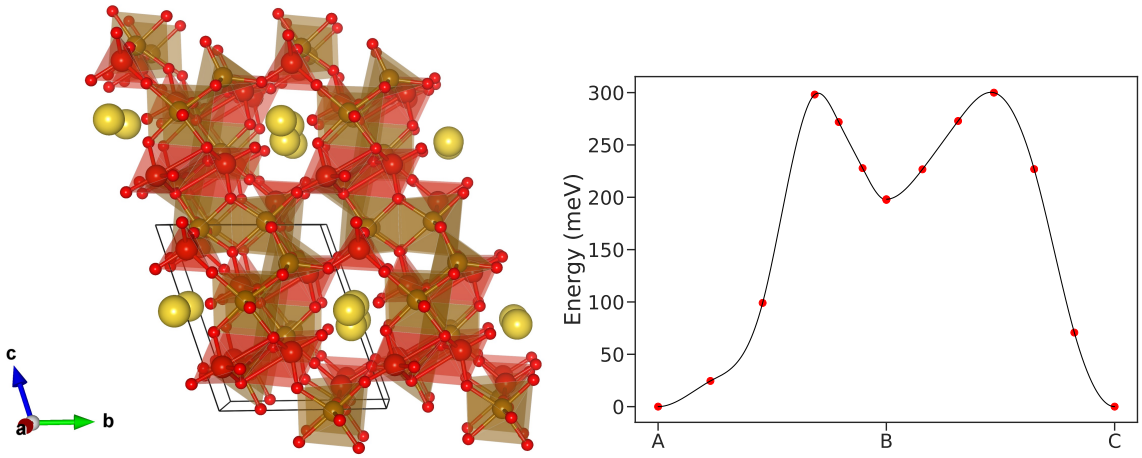

(a) (b)

Figure 4.8: (a) Crystal structure of $Na_2V_3(FeO_4)_3$. (b) Calculated NEB barriers of Na^+

.

synthesis and investigation as cathodes in ASIBs.

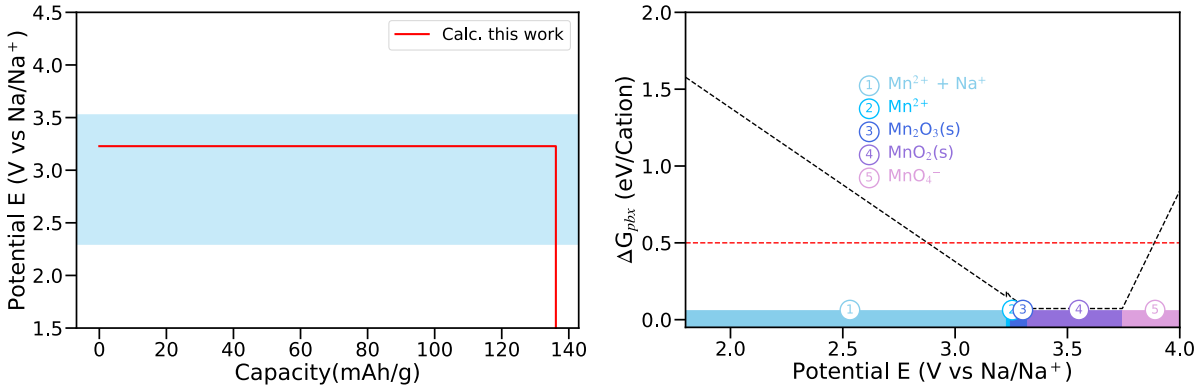

(a) (b)

Figure 4.9: Calculated (a) voltage profile and (b) ΔG_{pbx} as a function of voltage of $NaMn_2O_4$ cathodes at pH = 7

.

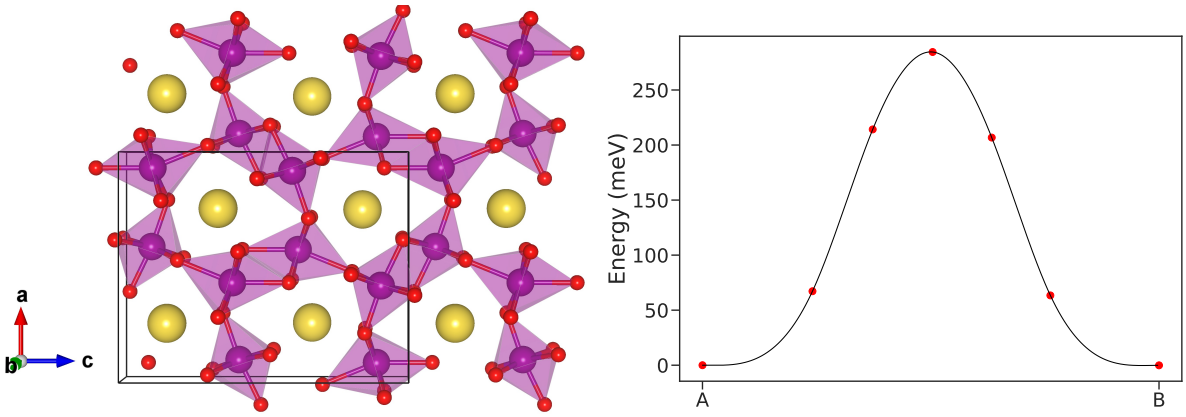

(a) (b)

Figure 4.10: (a) Crystal structure of $NaMn_2O_4$ and the calculated NEB barrier of (b) $NaMn_2O_4$

.

Chapter 5

The Intercalation Chemistry of the Disordered RockSalt $Li_3V_2O_5$ Anode from Cluster Expansions and Machine Learning Interatomic Potentials

5.1 Introduction

Rocksalt oxides have been extensively studied as electrodes for rechargeable lithium-ion batteries (LIBs).[29] As the name implies, the O_2^- anions in rocksalt oxides are arranged in a close-packed face-centered-cubic (fcc) framework, with the cations occupying the tetrahedral and octahedral interstitial sites, as shown in Figure5.1. For instance, the common layered transition metal (M) oxide $LiMO_2$ cathode used in LIBs is formed by an ordered arrangement of Li and M in this framework. In the past decade or so, lithium-rich disordered rocksalt (DRX) oxides have emerged as a promising class of alternative electrode materials with extraordinarily high specific capacities and high rate capabilities.[87, 159, 29, 77]

While DRX materials have been extensively studied as cathodes, relatively few have been explored as anodes.[98, 11, 183] Among the most promising is the DRX-$Li_3V_2O_5$ recently reported by Liu et al. [98]. The DRX-$Li_3V_2O_5$ anode operates at a near-optimal average voltage of ~ 0.6 V vs Li/Li^+ - high enough to alleviate the safety concerns attributed to Li plating that occurs during fast charge/discharge of the commercial graphite anode used in LIBs. At the same time, it is substantially lower than the 1.5 V operating voltage of lithium titanate, thereby yielding a much higher energy density.

Despite its great promise, there remains major ambiguity on the intercalation chemistry of DRX-$Li_3V_2O_5$. Previously, Zheng et al.[186] proposed that the related DRX-$Li_{0.78+x}V_{0.75}O_2$ anode undergoes a conversion-type reaction, in which the single phase material converts to VO_2 and Li_2O as it is discharged to 0.55 V vs Li/Li^+. However, previous density functional theory (DFT) calculations by the present authors attributed the low voltage and high rate capability of DRX-$Li_3V_2O_5$ to a redistributive lithium intercalation mechanism with low energy barriers.[98] These initial conclusions were reached based on 0K DFT calculations with small model cells, which did not fully explore the configurational space of the DRX anode at finite temperatures.

In this work, we revisit the intercalation chemistry of the DRX-$Li_{3+x}V_2O_5$ ($0 \leq x \leq 2$)) using large-scale simulations with machine-learned energy models. Monte Carlo simulations using a fitted cluster expansion model predict that Li primarily inserts into the tetrahedral sites of DRX-$Li_3V_2O_5$ while Li occupancy in octahedral sites remains largely unchanged, in contrast with earlier DFT results. Molecular dynamics (MD) simulations using a machine learning interatomic potential reveal that Li^+ diffusivity reaches the maximum at intermediate states of charge, but sharply decreases at the start of charge/discharge. The exceptionally high rate capability and superior cycling stability of DRX-$Li_3V_2O_5$ anode are a result of facile diffusion of Li ions through tetrahedral - octahedral - tetrahedral pathway, consistent with previous nudged elastic band calculations.

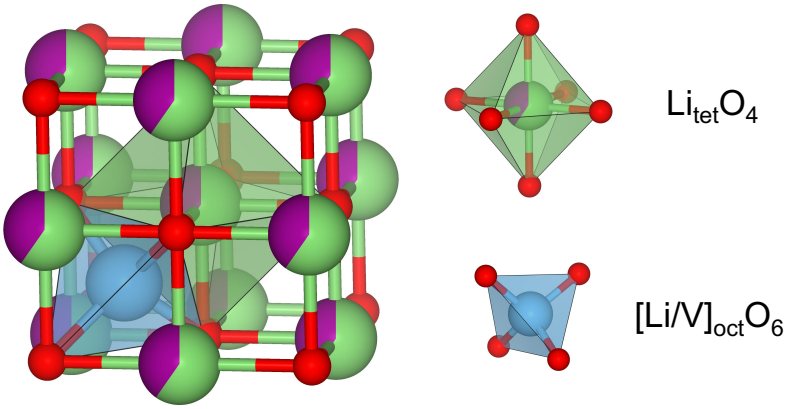

Figure 5.1: The crystal structure of disordered rocksalt $Li_{3+x}V_2O_5$. Red: O^{2-} anions forming an fcc sublattice. Light blue: Li^+ in tetrahedral interstitials. Green/purple: Disordered Li^+/V^{2+-4+} in octahedral interstitials.

5.2 Methods

5.2.1 Structure model

Figure 5.1 shows the crystal structure of DRX-$Li_{3+x}V_2O_5$, which has an fcc lattice with spacegroup $Fm\bar{3}m$. The O^{2-} anions occupy 4*a* sites. The initial composition of $Li_3V_2O_5$ has a cation: anion ratio of 1:1. Based on our previous studies, the lowest DFT energy structure is one where all Li/V cations fully occupy the octahedral 4*b* sites.[98] Henceforth, we will use the anion-normalized composition, e.g., $[Li_{0.6}V_{0.4}]^{oct}O$ for $Li_3V_2O_5$, to emphasize the site occupancies. During discharge, inserted Li^+ also occupy the tetrahedral 8*c* sites, forming $Li_x^{tet}[Li_yV_{0.4}]^{oct}O$.

For more costly DFT and climbing image nudged elastic band (NEB) calculations, a set of 64 special quasi-random structures (SQSs)[191] with formula $Li_{19}V_{13}O_{32}$ (corresponding to $[Li_{0.59375}V_{0.40625}]^{oct}O$) were generated using $2 \times 2 \times 2$ supercells of the conventional rocksalt cubic unit cell. The three relaxed SQS structures with the lowest energies were used for site energy and migration barrier calculations.

5.2.2 Density functional theory calculations

Spin-polarized density functional theory (DFT) calculations were performed using the Vienna *ab initio* simulation (VASP) package within the projected-augmented wave method.[81, 19] The Perdew-Burke-Ernzerhof (PBE) functional[127] was used for the structural relaxation and electronic energy calculations with an effective Hubbard U[34, 60] value of 3.25 eV for V, which is in line with the parameters used in the Materials Project. All calculations were initialized in a ferromagnetic high-spin configuration. A plane wave energy cutoff of 450 eV and a k-point density of at least 100 per reciprocal volume were adopted. The electronic energies and forces were converged to 10^{-4} eV and 0.02 eV Å^{-1}, respectively.

5.2.3 Li site energies

The Li site energies were determined by inserting one Li^+ into each symmetrically distinct tetrahedral site of the three lowest energy SQSs. The Li^{tet} site energies are given by the following expression:

$$E_{Li^{tet}} = E_{Doped} - E_{Host} - E^0_{Li} \tag{5.2.1}$$

where E_{Doped}, E_{Host}, and E^0_{Li} are the DFT calculated energies of the SQS with one Li atom inserted into the tetrahedral site, the SQS and Li metal, respectively.

5.2.4 Cluster expansion

The cluster expansion (CE) lattice model[162, 139, 31, 156] for the DRX $Li_x^{tet}[Li_yV_{0.4}]^{oct}O$ system was parameterized using the Clusters Approach to Statistical Mechanics (CASM) software.[3, 92] The DFT calculated total energies of the structure configurations were mapped into an

expansion of crystal basis functions $\Phi(\vec{m},\bar{\sigma})$ as given by

$$E(\bar{\sigma}) = \sum_{\vec{m}} V(\vec{m})\Phi_{\alpha}(\vec{m},\bar{\sigma}) \tag{5.2.2}$$

where $\Phi(\vec{m},\bar{\sigma}) = \prod_{n=1}^{N} \phi(n, m_n, \sigma_n)$ is a polynomial of site basis functions $\phi(n, m_n, \sigma_n)$, and V($\vec{m}$) are the fitted effective cluster interactions (ECIs).

To fit the CE, the [Li/V/Va]^{oct} and [Li/Va]^{tet} configurations of different compositions were exhaustively enumerated in cubic rocksalt supercells up to a maximum cell size of 25 times the primitive unit cell. It should be noted that V is allowed to occupy only the 4b octahedral sites, given that its occupancy at tetrahedral sites is extremely energetically unfavorable ($E_{V^{tet}} \sim 3$ eV). Li can occupy either the 4b octahedral or 8c tetrahedral sites. We note that only structures with basis deformation < 0.1 were used in the fit, which is a typical threshold used to identify structures that match with the primitive unit cell. The basis deformation is determined by the mean-square atomic displacement relative to the positions of the ideal ions in cubic rocksalt lattice.[3] In total, DFT computed energies of about 4500 symmetrically distinct configurations were used to fit the ECIs. All symmetrically distinct pairs, triplets, and quadruplets in the rocksalt cell within a radius of 7.1Å, 4.1Å and 4.1 Å, respectively, were used to construct the CE model.

The ECIs were obtained from a L_1 regularized linear regression fit with $\alpha = 10^{-8}$ to minimize over-fitting (Figure 5.13). The cross-validation mean absolute error in energies is 8.94 meV atom^{-1}. The 112 non-zero ECIs of the fitted CE model versus cluster size is shown in Figure 5.14(a). DFT calculated and CE predicted formation energy of $Li_{3+x}V_2O_5$ (x = 0.0 - 2.0) is shown in Figure 5.14(b), which shows that the fitted CE model accurately captures the DFT computed ground states (structures with formation energy on the convex hull). The calculated formation energy of $Li_{3+x}V_2O_5$ structures is given by

$$E_{form}[\mathrm{Li_{3+x}V_2O_5}] = E[\mathrm{Li_{3+x}V_2O_5}] - (1-\frac{x}{2})E[\mathrm{Li_3V_2O_5}] - \frac{x}{2}E[\mathrm{Li_5V_2O_5}] \tag{5.2.3}$$

5.2.5 Monte Carlo simulations

Monte Carlo (MC) simulations were performed using the fitted cluster expansion model. A 5×5×5 supercell (2000 sites) was used for these simulations; larger supercells produced similar results (see Figure 5.15). Canonical MC simulations were performed at the $[Li_{0.6}V_{0.4}]^{oct}O$ composition to probe the temperature under which the system undergoes an order-disorder transition.

Semi-grand canonical MC (GCMC) simulations at 300K were performed to study the intercalation of Li ions into the DRX-$Li_3V_2O_5$ structure. In a semi-grand canonical ensemble, the composition and energy of the system with a fixed number of sites were allowed to fluctuate while the temperature (T) and the chemical potentials of Li (μ_{Li}) and V (μ_V) were externally imposed. The chemical potentials were referenced to that of bulk Li and V metals, which have $\mu_{Li} = \mu_V = 0$. The semi-GCMC simulations were carried out by scanning μ_{Li} with a step of $\delta\mu_{Li}$ = 0.01 eV at constant μ_V within the chemical potential ranges of $-2.0 \leq \mu_{Li} \leq 0.0$ and $-2.0 \leq \mu_V \leq 0.0$ at 300 K. The initial disordered structures were obtained from equilibrated semi-GCMC simulations by heating the system from 5 K up to 1500 K at fixed chemical potentials. In this work, the semi-GCMC simulations were performed on only Li and vacancy occupancy in the tetrahedral and octahedral sites, while all V ions were fixed in the initial equilibrated octahedral sites due to the large V migration barriers.

The voltage of an electrochemical cell was related to the Li chemical potential of the electrodes according to the Nernst equation:

$$V = -(\mu_{Li} - \mu_{Li}^0)/e \tag{5.2.4}$$

where μ_{Li} is the chemical potential of Li in DRX-$Li_{3+x}V_2O_5$, μ_{Li}^0 is the reference chemical potential of Li metal and e is the elementary charge.

5.2.6 Moment tensor potential

A machine learning interatomic potential (ML-IAP) based on the moment tensor potential (MTP) formalism[110] was developed for DRX-$Li_{3+x}V_2O_5$ using a protocol similar to that developed by Qi et al.[132] for lithium superionic conductors. The initial training structures included DFT calculated ground state structures in the Li-V-O chemical space (supercells of Li_2O, Li_3VO_4, LiV_2O_5 and $LiVO_2$ with lattice parameters larger than 10 Å). To further sample the energy landscape of different Li/V arrangements, a set of SQSs with compositions $Li_{19}V_{13}O_{32}$ ($[Li_{0.59375}V_{0.40625}]^{oct}O) \approx Li_3V_2O_5$), $Li_{25}V_{13}O_{32}([Li_{0.1875}]^{tet}[Li_{0.59375}V_{0.40625}]^{oct}O) \approx Li_4V_2O_5$) and $Li_{32}V_{13}O_{32}([Li_{0.40625}]^{tet}[Li_{0.59375}V_{0.40625}]^{oct}O) \approx Li_5V_2O_5$) were generated in $2\times2\times2$ supercells of the conventional rocksalt cubic unit cell. It should be noted that changes in the occupancy of tetrahedral and octahedral sites in SQSs can occur upon DFT relaxation. The SQS with the lowest energy configuration of each composition were included in the fitting procedure.

Non-spin polarized *ab initio* molecular dynamics (AIMD) simulations using NVT ensembles were performed on relaxed supercells of all initial structures with a plane-wave energy cut-off of 280 eV and Gamma *k*-point. To diversify the sampled local environments, the simulations were carried out at three strains (0, $\pm$ 0.05) and four temperatures (300 K - 1200 K at an interval of 300 K). All simulations were performed for at least 30 ps with a 2 fs timestep using Nose-Hoover thermostat[109, 56]. The training structures were collected from 15 ps-equilibrated runs at 0.1 ps intervals, and more accurate energies and forces were obtained by static self-consistent calculations with a *k*-point density of at least 100 per reciprocal volume and an energy cutoff of 520 eV.

5.2.7 Molecular dynamics simulations

Molecular dynamic (MD) simulations were performed in the NpT ensemble to investigate the Li^+ diffusion properties of DRX-$Li_3V_2O_5$ using the fitted MTP potential. The time step of all

MD calculations was set to 1 fs, and the total simulation time was at least 1 ns. The diffusivity (D_{Li^+}) of Li^+ was calculated by performing a linear fitting of the mean square displacement (MSD) versus $2dt$:

$$D = \frac{1}{2dt} < [\Delta r(t)]^2 > \tag{5.2.5}$$

where d is the dimensionality factor, which equals 3 for bulk structures. $< [\Delta r(t)]^2 >$ is the average MSD over a time duration t. The activation energy of E_a was determined by the Arrhenius relationship,

$$D = D_0 exp(-E_a/kT) \tag{5.2.6}$$

where D_0 is the maximum diffusivity at infinite temperature, k is the Boltzmann constant and T is the temperature.

All the training, evaluations and MD simulations were performed using MLIP[143, 42], Large-scale Atomic/Molecular Massively Parallel Simulator (LAMMPS)[157] and the open-source Materials Machine Learning (maml) Python package[27].

5.2.8 Diffusion barriers

The migration barriers of Li^+ and V^{n+} (n=3, 4) vacancy were calculated using the climbing image nudged elastic band (CI-NEB) method[51, 50]. All NEB calculations were performed in three SQSs with the lowest DFT total energy created in the previous sections. For Li^+ migration barriers, the starting point of each NEB calculation was determined by inserting one Li^+ into the tetrahedral site, and then the structure was fully relaxed. Five linearly interpolated intermediate images were used to generate the initial guess for the minimum energy path. For Li_{tet} in varied local environments, the energy barriers for the Li^+ hoping were calculated in three configurations with the lowest Li_{tet} site energy. The kinetically resolved activation (KRA)[161] Li^+ migration barrier (ΔE_{KRA}), which is independent of hop direction, was determined by the

following expression:

$$\Delta E_{KRA} = E(\sigma_t) - \frac{1}{2}(E(\sigma_i + E(\sigma_f)) \tag{5.2.7}$$

where $E(\sigma_t)$, $E(\sigma_i$ and $E(\sigma_f)$ refer to the energy of the activated transition state, the initial state and the end state from the CI-NEB calculations, respectively. The PBE functional without Hubbard U was adopted to avoid the possible mixing of the diffusion barrier with a charge transfer barrier. [116] The force and energy convergence criterion was 0.05 eV/Å and 5×10^{-5} eV.

5.3 Results

5.3.1 Li-V-O phase diagram

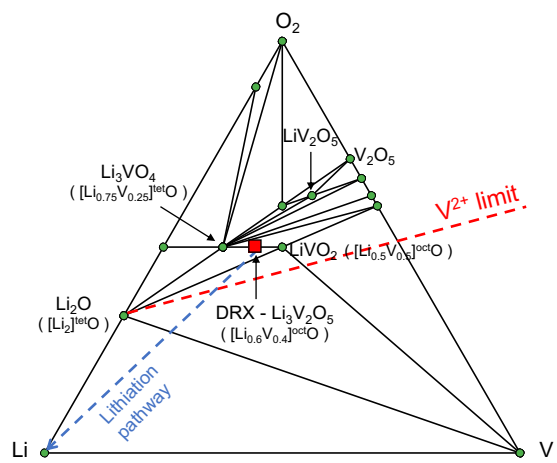

Figure 5.2: Calculated phase diagram of Li-V-O chemical system at 0 K. The green circles refer to ground states and the red square refers to the metastable phase. The red dashed line refers to the limit of V^{2+} oxidation state. The blue dashed line refers to the lithiation pathway in DRX-$Li_3V_2O_5$.

Figure 5.2 shows DFT-calculated Li-V-O phase diagram at 0 K. $Li_3V_2O_5$ ($[Li_{0.6}V_{0.4}]^{oct}O$), represented by the red square, is unstable at 0K relative to $LiVO_2$ and Li_3VO_4. Both ordered layered and DRX-$LiVO_2$ as well as ordered Li_3VO_4 have been explored as potential LIB anodes[6, 90, 14]. All three electrode materials have a cation: anion ratio of 1:1 and differ purely in their Li: V ratio and therefore active redox couple. Li_3VO_4 has a formal vanadium oxidation state

of 5+, and all cations are ordered in tetrahedral sites. It can therefore be represented using the anion-normalized composition of $[Li_{0.75}V_{0.25}]^{tet}O$. $LiVO_2$, on the other hand, has full octahedral occupancy like $Li_3V_2O_5$ and a formal V oxidation state of 3+. It can therefore be represented using the anion-normalized composition of $[Li_{0.5}V_{0.5}]^{oct}O$. It should be noted that Li_2O ($[Li_2]^{tet}O$) also has a cubic rocksalt structure with full occupancy in the tetrahedral sites and a cation: anion ratio of 2.

During charging, lithiation of $[Li_{0.6}V_{0.4}]^{oct}O$ occurs along the pathway indicated by the dashed blue line. The thermodynamically most favorable pathway is a conversion reaction given by the phase triangle of Li_2O-Li_3VO_4-$LiVO_2$($[Li_2]^{tet}O$-$[Li_{0.75}V_{0.25}]^{tet}O$-$[Li_{0.5}V_{0.5}]^{oct}O$). However, kinetic considerations may favor lithium insertion instead of conversion, as has been observed experimentally.[98] The ultimate limit of insertion into the rock salt $Li_{1-x}V_xO$ is given by the red dashed line representing $Li_{2-2x}V_xO$, i.e., a V^{2+} oxidation state. For a V cation content of 0.4, i.e., $Li_3V_2O_5$, this limit is given by $Li_{1.2}V_{0.4}O$ or $Li_6V_2O_5$. Experimentally, this limit is never reached and the highest lithiated state has a composition of $Li_1V_{0.4}O$ or $Li_5V_2O_5$.[98]

Li^+ insertion into the $Li_3V_2O_5$ anode at 0 K were studied by DFT calculations. Figure 5.3(a) shows the DFT calculated pseudo-binary $Li_3V_2O_5$-$Li_5V_2O_5$ phase diagram with the candidate structures colored in terms of their basis deformation. The larger the basis deformation, the greater the deviation of the DFT-relaxed structure from the ideal cubic rocksalt lattice. At $x \geq 0.5$, the DFT ground states comprise phases that are highly distorted (basis deformation > 0.1) from the parent cubic rocksalt lattice; the cubic phases (basis deformation ≤ 0.1) are metastable. A Li site occupancy analysis of DFT ground states structures (Figure 5.3(b)) indicates that redistribution of Li from octahedral sites to tetrahedral sites occurs at x ~ 0.75, where the occupancy of Li^{oct} sharply decreases to 0.1 and the occupancy of Li^{tet} increases to 0.65. These results are qualitatively in line with previous DFT studies.[98] However, this redistribution of Li is accompanied by a considerably large volume change ($\sim 20\%$) and lattice distortion, contradicting with the experimental observations that the anode retains a stable cubic lattice with a small

volume change of 5.9%.[98] In contrast, the Li site occupancy analysis of metastable cubic phases (Figure 5.3 (c)) suggests that a redistribution of Li only takes place at the end of charging. The volume change of these metastable cubic phases ranges from 8 to 15%, which is close to the experimental results.[98]. It is therefore essential to consider the metastable phases for assessing the thermodynamic properties of DRX using methods beyond DFT.

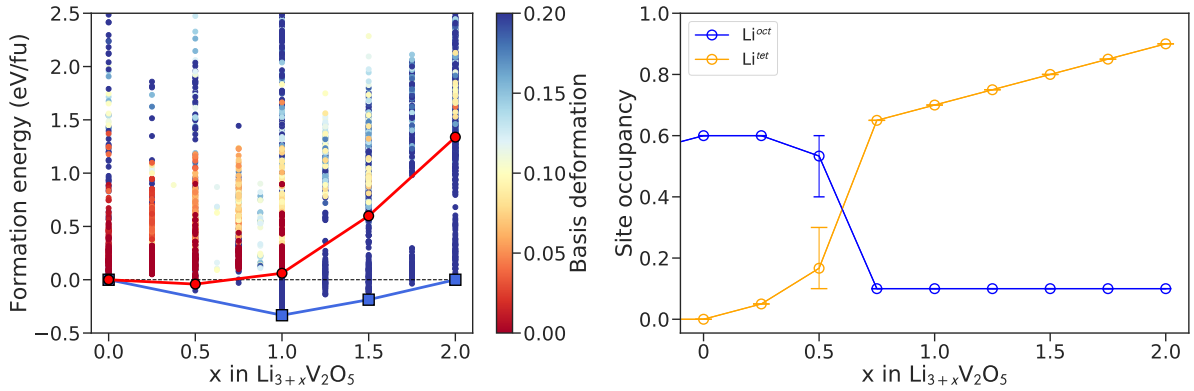

(a) DFT calculated pseudo-binary $Li_3V_2O_5$-$Li_5V_2O_5$ compound phase diagram.

(b) Li site evolution of ground state highly-distorted phases

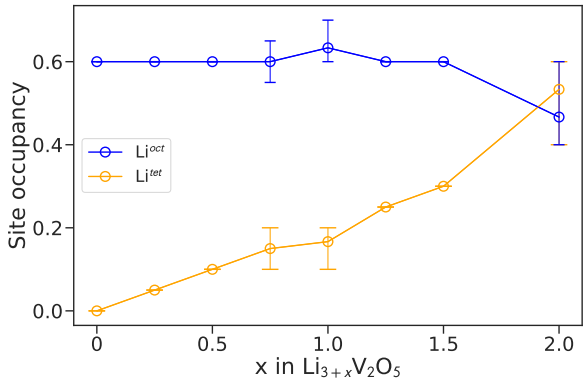

(c) Li site evolution of metastable cubic phase

Figure 5.3: (a) DFT calculated pseudo-binary $Li_3V_2O_5$-$Li_5V_2O_5$ compound phase diagram. The configurations are colored in terms of their basis deformation. The red line represents the convex hull of the cubic phase, i.e., structures with low basis deformation (< 0.1). The blue line represents the convex hull of all the DFT relaxed structures. (b) Evolution of the occupancy of Li^{oct} and Li^{tet} within $Li_3V_2O_5$ - $Li_5V_2O_5$ at 0 K. (c) Evolution of the occupancy of Li^{oct} and Li^{tet} within $Li_3V_2O_5$ - $Li_5V_2O_5$ in cubic phase. At each composition, the three lowest-energy structures were used for site occupancy calculations. The average values with error bars are shown in the plot. The most stable structures of ground states and metastable cubic phase of $Li_{3+x}V_2O_5$ (x = 0, 1, 2) are shown in Figure 5.12.

5.3.2 Order-disorder transition of cubic $Li_3V_2O_5$

To further understand the effect of cation disorder in DRX-$Li_3V_2O_5$ anode, we performed Monte Carlo simulation using the fitted CE model. Figure 5.4 shows the calculated formation energy E_f and specific heat capacity C_v as a function of temperature from MC simulations with the fitted CE model. The critical temperature (T_c) of order-disorder phase transition is predicted to be $\sim$ 1000 K, which is somewhat lower than that experimentally measured from $LiVO_2$ (1775 K)[53]. At temperatures below T_c, both E_f and C_v remain relatively constant with temperature, characteristic of a highly ordered crystal. At T_c, a discontinuous increase in the E_f and a sharp peak in the configurational C_v is observed, indicative of a phase transition taking place. The calculated average configurational specific heat capacity of the DRX phase (T $>$ 1000 K) is 2.973 J mol^{-1} K^{-1}. Figure 5.4 (b) shows two sampled configurations from the equilibrated MC simulations at 500K (ordered phase) and 1500 K (fully disordered phase). At temperatures above T_c, Li/V disordering occurs mostly on the octahedral 4*b* sites and only a small fraction of Li ($\sim$ 0.0125 %) ions occupy the tetrahedral sites. These observations are consistent with the fact that the DRX is synthesized under the application of an external driving force, such as high temperatures, ball milling, or electrochemical lithiation.[33, 98, 11]

5.3.3 Lithium intercalation mechanism and predicted voltage profile

The intercalation mechanism of Li^+ into DRX structures is strongly affected by the distribution of the tetrahedral sites with different local environments and connectivity. The Li in tetrahedral sites share faces with four neighboring octahedral sites. As shown in previous works,[87, 159, 98, 29] the Li/transition metal occupancy of these neighboring octahedral sites have a strong influence on the local site occupancies and Li^+ migration barriers. The local environment of a tetrahedral site can be denoted by n-V (n = 0 $\sim$ 4), where n represents the number of face-shared V atoms. Figure5.5 (a) shows the distribution of the calculated Li^{tet} site

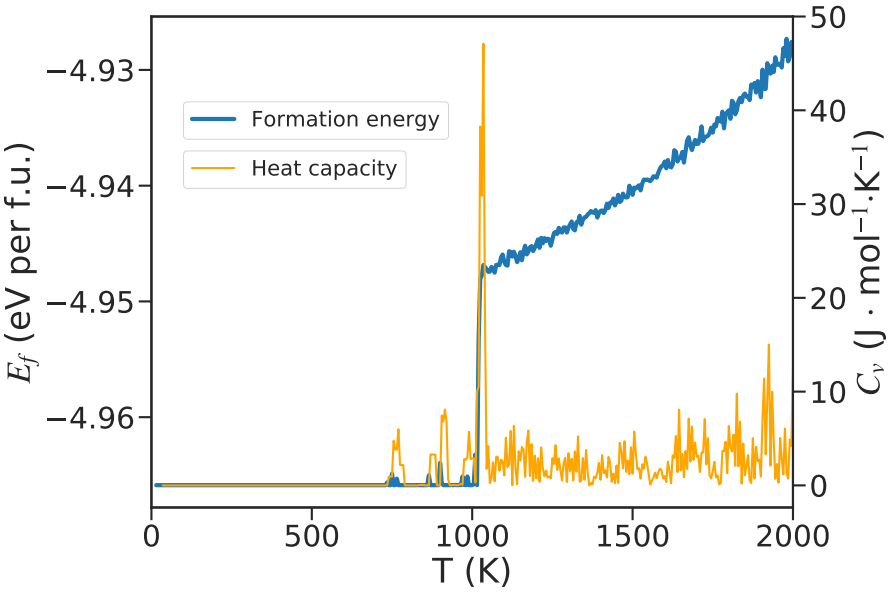

(a)

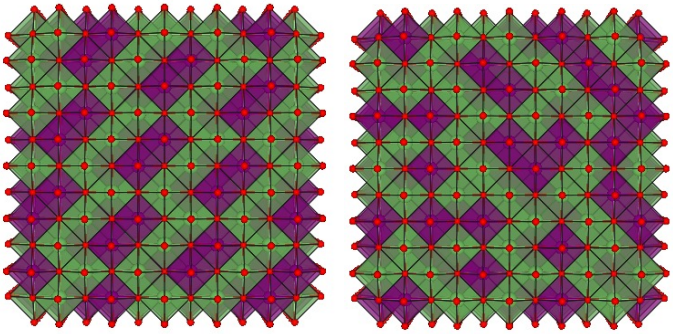

(b) T = 500 K (c) T = 1500 K

Figure 5.4: (a) Calculated formation energy (E_f) and heat capacity (C_v) as a function of temperature (T). Structures from equilibrated Monte Carlo simulations at (b) 500 K and (c) 1500 K. The MC simulations were initialized in the DFT calculated most energetically stable $Li_3V_2O_5$ structure, in which all Li and V ions occupy the octahedral sites. The initial configuration was then heated from 10 K to 2000K in intervals of = 10 K. At each temperature, the properties were then obtained by averaging the results from 1000 equilibrated MC runs. The configurational heat capacity C_v is given by the second derivative of the formation energy E_f with respect to temperature T, $C_v = \partial^2 E_f / \partial^2 T$.

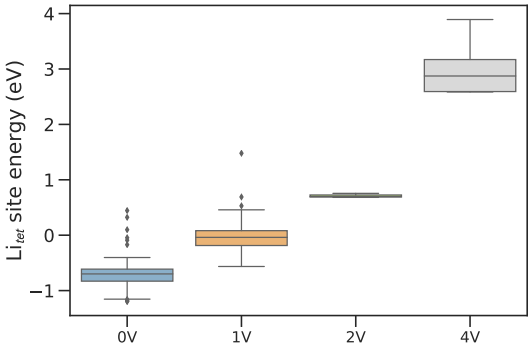

(a)

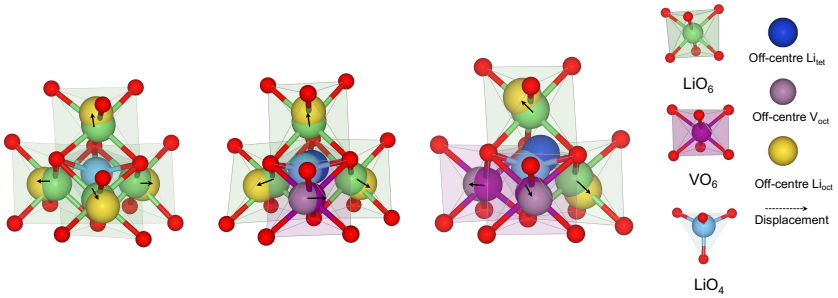

(b)

Figure 5.5: (a) Site energy of Li^{tet} in various local environments (i.e., diffusion sites). (b) 0-V, 1-V, and 2-V tetrahedral Li insertion sites and off-center displacements of the neighboring octahedral sites and the inserted tetrahedral Li sites.

energies in 0-V, 1-V, 2-V and 4-V clusters in the three SQSs with the lowest DFT energies. The Li_{tet} site energy in 3-V is not presented because Li_{tet} is unstable in this local environment and the electrostatic repulsive effect between the inserted Li_{tet} and the neighboring Li^{oct} ion caused local environment rearrangements during structure relaxations. In general, the Li_{tet} site energy and the distortion of neighboring LiO_6 octahedra increase with the number of neighboring V atoms. The Li insertion into 0-V sites is the most energetically favourable and the four neighboring Li_{oct} sites are displaced off-center by 0.4-0.5 Å due to the electrostatic repulsion between Li^+ (Figure 5.5(b)). The 1-V Li_{tet} site energy is on average 660 meV higher than that of 0-V sites and the inserted Li displaces $\sim$ 0.4 Å from the center of the tetrahedron in the direction away from the V ions. The off-center displacements of neighboring Li^{oct} are 0.3-0.6 Å, whereas that for the neighboring V^{oct} are only 0.16 Å. The 2-V Li^{tet} sites are relatively energetically unstable and is positioned $\sim$ 0.4 Å away from the tetrahedral center due to large repulsive interactions between V^{3+}/V^{4+} and Li^+. The neighboring Li atoms are pushed 0.5 - 0.6 Å away from the center of the octahedron, causing large distortions in the local lattice structure.

The migration of V vacancies between neighboring octahedral sites was also investigated by introducing one V^{oct} vacancy in the configuration with the lowest V^{oct} vacancy energy. The average V^{oct} migration barrier is extremely high, up to 2100 meV (Figure 5.11). This suggests that V ions in DRX-$Li_3V_2O_5$ are unlikely to migrate during charge/discharge under operating conditions.

Figure 5.6 (a) shows the calculated voltage profile by GCMC simulations. The GCMC-predicted voltage profile exhibits a solid solution-like behavior and is in good agreement with the experimentally-measured voltage profile.[98] Li starts to insert into DRX-$Li_3V_2O_5$ at $\sim$1.43 V and the predicted voltage profile exhibits two voltage steps at around 0.9 and 0.25 V vs Li/Li^+. As the voltage decreases to 0.01 V, the predicted average composition of the lithiated anode is $Li_{5.11}V_2O_5$, close to that observed in experiments ($Li_{4.86}V_2O_5$)[98]. In contrast, due to the limited supercell sizes used, DFT calculations[98] predict a multiple voltage steps at 0.98V, 0.54 V, 0.46

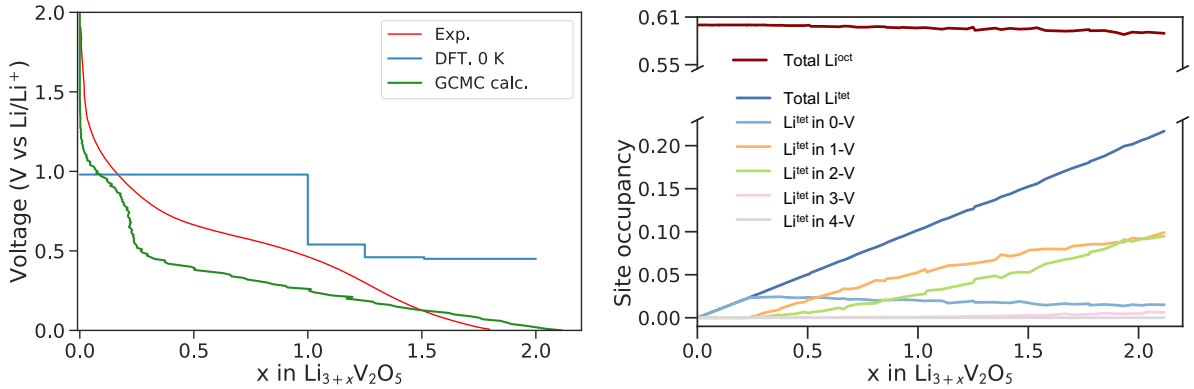

(a) (b)

Figure 5.6: (a) Calculated voltage as a function of Li content x in $Li_{3+x}V_2O_5$. The experimental and DFT (0 K) results are extracted from Liu et al. [98] (b) Evolution of Li site occupancies in tetrahedral and octahedral sites upon Li insertion from semi-GCMC simulations with the position of V^{oct} fixed.

V and 0.45 V.

Figure 5.6 (b) shows the evolution of Li site occupancies in DRX-$Li_{3+x}V_2O_5$ as a function of inserted Li content x. It should be noted that as an anode, insertion of Li into the DRX-$Li_3V_2O_5$ corresponds to the charging process in a typical Li-ion battery. As Li ions are introduced into the tetrahedral sites, the Li occupancy in the octahedral sites first remains constant at around 0.6 until $x \approx 0.3$, following which there is a small, gradual reduction in Li^{oct} occupancy. The insertion of Li ions into the tetrahedral sites consists of two steps. Li^+ first intercalate into 0-V sites, which is consistent with the energies predicted by DFT calculations (Figure5.5 (a)) and previous results that the insertion into 0-V tetrahedral sites is the most energetically favorable.[98] This process coincides with the formation of the first plateau at around 0.9 V on the voltage profile. At x = 0.31, 0-V sites are fully occupied and further lithiation insertion occurs in the energetically less favorable 1-V and 2-V sites. The occupancy of 1-V and 2-V sites rise to $\sim$ 0.1 till the end of charge. At the end of charge, only $\sim$0.1% 3-V tetrahedral sites are occupied, and all 4-V sites are vacant.

Table 5.1: Lattice parameters and densities of the structures in the training set (zero strain) relaxed with the trained MTP at 0K, in comparison with DFT calculated lattice parameters and densities at 0K. Values in brackets are the percentage differences between the MTP and DFT computed values, respectively.

Composition	a (Å)	b (Å)	c (Å)	Density (g/cm^3)
$LiVO_2$	3.02 (1.75 %)	5.16 (-1.24 %)	5.25 (1.19 %)	3.88 (1.69 %)
LiV_2O_5	6.75 (0.98 %)	7.68 (0.41 %)	7.58 (-1.65 %)	3.18 (-0.28 %)
Li_3VO_4	5.06 (0.48 %)	5.54 (0.51 %)	6.37 (-0.41 %)	2.52 (-0.57 %)
Li_2O	3.30 (0.056 %)	3.29 (0.056 %)	3.29 (0.056%)	1.96 (-0.17%)
DRX-$Li_3V_2O_5$	8.46 (0.66 %)	8.45 (1.26 %)	8.42 (0.84 %)	3.60 (-2.71 %)
DRX-$Li_{3.9}V_2O_5$	8.62 (1.26 %)	8.62 (1.25 %)	8.62 (1.24 %)	3.18 (-3.66 %)
DRX-$Li_5V_2O_5$	9.48 (3.12 %)	7.72 (-1.03 %)	9.43 (2.519 %)	3.36 (-4.42 %)

5.3.4 Validation of moment tensor potential

The mean absolute errors (MAEs) of training energies and forces (shown in Figure 5.7) of the fitted MTP are 3.15 meV/atom and 0.15 eV/Å, respectively, comparable to those of other MTPs in the literature.[192, 165] As shown in Table 5.1, the MTP is able to accurately reproduce the lattice parameters and densities of training structures, with errors of within $\pm$ 3.12% and $\pm$ 4.42% relative to DFT values, respectively.

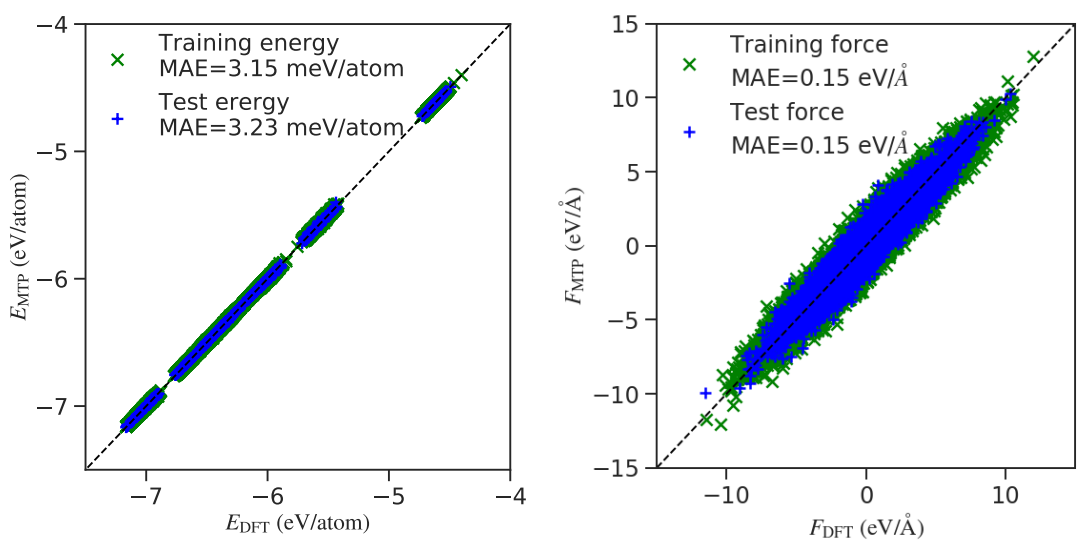

(a) (b)

Figure 5.7: Plots of the (a) MTP predicted versus DFT energies and (b) MTP predicted versus DFT forces with lev_{max} = 20.

5.3.5 Diffusion properties

MD simulations were carried out to investigate the Li^+ diffusion in the DRX-$Li_{3+x}V_2O_5$ anode as a function of Li concentration using the fitted MTP potential. The initial structures were obtained from the equilibrium semi-GCMC simulations in the preceding section. Figure5.8 shows the calculated diffusivity D_{Li^+} and activation energy E_a as a function of Li content x in DRX-$Li_{3+x}V_2O_5$ at room temperature (300 K). The Arrhenius plot from NpT MD simulations for each composition is shown in Figure 5.16. At the start of lithiation, a sharp increase in D_{Li^+} to $\sim 10^{-9}$ cm^2 s^{-1} with a corresponding decrease in E_a from 450 meV to 280 meV is observed up to $x = 0.5$. However, further lithiation results in a gradual decrease in D_{Li^+} from $\sim 10^{-9}$ cm^2 s^{-1} to $\sim 10^{-11}$ cm^2 s^{-1} accompanied by an increase in E_a from 280 to 460 meV. The calculated diffusivities are generally similar to that in graphite ($10^{-11} \sim 10^{-7}$ cm^2 s^{-1})[88, 121, 129], but much lower than that in ($\sim 10^{-6}$ cm^2 s^{-1} at high temperature range from 1133 K to 1173 K)[49, 154] in $Li_4Ti_5O_{12}$(LTO) anodes.

To further investigate the Li^+ diffusion mechanisms and pathways, we analyzed the Li^+ trajectories from 1 ns MD simulations at 600 K and the results for selected configurations are presented in Figure 5.8 (b). For $x < 1.5$, Li^+ ions migrate via a cooperative tetrahedral - octahedral - tetrahedral ("t-o-t") mechanism, in agreement with previous NEB calculations.[98] For $x > 1.5$, the increased amount of inserted Li^+ in tetrahedral sites and vacancies in octahedral sites may result in Li^+ migration between neighboring tetrahedral - tetrahedral ("t-t") sites via the vacant octahedral sites along with the "t-o-t" migration.

To confirm the above results, DFT NEB calculations were also performed to calculate the Li^+ migration barriers. Similar to the previous NEB calculations,[98] a cooperative mechanism of Li^+ migration was considered, where the tetrahedral Li^+ migrates to a neighboring octahedral site and the octahedral Li^+ migrates into another neighboring tetrahedral site (Figure 5.9 (a)). Here, we consider cooperative migration that occurs between corner-sharing and opposing tetrahedral sites, given that migration between edge-sharing tetrahedral sites is extremely energetically unfavorable

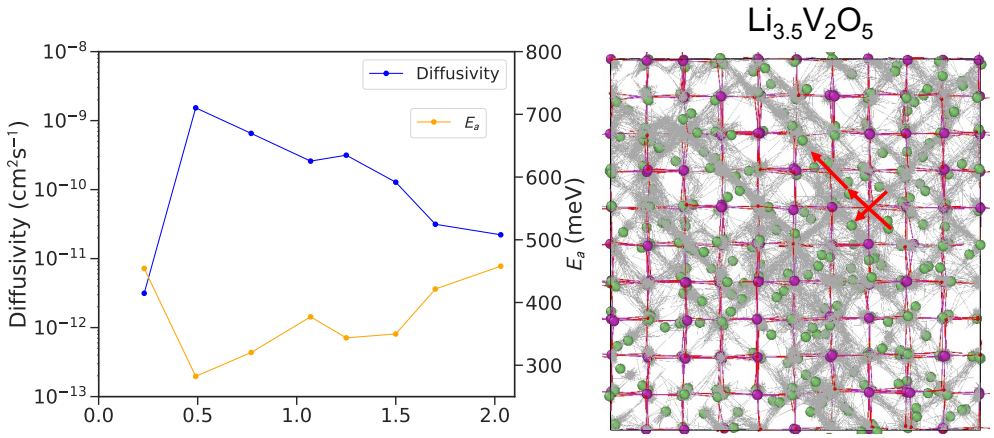

(a) (b)

Figure 5.8: (a) Calculated diffusivity and activation energy of Li^+ in DRX-$Li_{3+x}V_2O_5$ as a function of Li content at 300 K. (b) Li trajectories (colored as grey) from MD simulations of $Li_{3.5}V_2O_5$ at 600 K, projected in the crystallographic a-b planes. Illustrations of "t-o-t" migration mechanisms of Li^+ are shown in red arrows. The green balls, purple balls, and red balls represent Li, V, and O atoms, respectively.)

due to the close proximity of the Li during migration (Figure 5.18(c) and 5.19(c)). Figure5.9 shows the calculated Li^+ migration barriers between connected 0-V/1-V sites. We note that migration from 2-V site to 0-V and 1-V sites are energetically downhill due to the large site energy differences (Figure 5.21). The cooperative migration of Li^+ via opposing "t-o-t" paths exhibits the lowest calculated average energy barriers, ranging from 230 to 340 meV in 0-V and 1-V sites. The average energy barriers of Li^+ transport through corner-sharing 't-o-t' pathways exhibit higher energy barriers of 334 to 628 meV. In general, the migration barriers of Li^+ increase as more V atoms gather around the local environment of tetrahedral Li^+ sites. At the end of discharge, the formation of vacancies at the octahedral sites allows for direct hopping of Li^+ from one tetrahedral site to its next edge-sharing tetrahedral site ('t - t'), as illustrated in Figure 5.23, with a low energy barrier of 241 meV. These results are in line with the activation energies obtained by MD simulations and previous theoretical studies[98] that the facile migration of Li^+ across opposing 't-o-t' pathways results in high rate capability of DRX-$Li_{3+x}V_2O_5$ anode. In previous studies[98], Li^+ hopping via 0-V sites is the only mechanism that was considered while our results show that Li^+ migration in 0-V, 1-V and 2-V sites is facile. Similar results have also

been observed in LTO anodes that the transportation of Li^+ in face-sharing octahedral-tetrahedral motif contributes to fast kinetics.[187]

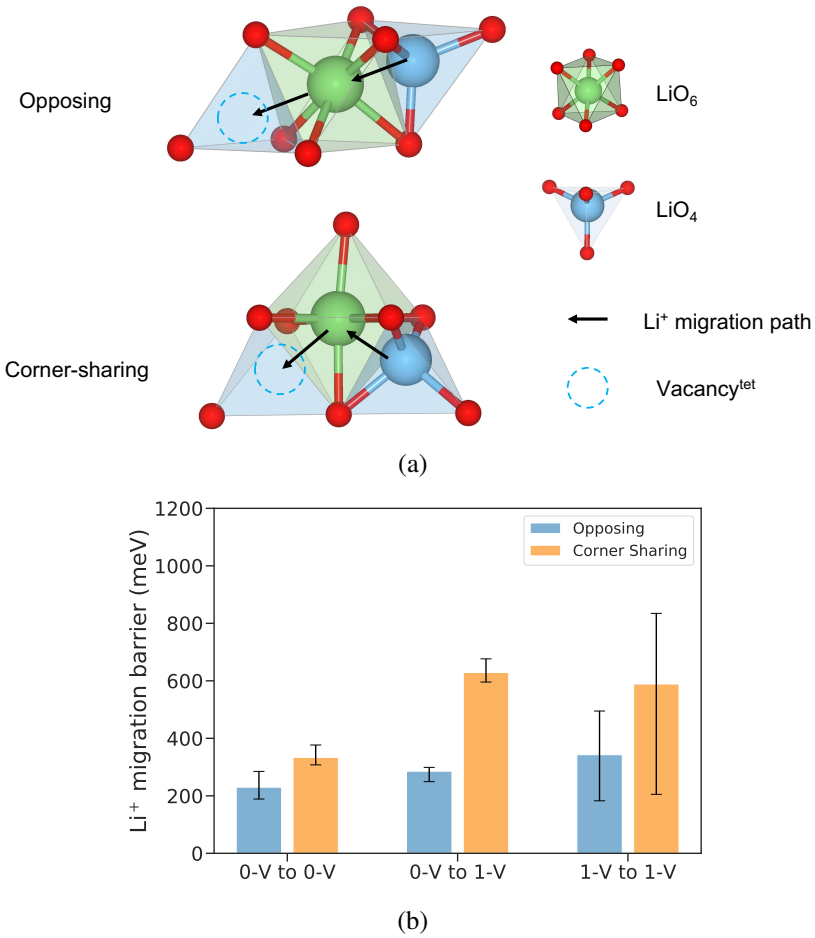

Figure 5.9: (a) Illustration of Li^+ migration path in DRX-$Li_3V_2O_5$. The opposing and corner-sharing pathways indicate cooperative migration mechanisms of Li^+ via the octahedral site and its next tetrahedral site. (b) Calculated NEB barriers for possible Li migration hops. The barriers are categorized in terms of their mechanisms and local environments.

5.4 Discussion

In DRX electrodes, The Li^+ transportation depends on the distribution of tetrahedral sites and their connectivity. Our results show that Li^+ in 0-V sites are the most energetically favorable and have the lowest migration barrier, which is critical for fast Li^+ diffusion during

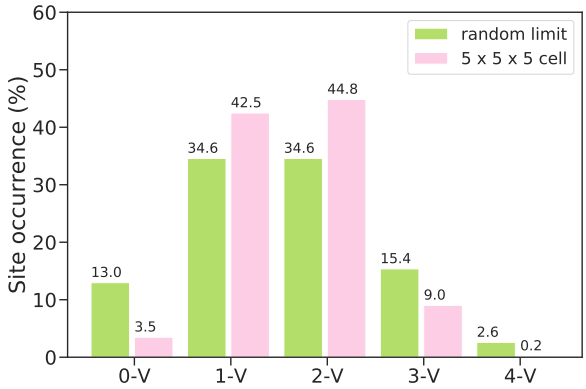

Figure 5.10: (a) Occurrence of tetrahedral sites with different local environment predicted by cluster expansion in $5 \times 5 \times 5$ DRX-$Li_3V_2O_5$ supercell and random limit.

charge/discharge processes. Figure 5.10 shows the occurrence of various tetrahedral sites in DRX-$Li_3V_2O_5$ structures averaged over 500 equilibrated structures from MC simulations at 1500 K as well as that in the random limit. The occurrence of 0V sites only accounts for 3.5 % of the diffusion sites in DRX-$Li_3V_2O_5$, which is significantly lower than that in the random limit. While the populations of 1-V and 2-V sites are slightly higher than that in the random limit. These observations indicate that the local arrangements of the tetrahedral sites are modified by short-range orderings (SROs), which are influenced by the materials chemistry and have been shown to affect the kinetic properties of DRX electrodes considerably. According to Ji et al. [63], the formation of 0-V sites depends on two competing factors: i) The existence of V^{3+} and V^{4+} tends to promote the mixing of Li and V ions due to the large repulsive electrostatic interactions between V ions. Also, large mismatch between the ionic radius of Li^+(0.76 Å) and V^{4+} (0.58 Å) might promote Li segregation into 0-V sites to reduce the strain effect. Therefore, we propose that to further optimize the electrochemical performance of DRX-$Li_3V_2O_5$, substituting V^{4+} by element with a smaller radius, for example, Cr^{4+}(0.55 Å), is likely to introduce more 0-V sites for Li^+ and thus enhancing its electrochemical performance.

5.5 Conclusion

To summarize, we have performed a systematic study of the mechanism of Li intercalation into DRX-$Li_3V_2O_5$ anode by coupling DFT calculations with cluster expansion and molecular dynamic simulations. Based on the semi-GCMC calculations, we find that the intercalated Li ions in the DRX-$Li_3V_2O_5$ anode are mainly populated in tetrahedral sites while most cations in octahedral sites remain immobile. Furthermore, the exceptionally high rate capability and superior cycling stability of DRX-$Li_3V_2O_5$ anode are due to the facile diffusion of Li ions along the "tetrahedral - octahedral - tetrahedral" pathway and the pillar effect of disordered V ions.

Chapter 5, in part is currently being prepared for submission for publication of the material "The Intercalation Chemistry of the Disordered RockSalt $Li_3V_2O_5$ Anode from Cluster Expansions and Machine Learning Interatomic Potentials." Xingyu Guo, Chi Chen, Shyue Ping Ong. The dissertation author was the primary investigator and author of this paper.

Appendix: Supplementary The Intercalation Chemistry of the Disordered RockSalt $Li_3V_2O_5$ Anode from Cluster Expansions and Machine Learning Interatomic Potentials

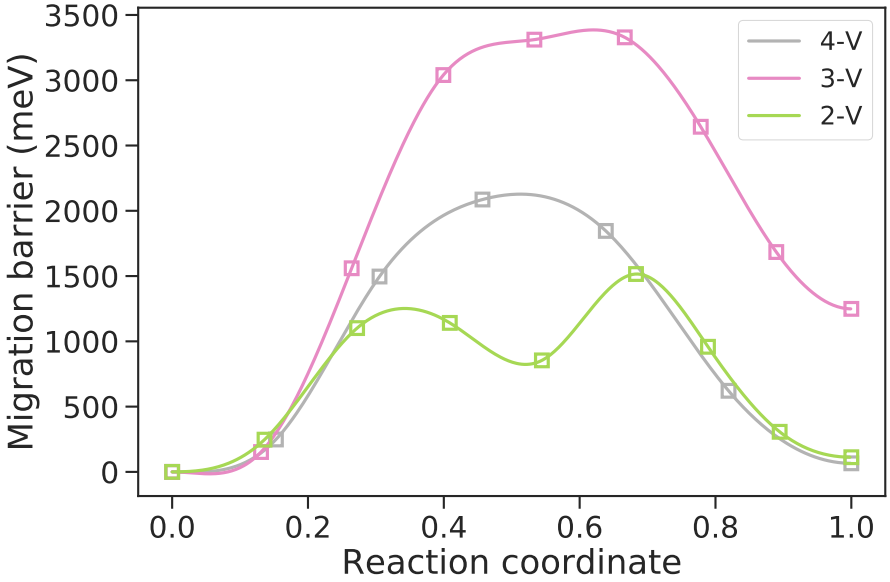

(a)

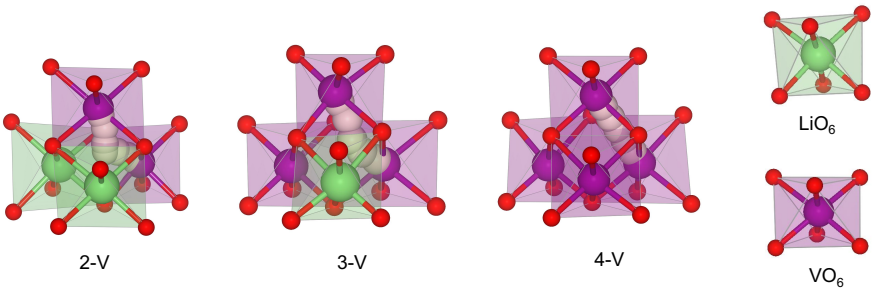

(b)

Figure 5.11: (a) DFT calculated V^{4+}/V^{3+} migration barriers through 2-V, 3-V and 4-V sites (b) Illustration of the DFT optimized hopping path of V atoms in varied local environment.

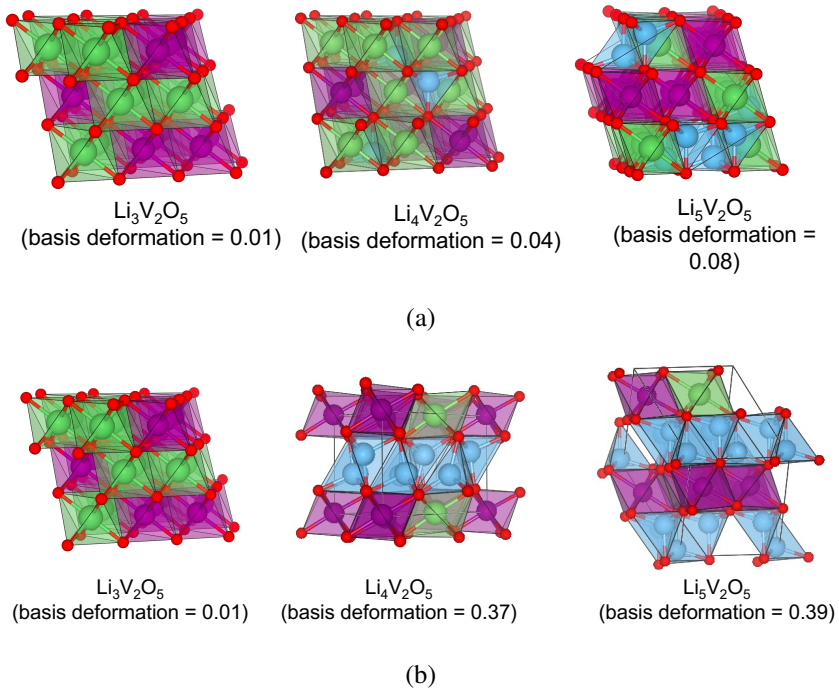

Figure 5.12: (a) The structures of ground states and (b) lowest energy metastable cubic phase of $Li_{3+x}V_2O_5$ (x = 0, 1, 2)

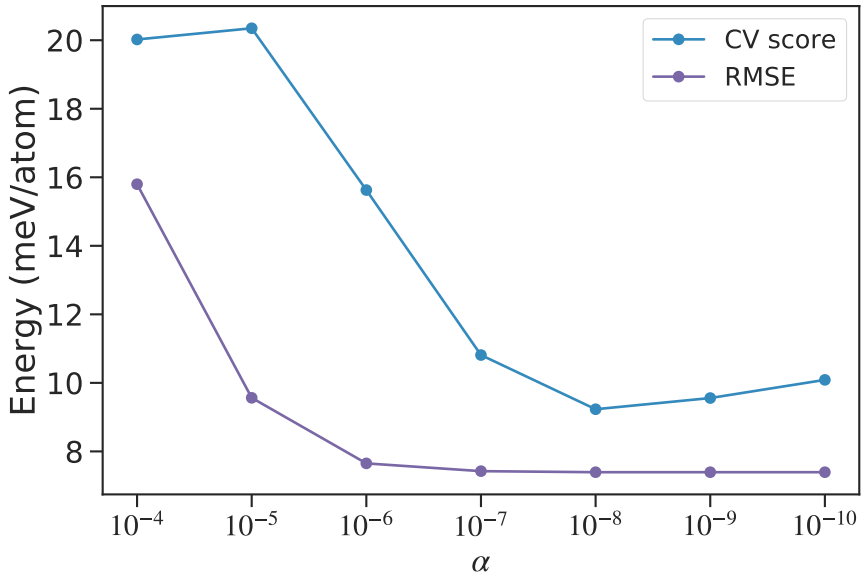

Figure 5.13: Cross-validation (CV) score and root mean square error (RMSE) of the fitted cluster expansion model as a function of the amount of penalization (α) used in the fit to minimize overfitting.

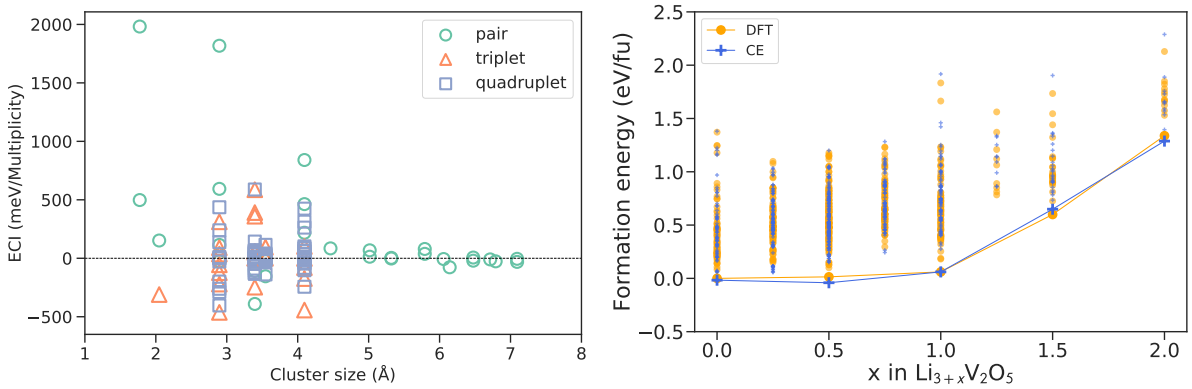

(a) (b)

Figure 5.14: (a) Fitted effective cluster interactions (ECI) values with respect to the size of the clusters (b) DFT calculated and cluster expansion (CE) predicted formation energy of $Li_{3+x}V_2O_5$ (x = 0.0 - 2.0)

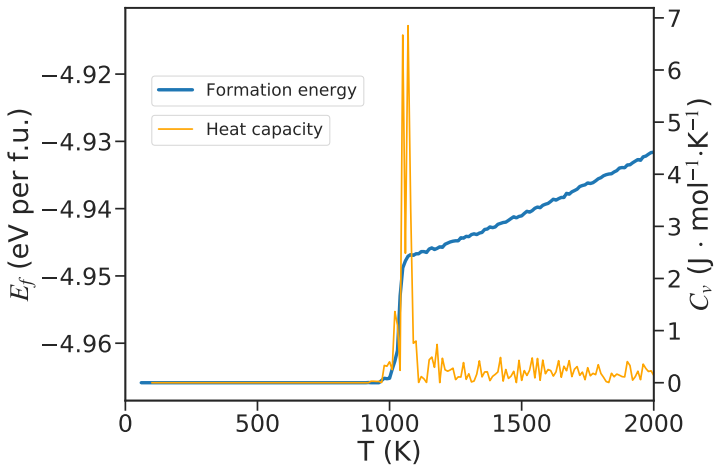

Figure 5.15: Monte Carlo simulations of order-disorder phase transition of $Li_3V_2O_5$ in $10\times10\times10$ supercell

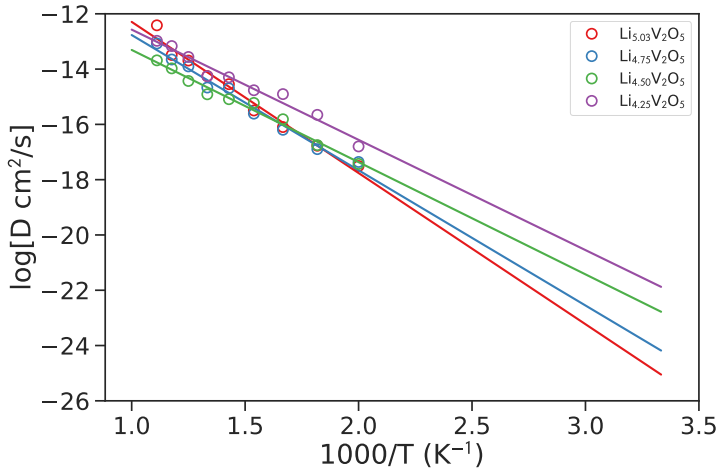

(a)

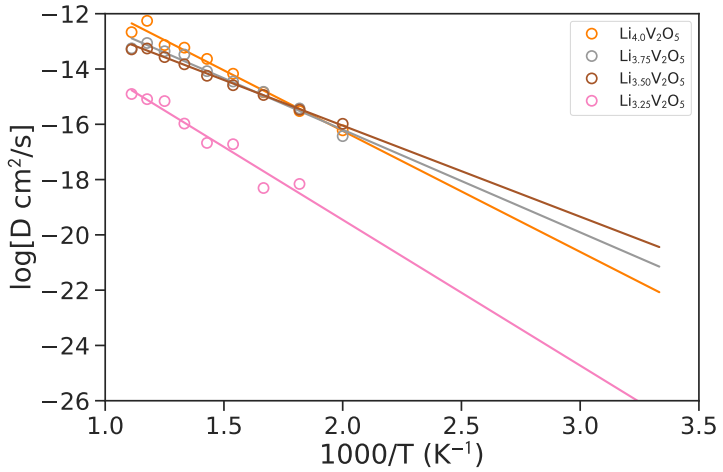

(b)

Figure 5.16: Arrhenius plot from NpT/MD simulations for each composition of $Li_{3+x}V_2O_5$

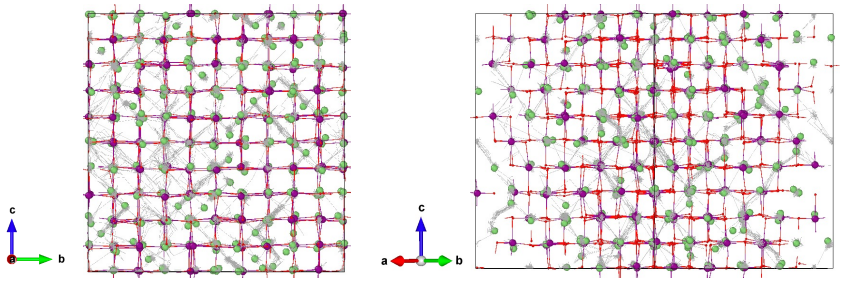

(a) $Li_{3.25}V_2O_5$

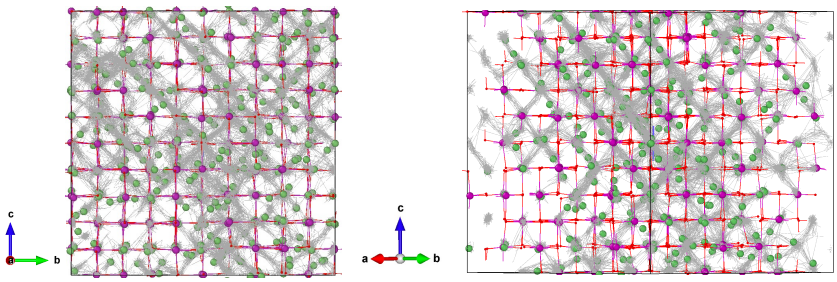

(b) $Li_{3.5}V_2O_5$

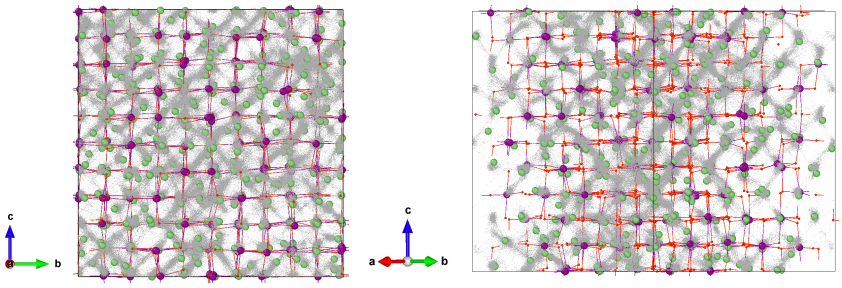

(c) $Li_{3.75}V_2O_5$

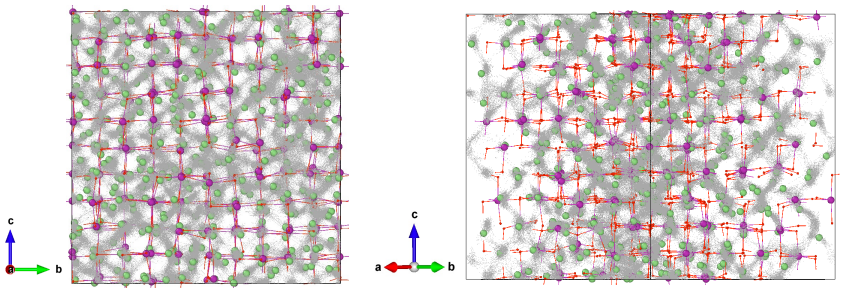

(d) $Li_{4.0}V_2O_5$

Figure 5.17: Calculated Li^+ trajectories obtained from MD simulations

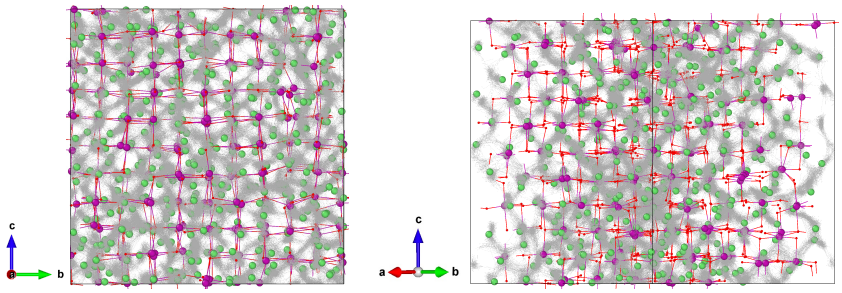

(a) $Li_{4.25}V_2O_5$

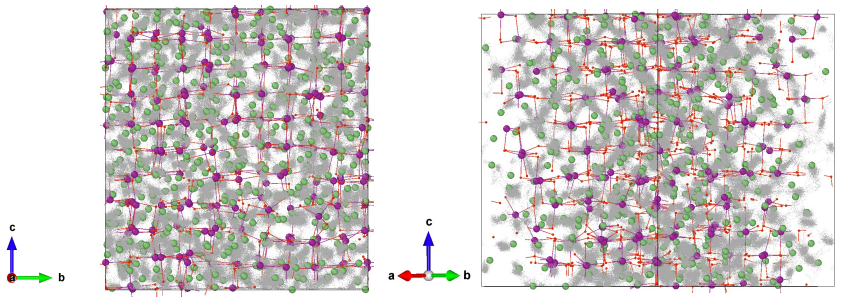

(b) $Li_{4.50}V_2O_5$

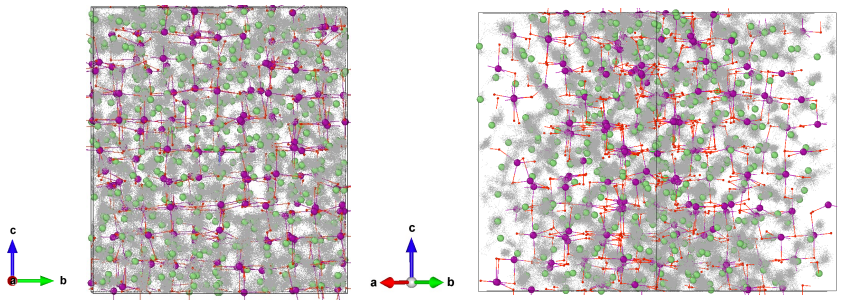

(c) $Li_{4.75}V_2O_5$

Figure 5.17: (Continued) Calculated Li^+ trajectories obtained from MD simulations

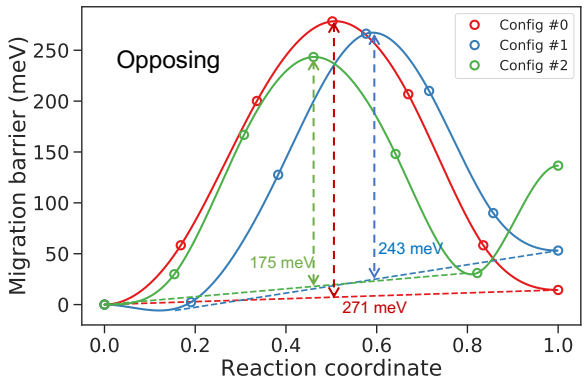

(d) 0-V to 0-V (Opposing)

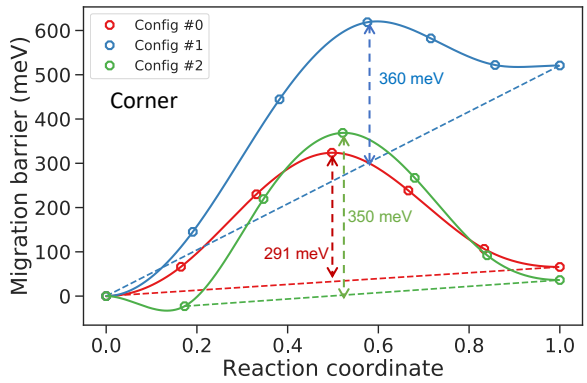

(e) 0-V to 0-V (Corner-Sharing)

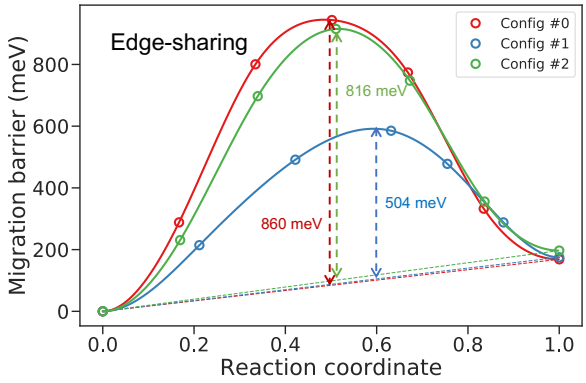

(f) 0-V to 0-V (Edge-Sharing)

Figure 5.18: DFT calculated Li^+ migration barriers in 0-V sites

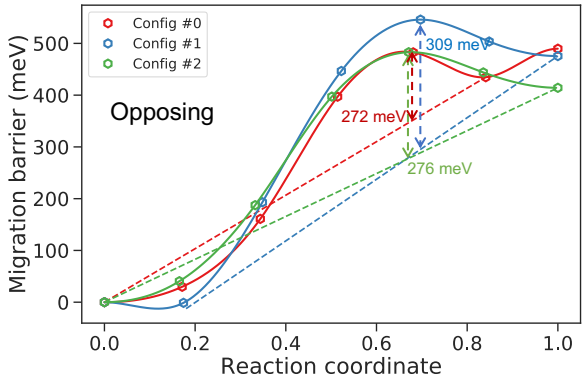

(a) 0-V to 1-V (Opposing)

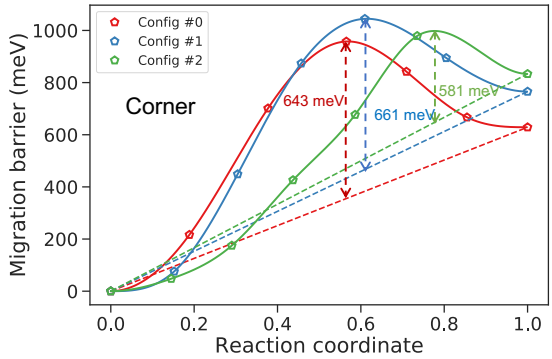

(b) 0-V to 1-V (Corner-sharing)

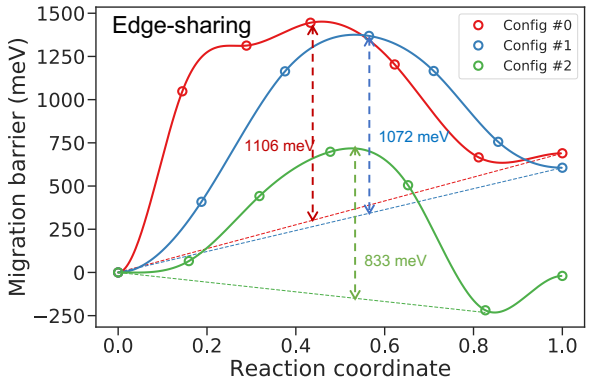

(c) 0-V to 1-V (Edge-sharing)

Figure 5.19: DFT calculated Li^+ migration barriers via 0-V and 1-V sites

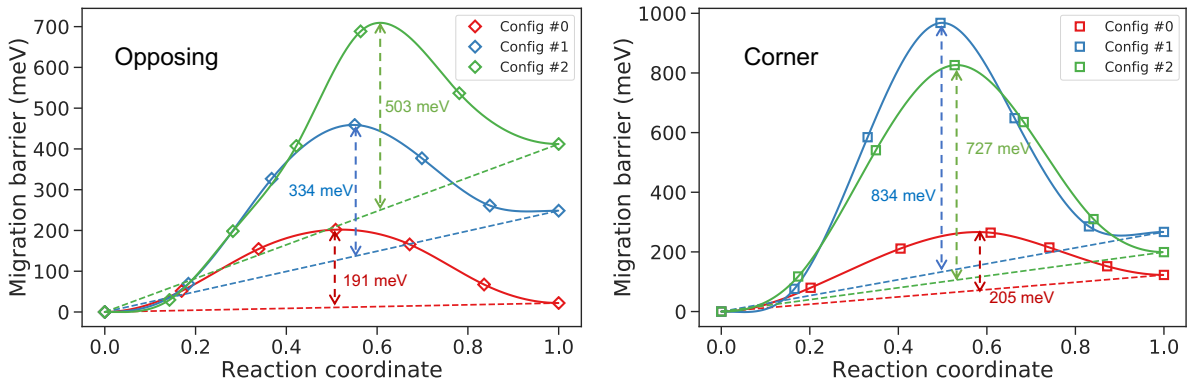

(a) 1-V to 1-V (Opposing)

(b) 1-V to 1-V (Corner Sharing)

Figure 5.20: DFT calculated Li^+ migration barriers via 1-V sites

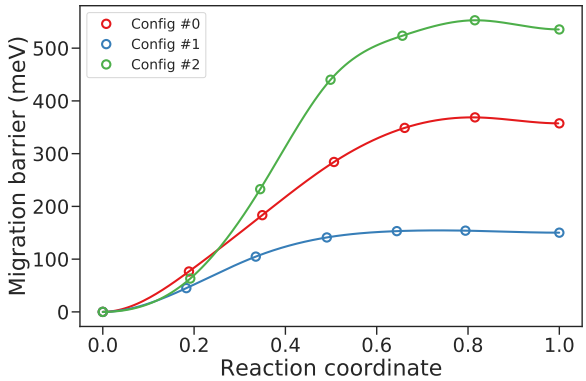

(a) 1-V to 2-V (Opposing)

Figure 5.21: DFT calculated Li^+ migration barriers via connected 1-V and 2-V sites

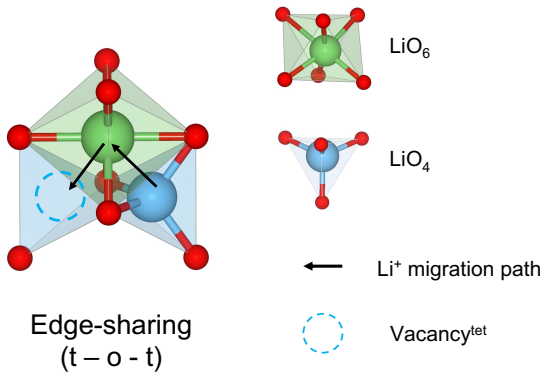

(a)

Figure 5.22: Illustration of Li^+ migration via edge-sharing "t-o-t " path in DRX-$Li_3V_2O_5$.

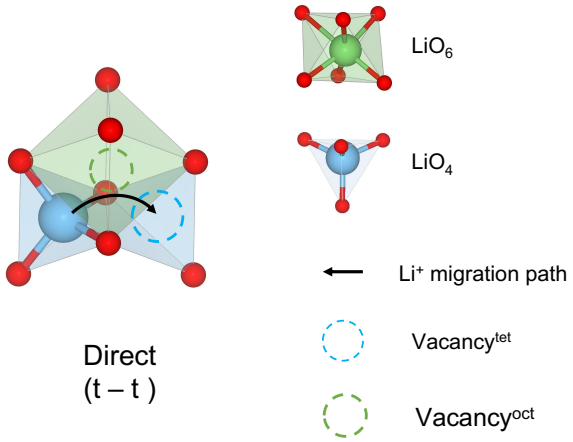

(a)

Figure 5.23: Illustration of Li^+ migration via "t-t " path in DRX-$Li_3V_2O_5$. The direct pathway indicates a divacancy mechanism of Li^{tet} vacancies at the end of discharge.

Chapter 6

Summary

In the first project, we performed a comprehensive study of Prussian blue and its analogues (PBAs), one of the most promising cathode materials for aqueous sodium-ion batteries (ASIBs) for large-scale energy storage systems, using first principles calculations. It is confirmed that dry PBAs generally undergo a phase transition from a rhombohedral $Na_2PR(CN)_6$ (where P and R are transition metals) to a tetragonal/cubic $PR(CN)_6$ during Na extraction, in agreement with experimental observations. Using a grand potential phase diagram construction, we show that water and Na co-intercalation result in fundamentally different phase transition behavior, and hence, electrochemical voltage profiles in wet versus dry electrolytes. Lattice water increases the average voltage and reduces the volume change during electrochemical cycling, resulting in both higher energy density and better cycling stability. Finally, we identified four new PBA compositions – $Na_2CoMn(CN)_6$, $Na_2NiMn(CN)_6$, $Na_2CuMn(CN)_6$ and $Na_2ZnMn(CN)_6$ – that show great promise as cathodes for aqueous rechargeable Na-ion batteries.

In the second project, we developed design rules for aqueous sodium-ion battery cathodes through a comprehensive density functional theory study of the working potential and aqueous stability of known cathode materials. These design rules were applied in a high-throughput screening of Na-ion battery cathode materials for application in aqueous electrolytes. Five

promising cathode materials - NASICON-$Na_3Fe_2(PO_4)_3$, Na_2FePO_4F, $Na_3FeCO_3PO_4$, alluadite-$Na_2Fe_3(PO_4)_3$ and $Na_3MnCO_3PO_4$, were identified as hitherto unexplored aqueous sodium-ion battery cathodes, with high voltage, good capacity, high stability in aqueous environments and facile Na-ion migration. These findings pave the way the practical cathode development for large-scale energy storage systems based on aqueous Na-ion battery chemistry.

Based on the developed design rules in the second project, we designed a high throughput (HT) workflow for automated descriptor calculations, data storage and analysis. In total, our database contains 3847 computed compounds with calculated properties of structure, phase stability, theoretical capacity, average voltage and aqueous stabilities. A user-friendly web-GUI have been developed for data visualization. In the end, we proposed two promising candidates, $Na_2(FeVO_4)_3$ and $NaMn_2O_4$ for further experimental validations.

Last but not the least, we presents a comprehensive study of Li insertion mechanism in *DRX*-$Li_3V_2O_5$, which is a promising candidate for anode in rechargeable lithium ion batteries because of its low work potential, high rate capability and superior cycling stability. Using a combination of first-principles calculations and cluster expansion methods, we show that during discharge, Li ions mainly intercalate into tetrahedral sites, while the majority of Li and V ions in octahedral sites remain stable. Furthermore, its fast-charging nature is attributed to the facile diffusivity of Li ions via a correlated "octahedral - tetrahedral - octahedral" Li diffusion.

Bibliography

[1] Catl unveils its latest breakthrough technology by releasing its first generation of sodium-ion batteries. https://www.catl.com/en/news/665.html.

[2] Iea (2021), global energy review 2021, iea, paris, https://www.iea.org/reports/global-energy-review-2021.

[3] Casm, v1.1.1. https://github.com/prisms-center/casmcode, 2021.

[4] P. Agreement. Paris agreement. In *Report of the Conference of the Parties to the United Nations Framework Convention on Climate Change (21st Session, 2015: Paris). Retrived December*, volume 4, page 2017. HeinOnline, 2015.

[5] A. S. Arico, P. Bruce, B. Scrosati, J.-M. Tarascon, and W. Van Schalkwijk. Nanostructured materials for advanced energy conversion and storage devices. In *Materials for sustainable energy: a collection of peer-reviewed research and review articles from Nature Publishing Group*, pages 148–159. World Scientific, 2011.

[6] A. R. Armstrong, C. Lyness, P. M. Panchmatia, M. S. Islam, and P. G. Bruce. The lithium intercalation process in the low-voltage lithium battery anode $Li_{1+x}V_{1-x}O_2$. *Nature materials*, 10(3):223–229, 2011.

[7] L. Athouël, F. Moser, R. Dugas, O. Crosnier, D. Bélanger, and T. Brousse. Variation of the MnO_2 birnessite structure upon charge/discharge in an electrochemical supercapacitor electrode in aqueous na_2so_4 electrolyte. *The Journal of Physical Chemistry C*, 112(18): 7270–7277, 2008.

[8] M. Aydinol, A. Kohan, G. Ceder, K. Cho, and J. Joannopoulos. Ab initio study of lithium intercalation in metal oxides and metal dichalcogenides. *Physical Review B*, 56(3):1354, 1997.

[9] M. Aydinol, A. Kohan, G. Ceder, K. Cho, and J. Joannopoulos. Ab initio study of lithium intercalation in metal oxides and metal dichalcogenides. *Physical Review B*, 56(3):1354, 1997.

[10] Q. Bai, L. Yang, H. Chen, and Y. Mo. Computational studies of electrode materials in sodium-ion batteries. *Advanced energy materials*, 8(17):1702998, 2018.

[11] P. Barnes, Y. Zuo, K. Dixon, D. Hou, S. Lee, Z. Ma, J. G. Connell, H. Zhou, C. Deng, K. Smith, et al. Electrochemically induced amorphous-to-rock-salt phase transformation in niobium oxide electrode for li-ion batteries. *Nature Materials*, pages 1–9, 2022.

[12] P. Barpanda, T. Ye, M. Avdeev, S.-C. Chung, and A. Yamada. A new polymorph of $Na_2MnP_2O_7$ as a 3.6 v cathode material for sodium-ion batteries. *Journal of Materials Chemistry A*, 1(13):4194–4197, 2013.

[13] P. Barpanda, G. Oyama, S.-i. Nishimura, S.-C. Chung, and A. Yamada. A 3.8-V earth-abundant sodium battery electrode. *Nature communications*, 5(1):1–8, 2014.

[14] C. Baur, J. Chable, F. Klein, V. S. K. Chakravadhanula, and M. Fichtner. Reversible delithiation of disordered rock salt $LiVO_2$. *ChemElectroChem*, 5(11):1484–1490, 2018.

[15] G. Bergerhoff, R. Hundt, R. Sievers, and I. Brown. The inorganic crystal structure data base. *Journal of chemical information and computer sciences*, 23(2):66–69, 1983.

[16] G. Bergerhoff, R. Hundt, R. Sievers, and I. D. Brown. The inorganic crystal structure data base. *Journal of Chemical Information and Modeling*, 23(2):66–69, may 1983. ISSN 1549-9596. doi: 10.1021/ci00038a003.

[17] D. Bin, F. Wang, A. G. Tamirat, L. Suo, Y. Wang, C. Wang, and Y. Xia. Progress in aqueous rechargeable sodium-ion batteries. *Advanced Energy Materials*, 8(17):1703008, 2018.

[18] P. E. Blöchl. Projector augmented-wave method. *Physical review B*, 50(24):17953, 1994.

[19] P. E. Blöchl. Projector augmented-wave method. *Physical review B*, 50(24):17953, 1994.

[20] F. Boucher, J. Gaubicher, M. Cuisinier, D. Guyomard, and P. Moreau. Elucidation of the $Na_{2/3}FePO_4$ and $Li_{2/3}FePO_4$ intermediate superstructure revealing a pseudouniform ordering in 2d. *Journal of the American Chemical Society*, 136(25):9144–9157, 2014.

[21] D. A. Brownson, D. K. Kampouris, and C. E. Banks. An overview of graphene in energy production and storage applications. *Journal of Power Sources*, 196(11):4873–4885, 2011.

[22] D. A. Brownson, L. J. Munro, D. K. Kampouris, and C. E. Banks. Electrochemistry of graphene: not such a beneficial electrode material? *Rsc Advances*, 1(6):978–988, 2011.

[23] X. Bu, L. Su, Q. Dou, S. Lei, and X. Yan. A low-cost "water-in-salt" electrolyte for a 2.3 v high-rate carbon-based supercapacitor. *Journal of materials chemistry A*, 7(13):7541–7547, 2019.

[24] Y. Cao, L. Xiao, W. Wang, D. Choi, Z. Nie, J. Yu, L. V. Saraf, Z. Yang, and J. Liu. Reversible sodium ion insertion in single crystalline manganese oxide nanowires with long cycle life. *Advanced Materials*, 23(28):3155–3160, 2011.

[25] G. Ceder, M. Aydinol, and A. Kohan. Application of first-principles calculations to the design of rechargeable li-batteries. *Computational materials science*, 8(1-2):161–169, 1997.

[26] G. Ceder, Y.-M. Chiang, D. Sadoway, M. Aydinol, Y.-I. Jang, and B. Huang. Identification of cathode materials for lithium batteries guided by first-principles calculations. *Nature*, 392(6677):694–696, 1998.

[27] C. Chen, Q. J. Yunxing Zuo, Weike Ye, and S. P. Ong. Maml - materials machine learning package. https://github.com/materialsvirtuallab/maml, 2020.

[28] H. Chen, Q. Hao, O. Zivkovic, G. Hautier, L.-S. Du, Y. Tang, Y.-Y. Hu, X. Ma, C. P. Grey, and G. Ceder. Sidorenkite ($Na_3MnPO_4CO_3$): a new intercalation cathode material for na-ion batteries. *Chemistry of Materials*, 25(14):2777–2786, 2013.

[29] R. Clément, Z. Lun, and G. Ceder. Cation-disordered rocksalt transition metal oxides and oxyfluorides for high energy lithium-ion cathodes. *Energy & Environmental Science*, 13 (2):345–373, 2020.

[30] Y. Cui. Silicon anodes. *Nature Energy*, 6(10):995–996, 2021.

[31] D. De Fontaine. Cluster approach to order-disorder transformations in alloys. 47:33–176, 1994.

[32] C. Delacourt, P. Poizot, J.-M. Tarascon, and C. Masquelier. The existence of a temperature-driven solid solution in Li_xFePO_4 for $0 \leq x \leq 1$. *Nature materials*, 4(3):254–260, 2005.

[33] C. Delmas and H. Cognac-Auradou. Formation of the ω-type phase by lithium intercalation in (mo, v) oxides deriving from V_2O_5. *Journal of power sources*, 54(2):406–410, 1995.

[34] S. Dudarev, G. Botton, S. Savrasov, C. Humphreys, and A. Sutton. Electron-energy-loss spectra and the structural stability of nickel oxide: An lsda+ u study. *Physical Review B*, 57(3):1505, 1998.

[35] A. Fernández-Ropero, D. Saurel, B. Acebedo, T. Rojo, and M. Casas-Cabanas. Electrochemical characterization of $NaFePO_4$ as positive electrode in aqueous sodium-ion batteries. *Journal of Power Sources*, 291:40–45, 2015.

[36] A. Fernández-Ropero, M. Piernas-Muñoz, E. Castillo-Martínez, T. Rojo, and M. Casas-Cabanas. Electrochemical characterization of $NaFe_2(CN)_6$ prussian blue as positive electrode for aqueous sodium-ion batteries. *Electrochimica Acta*, 210:352–357, 2016.

[37] A. J. Fernández-Ropero, M. Zarrabeitia, M. Reynaud, T. Rojo, and M. Casas-Cabanas. Toward safe and sustainable batteries: $Na_4Fe_3(PO_4)_2P_2O_7$ as a low-cost cathode for rechargeable aqueous na-ion batteries. *The Journal of Physical Chemistry C*, 122(1):133–142, 2018.

[38] G. Fornasieri, A. Bordage, and A. Bleuzen. Magnetism and photomagnetism of prussian blue analogue nanoparticles embedded in porous metal oxide ordered nanostructures. *European Journal of Inorganic Chemistry*, 2018(3-4):259–271, 2018.

[39] H. Gao and J. B. Goodenough. An aqueous symmetric sodium-ion battery with nasicon-structured $Na_3MnTi(PO_4)_3$. *Angewandte Chemie International Edition*, 55(41):12768–12772, 2016.

[40] H. J. S. Ge and M. Ernzerhof. Erratum:"hybrid functionals based on a screened coulomb potential"[j. chem. phys. 118, 8207 (2003)]. *J Chem Phys*, 124:219906, 2006.

[41] J. B. Goodenough, H.-P. Hong, and J. Kafalas. Fast Na^+-ion transport in skeleton structures. *Materials Research Bulletin*, 11(2):203–220, 1976.

[42] K. Gubaev, E. V. Podryabinkin, G. L. Hart, and A. V. Shapeev. Accelerating high-throughput searches for new alloys with active learning of interatomic potentials. *Computational Materials Science*, 156:148–156, 2019.

[43] X. Guo, Z. Wang, Z. Deng, X. Li, B. Wang, X. Chen, and S. P. Ong. Water contributes to higher energy density and cycling stability of prussian blue analogue cathodes for aqueous sodium-ion batteries. *Chemistry of Materials*, 31(15):5933–5942, 2019.

[44] G. L. Hart and R. W. Forcade. Algorithm for generating derivative structures. *Physical Review B*, 77(22):224115, 2008.

[45] G. Hautier, A. Jain, H. Chen, C. Moore, S. P. Ong, and G. Ceder. Novel mixed polyanions lithium-ion battery cathode materials predicted by high-throughput ab initio computations. *Journal of Materials Chemistry*, 21(43):17147–17153, 2011.

[46] G. Hautier, A. Jain, S. P. Ong, B. Kang, C. Moore, R. Doe, and G. Ceder. Phosphates as lithium-ion battery cathodes: an evaluation based on high-throughput ab initio calculations. *Chemistry of Materials*, 23(15):3495–3508, 2011.

[47] G. Hautier, A. Jain, S. P. Ong, B. Kang, C. Moore, R. Doe, and G. Ceder. Phosphates as lithium-ion battery cathodes: an evaluation based on high-throughput ab initio calculations. *Chemistry of Materials*, 23(15):3495–3508, 2011.

[48] G. He, A. Huq, W. H. Kan, and A. Manthiram. β-$NaVOPO_4$ obtained by a low-temperature synthesis process: a new 3.3 v cathode for sodium-ion batteries. *Chemistry of Materials*, 28(5):1503–1512, 2016.

[49] P. Henkel, S. Zahn, J. Lorenz, T. Jacob, J. Janek, and D. Mollenhauer. Temperature-dependent li vacancy diffusion in $Li_4Ti_5O_{12}$ by means of first principles molecular dynamic simulations. *Physical Chemistry Chemical Physics*, 24(9):5301–5316, 2022.

[50] G. Henkelman and H. Jónsson. Improved tangent estimate in the nudged elastic band method for finding minimum energy paths and saddle points. *The Journal of chemical physics*, 113(22):9978–9985, 2000.

[51] G. Henkelman, B. P. Uberuaga, and H. Jónsson. A climbing image nudged elastic band method for finding saddle points and minimum energy paths. *The Journal of chemical physics*, 113(22):9901–9904, 2000.

[52] F. Herren, P. Fischer, A. Ludi, and W. Hälg. Neutron diffraction study of prussian blue, $Fe_4[Fe(CN)_6]_3 \cdot xH_2O$. location of water molecules and long-range magnetic order. *Inorganic Chemistry*, 19(4):956–959, 1980.

[53] T. Hewston and B. Chamberland. A survey of first-row ternary oxides $LiMO_2$ (m= sc-cu). *Journal of Physics and Chemistry of Solids*, 48(2):97–108, 1987.

[54] J. Heyd, G. E. Scuseria, and M. Ernzerhof. Hybrid functionals based on a screened coulomb potential. *The Journal of chemical physics*, 118(18):8207–8215, 2003.

[55] J. Heyd, G. E. Scuseria, and M. Ernzerhof. Hybrid functionals based on a screened coulomb potential. *The Journal of chemical physics*, 118(18):8207–8215, 2003.

[56] W. G. Hoover. Canonical dynamics: Equilibrium phase-space distributions. *Physical review A*, 31(3):1695, 1985.

[57] J. Hou, Y. Shao, M. W. Ellis, R. B. Moore, and B. Yi. Graphene-based electrochemical energy conversion and storage: fuel cells, supercapacitors and lithium ion batteries. *Physical Chemistry Chemical Physics*, 13(34):15384–15402, 2011.

[58] W. Huang, J. Zhou, B. Li, J. Ma, S. Tao, D. Xia, W. Chu, and Z. Wu. Detailed investigation of $Na_{2.24}FePO_4CO_3$ as a cathode material for na-ion batteries. *Scientific reports*, 4:4188, 2014.

[59] W. Huang, B. Li, M. F. Saleem, X. Wu, J. Li, J. Lin, D. Xia, W. Chu, and Z. Wu. Self-assembled alluaudite $Na_2Fe_{3-x}Mn_x(PO_4)_3$ micro/nanocompounds for sodium-ion battery electrodes: A new insight into their electronic and geometric structure. *Chemistry–A European Journal*, 21(2):851–860, 2015.

[60] A. Jain, G. Hautier, S. P. Ong, C. J. Moore, C. C. Fischer, K. A. Persson, and G. Ceder. Formation enthalpies by mixing gga and gga+ u calculations. *Physical Review B*, 84(4): 045115, 2011.

[61] A. Jain, S. P. Ong, G. Hautier, W. Chen, W. D. Richards, S. Dacek, S. Cholia, D. Gunter, D. Skinner, G. Ceder, et al. Commentary: The materials project: A materials genome approach to accelerating materials innovation. *APL materials*, 1(1):011002, 2013.

[62] A. Jain, S. P. Ong, G. Hautier, W. Chen, W. D. Richards, S. Dacek, S. Cholia, D. Gunter, D. Skinner, G. Ceder, et al. Commentary: The materials project: A materials genome approach to accelerating materials innovation. *Apl Materials*, 1(1):011002, 2013.

[63] H. Ji, A. Urban, D. A. Kitchaev, D.-H. Kwon, N. Artrith, C. Ophus, W. Huang, Z. Cai, T. Shi, J. C. Kim, et al. Hidden structural and chemical order controls lithium transport in cation-disordered oxides for rechargeable batteries. *Nature communications*, 10(1):1–9, 2019.

[64] Z. Ji, B. Han, H. Liang, C. Zhou, Q. Gao, K. Xia, and J. Wu. On the mechanism of the improved operation voltage of rhombohedral nickel hexacyanoferrate as cathodes for sodium-ion batteries. *ACS Applied Materials & Interfaces*, 8(49):33619–33625, 2016.

[65] Y. H. Jung, C. H. Lim, J.-H. Kim, and D. K. Kim. $Na_2FeP_2O_7$ as a positive electrode material for rechargeable aqueous sodium-ion batteries. *Rsc Advances*, 4(19):9799–9802, 2014.

[66] B. Kang and G. Ceder. Battery materials for ultrafast charging and discharging. *Nature*, 458(7235):190–193, 2009.

[67] K. Kang, Y. S. Meng, J. Breger, C. P. Grey, and G. Ceder. Electrodes with high power and high capacity for rechargeable lithium batteries. *Science*, 311(5763):977–980, 2006.

[68] C. M. Kareis, S. H. Lapidus, J.-H. Her, P. W. Stephens, and J. S. Miller. Non-prussian blue structures and magnetic ordering of $Na_2MnII[MnII(CN)_6]$ and $Na_2MnII[MnII(CN)_6]\cdot{}_2H_2O$. *Journal of the American Chemical Society*, 134(4):2246–2254, 2012.

[69] Y. Kawabe, N. Yabuuchi, M. Kajiyama, N. Fukuhara, T. Inamasu, R. Okuyama, I. Nakai, and S. Komaba. Synthesis and electrode performance of carbon coated Na_2FePO_4F for rechargeable na batteries. *Electrochemistry Communications*, 13(11):1225–1228, 2011.

[70] D. J. Kim, R. Ponraj, A. G. Kannan, H.-W. Lee, R. Fathi, R. Ruffo, C. M. Mari, and D. K. Kim. Diffusion behavior of sodium ions in $Na_{0.44}MnO_2$ in aqueous and non-aqueous electrolytes. *Journal of Power Sources*, 244:758–763, 2013.

[71] H. Kim, D. J. Kim, D.-H. Seo, M. S. Yeom, K. Kang, D. K. Kim, and Y. Jung. Ab initio study of the sodium intercalation and intermediate phases in $Na_{0.44}MnO_2$ for sodium-ion battery. *Chemistry of Materials*, 24(6):1205–1211, 2012.

[72] H. Kim, R. Shakoor, C. Park, S. Y. Lim, J.-S. Kim, Y. N. Jo, W. Cho, K. Miyasaka, R. Kahraman, Y. Jung, et al. $Na_2FeP_2O_7$ as a promising iron-based pyrophosphate cathode for sodium rechargeable batteries: a combined experimental and theoretical study. *Advanced Functional Materials*, 23(9):1147–1155, 2013.

[73] H. Kim, J. Hong, K.-Y. Park, H. Kim, S.-W. Kim, and K. Kang. Aqueous rechargeable li and na ion batteries. *Chemical reviews*, 114(23):11788–11827, 2014.

[74] H. Kim, J. Hong, K.-Y. Park, H. Kim, S.-W. Kim, and K. Kang. Aqueous rechargeable li and na ion batteries. *Chemical reviews*, 114(23):11788–11827, 2014.

[75] H. Kim, C. S. Park, J. W. Choi, and Y. Jung. Defect-controlled formation of triclinic $Na_2CoP_2O_7$ for 4 v sodium-ion batteries. *Angewandte Chemie International Edition*, 55 (23):6662–6666, 2016.

[76] S.-W. Kim, D.-H. Seo, X. Ma, G. Ceder, and K. Kang. Electrode materials for rechargeable sodium-ion batteries: potential alternatives to current lithium-ion batteries. *Advanced Energy Materials*, 2(7):710–721, 2012.

[77] D. A. Kitchaev, Z. Lun, W. D. Richards, H. Ji, R. J. Clément, M. Balasubramanian, D.-H. Kwon, K. Dai, J. K. Papp, T. Lei, et al. Design principles for high transition metal capacity in disordered rocksalt li-ion cathodes. *Energy & Environmental Science*, 11(8):2159–2171, 2018.

[78] N. Koshiba, K. Takata, E. Asaka, and M. Nakanishi. Rechargeable lithium cell and process for making an anode for use in the cell, Aug. 13 1996. US Patent 5,545,468.

[79] S. Kotrlỳ and L. Sucha. *Handbook of chemical equilibria in analytical chemis try*. 1985.

[80] G. Kresse and J. Furthmüller. Efficient iterative schemes for ab initio total-energy calculations using a plane-wave basis set. *Physical review B*, 54(16):11169, 1996.

[81] G. Kresse and J. Furthmüller. Efficient iterative schemes for ab initio total-energy calculations using a plane-wave basis set. *Physical review B*, 54(16):11169, 1996.

[82] K. Kubota, N. Yabuuchi, H. Yoshida, M. Dahbi, and S. Komaba. Layered oxides as positive electrode materials for na-ion batteries. *Mrs Bulletin*, 39(5):416–422, 2014.

[83] K. Kubota, K. Yokoh, N. Yabuuchi, and S. Komaba. Na_2CoPO_4F as a high-voltage electrode material for na-ion batteries. *Electrochemistry*, 82(10):909–911, 2014.

[84] H. J. Kulik, M. Cococcioni, D. A. Scherlis, and N. Marzari. Density functional theory in transition-metal chemistry: A self-consistent hubbard u approach. *Physical Review Letters*, 97(10):103001, 2006.

[85] D. Kundu, B. D. Adams, V. Duffort, S. H. Vajargah, and L. F. Nazar. A high-capacity and long-life aqueous rechargeable zinc battery using a metal oxide intercalation cathode. *Nature Energy*, 1(10):1–8, 2016.

[86] H.-W. Lee, R. Y. Wang, M. Pasta, S. Woo Lee, N. Liu, and Y. Cui. Manganese hexacyanomanganate open framework as a high-capacity positive electrode material for sodium-ion batteries. *Nature communications*, 5(1):1–6, 2014.

[87] J. Lee, A. Urban, X. Li, D. Su, G. Hautier, and G. Ceder. Unlocking the potential of cation-disordered oxides for rechargeable lithium batteries. *science*, 343(6170):519–522, 2014.

[88] M. Levi, E. Markevich, and D. Aurbach. The effect of slow interfacial kinetics on the chronoamperometric response of composite lithiated graphite electrodes and on the calculation of the chemical diffusion coefficient of Li ions in graphite. *The Journal of Physical Chemistry B*, 109(15):7420–7427, 2005.

[89] C. Li, L. Gu, J. Tong, S. Tsukimoto, and J. Maier. A mesoporous iron-based fluoride cathode of tunnel structure for rechargeable lithium batteries. *Advanced Functional Materials*, 21(8):1391–1397, 2011.

[90] H. Li, X. Liu, T. Zhai, D. Li, and H. Zhou. Li_3VO_4: a promising insertion anode material for lithium-ion batteries. *Advanced Energy Materials*, 3(4):428–432, 2013.

[91] Q. Li, Z. Liu, F. Zheng, R. Liu, J. Lee, G.-L. Xu, G. Zhong, X. Hou, R. Fu, Z. Chen, et al. Identifying the structural evolution of the sodium ion battery Na_2FePO_4F cathode. *Angewandte Chemie*, 130(37):12094–12099, 2018.

[92] W. Li, J. Reimers, and J. Dahn. Lattice-gas-model approach to understanding the structures of lithium transition-metal oxides $LiMO_2$. *Physical Review B*, 49(2):826, 1994.

[93] S. Y. Lim, H. Kim, R. Shakoor, Y. Jung, and J. W. Choi. Electrochemical and thermal properties of nasicon structured $Na_3V_2(PO_4)_3$ as a sodium rechargeable battery cathode: a combined experimental and theoretical study. *Journal of The Electrochemical Society*, 159 (9):A1393, 2012.

[94] S. Y. Lim, J. H. Lee, S. Kim, J. Shin, W. Choi, K. Y. Chung, D. S. Jung, and J. W. Choi. Lattice water for the enhanced performance of amorphous iron phosphate in sodium-ion batteries. *Acs Energy Letters*, 2(5):998–1004, 2017.

[95] Y.-C. Lin, B. Wen, K. M. Wiaderek, S. Sallis, H. Liu, S. H. Lapidus, O. J. Borkiewicz, N. F. Quackenbush, N. A. Chernova, K. Karki, et al. Thermodynamics, kinetics and structural evolution of ε-$LiVOPO_4$ over multiple lithium intercalation. *Chemistry of Materials*, 28 (6):1794–1805, 2016.

[96] C. Ling, J. Chen, and F. Mizuno. First-principles study of alkali and alkaline earth ion intercalation in iron hexacyanoferrate: the important role of ionic radius. *The Journal of Physical Chemistry C*, 117(41):21158–21165, 2013.

[97] P. Linstorm. Nist chemistry webbook, nist standard reference database number 69. *J. Phys. Chem. Ref. Data, Monograph*, 9:1–1951, 1998.

[98] H. Liu, Z. Zhu, Q. Yan, S. Yu, X. He, Y. Chen, R. Zhang, L. Ma, T. Liu, M. Li, et al. A disordered rock salt anode for fast-charging lithium-ion batteries. *Nature*, 585(7823): 63–67, 2020.

[99] Y. Liu, Y. Zhu, and Y. Cui. Challenges and opportunities towards fast-charging battery materials. *Nature Energy*, 4(7):540–550, 2019.

[100] Y. Lu, S. Zhang, Y. Li, L. Xue, G. Xu, and X. Zhang. Preparation and characterization of carbon-coated $NaVPO_4F$ as cathode material for rechargeable sodium-ion batteries. *Journal of Power Sources*, 247:770–777, 2014.

[101] J.-Y. Luo, W.-J. Cui, P. He, and Y.-Y. Xia. Raising the cycling stability of aqueous lithium-ion batteries by eliminating oxygen in the electrolyte. *Nature chemistry*, 2(9):760–765, 2010.

[102] K. Mizushima, P. Jones, P. Wiseman, and J. B. Goodenough. Li_xCoO_2 ($0 < x <$-1): A new cathode material for batteries of high energy density. *Materials Research Bulletin*, 15(6): 783–789, 1980.

[103] K. Nakamoto, R. Sakamoto, M. Ito, A. Kitajou, and S. Okada. Effect of concentrated electrolyte on aqueous sodium-ion battery with sodium manganese hexacyanoferrate cathode. *Electrochemistry*, 85(4):179–185, 2017.

[104] S. Nakanishi, M. Nose, H. Nakayama, and H. Iba. Study of new active materials for rechargeable sodium-ion batteries. In *Advances in Science and Technology*, volume 93, pages 137–145. Trans Tech Publ, 2014.

[105] K. W. Nam, S. Kim, E. Yang, Y. Jung, E. Levi, D. Aurbach, and J. W. Choi. Critical role of crystal water for a layered cathode material in sodium ion batteries. *Chemistry of Materials*, 27(10):3721–3725, 2015.

[106] M. Nishino, S. Kubo, Y. Yoshioka, A. Nakamura, and K. Yamaguchi. Theoretical studies on magnetic interactions in prussian blue analogs and active controls of spin states by external fields. *Molecular Crystals and Liquid Crystals Science and Technology. Section A. Molecular Crystals and Liquid Crystals*, 305(1):109–128, 1997.

[107] J. K. Nørskov, J. Rossmeisl, A. Logadottir, L. Lindqvist, J. R. Kitchin, T. Bligaard, and H. Jonsson. Origin of the overpotential for oxygen reduction at a fuel-cell cathode. *The Journal of Physical Chemistry B*, 108(46):17886–17892, 2004.

[108] J. K. Nørskov, J. Rossmeisl, A. Logadottir, L. Lindqvist, J. R. Kitchin, T. Bligaard, and H. Jonsson. Origin of the overpotential for oxygen reduction at a fuel-cell cathode. *The Journal of Physical Chemistry B*, 108(46):17886–17892, 2004.

[109] S. Nosé. A unified formulation of the constant temperature molecular dynamics methods. *The Journal of chemical physics*, 81(1):511–519, 1984.

[110] I. S. Novikov, K. Gubaev, E. V. Podryabinkin, and A. V. Shapeev. The mlip package: moment tensor potentials with mpi and active learning. *Machine Learning: Science and Technology*, 2(2):025002, 2020.

[111] M. Obrovac and L. Christensen. Structural changes in silicon anodes during lithium insertion/extraction. *Electrochemical and solid-state letters*, 7(5):A93, 2004.

[112] S.-M. Oh, S.-T. Myung, J. Hassoun, B. Scrosati, and Y.-K. Sun. Reversible nafepo$_4$ electrode for sodium secondary batteries. *Electrochemistry Communications*, 22:149–152, 2012.

[113] S. P. Ong, L. Wang, B. Kang, and G. Ceder. Li−Fe−P−O_2 phase diagram from first principles calculations. *Chemistry of Materials*, 20(5):1798–1807, 2008.

[114] S. P. Ong, L. Wang, B. Kang, and G. Ceder. $Li - Fe - P - O_2$ phase diagram from first principles calculations. *Chemistry of Materials*, 20(5):1798–1807, 2008.

[115] S. P. Ong, V. L. Chevrier, G. Hautier, A. Jain, C. Moore, S. Kim, X. Ma, and G. Ceder. Voltage, stability and diffusion barrier differences between sodium-ion and lithium-ion intercalation materials. *Energy & Environmental Science*, 4(9):3680–3688, 2011.

[116] S. P. Ong, V. L. Chevrier, G. Hautier, A. Jain, C. Moore, S. Kim, X. Ma, and G. Ceder. Voltage, stability and diffusion barrier differences between sodium-ion and lithium-ion intercalation materials. *Energy & Environmental Science*, 4(9):3680–3688, 2011.

[117] S. P. Ong, W. D. Richards, A. Jain, G. Hautier, M. Kocher, S. Cholia, D. Gunter, V. L. Chevrier, K. A. Persson, and G. Ceder. Python materials genomics (pymatgen): A robust, open-source python library for materials analysis. *Computational Materials Science*, 68: 314–319, 2013.

[118] S. P. Ong, W. D. Richards, A. Jain, G. Hautier, M. Kocher, S. Cholia, D. Gunter, V. L. Chevrier, K. A. Persson, and G. Ceder. Python materials genomics (pymatgen): A robust, open-source python library for materials analysis. *Computational Materials Science*, 68: 314–319, 2013.

[119] A. K. Padhi, K. S. Nanjundaswamy, and J. B. Goodenough. Phospho-olivines as positive-electrode materials for rechargeable lithium batteries. *Journal of the electrochemical society*, 144(4):1188, 1997.

[120] G. Pang, P. Nie, C. Yuan, L. Shen, X. Zhang, J. Zhu, and B. Ding. Enhanced performance of aqueous sodium-ion batteries using electrodes based on the $NaTi_2(PO_4)_3$/mwnts–$Na_{0.44}MnO_2$ system. *Energy Technology*, 2(8):705–712, 2014.

[121] M. Park, X. Zhang, M. Chung, G. B. Less, and A. M. Sastry. A review of conduction phenomena in li-ion batteries. *Journal of power sources*, 195(24):7904–7929, 2010.

[122] S. I. Park, I. Gocheva, S. Okada, and J.-i. Yamaki. Electrochemical properties of $NaTi_2(PO_4)_3$ anode for rechargeable aqueous sodium-ion batteries. *Journal of The Electrochemical Society*, 158(10):A1067–A1070, 2011.

[123] Y.-U. Park, D.-H. Seo, H. Kim, J. Kim, S. Lee, B. Kim, and K. Kang. A family of high-performance cathode materials for na-ion batteries, $Na_3(VO_{1-x}PO_4)_2F_{1+2x}$ ($0 \geq x \leq 1$): Combined first-principles and experimental study. *Advanced Functional Materials*, 24 (29):4603–4614, 2014.

[124] M. Pasta, R. Y. Wang, R. Ruffo, R. Qiao, H.-W. Lee, B. Shyam, M. Guo, Y. Wang, L. A. Wray, W. Yang, et al. Manganese–cobalt hexacyanoferrate cathodes for sodium-ion batteries. *Journal of Materials Chemistry A*, 4(11):4211–4223, 2016.

[125] H. Peng, Z.-H. Yang, J. P. Perdew, and J. Sun. Versatile van der waals density functional based on a meta-generalized gradient approximation. *Physical Review X*, 6(4):041005, 2016.

[126] J. P. Perdew, K. Burke, and M. Ernzerhof. Generalized gradient approximation made simple. *Physical review letters*, 77(18):3865, 1996.

[127] J. P. Perdew, K. Burke, and M. Ernzerhof. Generalized gradient approximation made simple. *Physical review letters*, 77(18):3865, 1996.

[128] J. P. Perdew, A. Ruzsinszky, G. I. Csonka, O. A. Vydrov, G. E. Scuseria, L. A. Constantin, X. Zhou, and K. Burke. Restoring the density-gradient expansion for exchange in solids and surfaces. *Physical review letters*, 100(13):136406, 2008.

[129] K. Persson, V. A. Sethuraman, L. J. Hardwick, Y. Hinuma, Y. S. Meng, A. Van Der Ven, V. Srinivasan, R. Kostecki, and G. Ceder. Lithium diffusion in graphitic carbon. *The journal of physical chemistry letters*, 1(8):1176–1180, 2010.

[130] K. A. Persson, B. Waldwick, P. Lazic, and G. Ceder. Prediction of solid-aqueous equilibria: Scheme to combine first-principles calculations of solids with experimental aqueous states. *Physical Review B*, 85(23):235438, 2012.

[131] Y. Preger, H. M. Barkholtz, A. Fresquez, D. L. Campbell, B. W. Juba, J. Romàn-Kustas, S. R. Ferreira, and B. Chalamala. Degradation of commercial lithium-ion cells as a function of chemistry and cycling conditions. *Journal of The Electrochemical Society*, 167(12): 120532, 2020.

[132] J. Qi, S. Banerjee, Y. Zuo, C. Chen, Z. Zhu, M. H. Chandrappa, X. Li, and S. P. Ong. Bridging the gap between simulated and experimental ionic conductivities in lithium superionic conductors. *Materials Today Physics*, 21:100463, 2021.

[133] J. Qian, C. Wu, Y. Cao, Z. Ma, Y. Huang, X. Ai, and H. Yang. Prussian blue cathode materials for sodium-ion batteries and other ion batteries. *Advanced Energy Materials*, 8 (17):1702619, 2018.

[134] S. Qiu, X. Wu, M. Wang, M. Lucero, Y. Wang, J. Wang, Z. Yang, W. Xu, Q. Wang, M. Gu, et al. Nasicon-type $Na_3Fe_2(PO_4)_3$ as a low-cost and high-rate anode material for aqueous sodium-ion batteries. *Nano Energy*, 64:103941, 2019.

[135] Q. Qu, P. Zhang, B. Wang, Y. Chen, S. Tian, Y. Wu, and R. Holze. Electrochemical performance of MnO_2 nanorods in neutral aqueous electrolytes as a cathode for asymmetric supercapacitors. *The Journal of Physical Chemistry C*, 113(31):14020–14027, 2009.

[136] B. Radhakrishnan and S. P. Ong. Aqueous stability of alkali superionic conductors from first-principles calculations. *Frontiers in Energy Research*, 4:16, 2016.

[137] R. Rajagopalan, B. Chen, Z. Zhang, X.-L. Wu, Y. Du, Y. Huang, B. Li, Y. Zong, J. Wang, G.-H. Nam, et al. Improved reversibility of Fe^{3+}/Fe^{4+} redox couple in sodium super ion conductor type $Na_3Fe_2(PO_4)_3$ for sodium-ion batteries. *Advanced Materials*, 29(12): 1605694, 2017.

[138] G. Sai Gautam, P. Canepa, W. D. Richards, R. Malik, and G. Ceder. Role of structural H_2O in intercalation electrodes: the case of mg in nanocrystalline xerogel-V_2O_5. *Nano Letters*, 16(4):2426–2431, 2016.

[139] J. M. Sanchez, F. Ducastelle, and D. Gratias. Generalized cluster description of multicomponent systems. *Physica A: Statistical Mechanics and its Applications*, 128(1-2):334–350, 1984.

[140] A. Saracibar, J. Carrasco, D. Saurel, M. Galceran, B. Acebedo, H. Anne, M. Lepoitevin, T. Rojo, and M. C. Cabanas. Investigation of sodium insertion–extraction in olivine Na_xFePO_4 ($0 \leq x \leq 1$) using first-principles calculations. *Physical Chemistry Chemical Physics*, 18(18):13045–13051, 2016.

[141] K. Saravanan, C. W. Mason, A. Rudola, K. H. Wong, and P. Balaya. The first report on excellent cycling stability and superior rate capability of $Na_3V_2(PO_4)_3$ for sodium ion batteries. *Advanced Energy Materials*, 3(4):444–450, 2013.

[142] X. Shan, D. S. Charles, Y. Lei, R. Qiao, G. Wang, W. Yang, M. Feygenson, D. Su, and X. Teng. Bivalence Mn_5O_8 with hydroxylated interphase for high-voltage aqueous sodium-ion storage. *Nature communications*, 7(1):1–8, 2016.

[143] A. V. Shapeev. Moment tensor potentials: A class of systematically improvable interatomic potentials. *Multiscale Modeling & Simulation*, 14(3):1153–1173, 2016.

[144] L. Sharma, K. Nakamoto, R. Sakamoto, S. Okada, and P. Barpanda. Na_2FePO_4F fluorophosphate as positive insertion material for aqueous sodium-ion batteries. *ChemElectroChem*, 6(2):444–449, 2019.

[145] N. Shimamoto, S.-i. Ohkoshi, O. Sato, and K. Hashimoto. Control of charge-transfer-induced spin transition temperature on cobalt- iron prussian blue analogues. *Inorganic chemistry*, 41(4):678–684, 2002.

[146] C. Shinagawa, Y. Morikawa, S.-i. Nishimura, H. Ushiyama, A. Yamada, and K. Yamashita. A theoretical study on the charge and discharge states of na-ion battery cathode material, $Na_{1+x}FePO_4F$. *Journal of computational chemistry*, 40(1):237–246, 2019.

[147] A. K. Singh, L. Zhou, A. Shinde, S. K. Suram, J. H. Montoya, D. Winston, J. M. Gregoire, and K. A. Persson. Electrochemical stability of metastable materials. *Chemistry of Materials*, 29(23):10159–10167, 2017.

[148] J. Song, M. Xu, L. Wang, and J. B. Goodenough. Exploration of $NaVOPO_4$ as a cathode for a na-ion battery. *Chemical Communications*, 49(46):5280–5282, 2013.

[149] J. Song, L. Wang, Y. Lu, J. Liu, B. Guo, P. Xiao, J.-J. Lee, X.-Q. Yang, G. Henkelman, and J. B. Goodenough. Removal of interstitial H_2O in hexacyanometallates for a superior cathode of a sodium-ion battery. *Journal of the American Chemical Society*, 137(7): 2658–2664, 2015.

[150] W. Song, X. Ji, Y. Zhu, H. Zhu, F. Li, J. Chen, F. Lu, Y. Yao, and C. E. Banks. Aqueous sodium-ion battery using a $Na_3V_2(PO_4)_3$ electrode. *ChemElectroChem*, 1(5):871–876, 2014.

[151] J. Sun, A. Ruzsinszky, and J. Perdew. Strongly Constrained and Appropriately Normed Semilocal Density Functional. *Physical Review Letters*, 115(3):036402, jul 2015. doi: 10.1103/PhysRevLett.115.036402.

[152] J. Sun, A. Ruzsinszky, and J. P. Perdew. Strongly constrained and appropriately normed semilocal density functional. *Physical review letters*, 115(3):036402, 2015.

[153] W. Sun, D. A. Kitchaev, D. Kramer, and G. Ceder. Non-equilibrium crystallization pathways of manganese oxides in aqueous solution. *Nature communications*, 10(1):1–9, 2019.

[154] S. Takai, M. Kamata, S. Fujine, K. Yoneda, K. Kanda, and T. Esaka. Diffusion coefficient measurement of lithium ion in sintered $Li_{1.33}Ti_{1.67}O_4$ by means of neutron radiography. *Solid State Ionics*, 123(1-4):165–172, 1999.

[155] M. M. Thackeray and K. Amine. $Li_4ti_5o_{12}$ spinel anodes. *Nature Energy*, 6(6):683–683, 2021.

[156] J. C. Thomas and A. Van der Ven. Finite-temperature properties of strongly anharmonic and mechanically unstable crystal phases from first principles. *Physical Review B*, 88(21): 214111, 2013.

[157] A. P. Thompson, H. M. Aktulga, R. Berger, D. S. Bolintineanu, W. M. Brown, P. S. Crozier, P. J. in't Veld, A. Kohlmeyer, S. G. Moore, T. D. Nguyen, et al. Lammps-a flexible simulation tool for particle-based materials modeling at the atomic, meso, and continuum scales. *Computer Physics Communications*, 271:108171, 2022.

[158] M. Toupin, T. Brousse, and D. Bélanger. Charge storage mechanism of MnO_2 electrode used in aqueous electrochemical capacitor. *Chemistry of Materials*, 16(16):3184–3190, 2004.

[159] A. Urban, I. Matts, A. Abdellahi, and G. Ceder. Computational design and preparation of cation-disordered oxides for high-energy-density li-ion batteries. *Advanced Energy Materials*, 6(15):1600488, 2016.

[160] C. Vaalma, D. Buchholz, M. Weil, and S. Passerini. A cost and resource analysis of sodium-ion batteries. *Nature reviews materials*, 3(4):1–11, 2018.

[161] A. Van der Ven, G. Ceder, M. Asta, and P. Tepesch. First-principles theory of ionic diffusion with nondilute carriers. *Physical Review B*, 64(18):184307, 2001.

[162] A. Van der Ven, J. Thomas, Q. Xu, and J. Bhattacharya. Linking the electronic structure of solids to their thermodynamic and kinetic properties. *Mathematics and computers in simulation*, 80(7):1393–1410, 2010.

[163] A. Van der Ven, Z. Deng, S. Banerjee, and S. P. Ong. Rechargeable alkali-ion battery materials: theory and computation. *Chemical Reviews*, 120(14):6977–7019, 2020.

[164] B. Wang, Y. Han, X. Wang, N. Bahlawane, H. Pan, M. Yan, and Y. Jiang. Prussian blue analogs for rechargeable batteries. *Iscience*, 3:110–133, 2018.

[165] C. Wang, K. Aoyagi, P. Wisesa, and T. Mueller. Lithium ion conduction in cathode coating materials from on-the-fly machine learning. *Chemistry of Materials*, 32(9):3741–3752, 2020.

[166] H. Wang, T. Zhang, C. Chen, M. Ling, Z. Lin, S. Zhang, F. Pan, and C. Liang. High-performance aqueous symmetric sodium-ion battery using nasicon-structured $Na_2VTi(PO_4)_3$. *Nano Research*, 11(1):490–498, 2018.

[167] L. Wang, T. Maxisch, and G. Ceder. Oxidation energies of transition metal oxides within the gga+ u framework. *Physical Review B*, 73(19):195107, 2006.

[168] L. Wang, J. Song, R. Qiao, L. A. Wray, M. A. Hossain, Y.-D. Chuang, W. Yang, Y. Lu, D. Evans, J.-J. Lee, et al. Rhombohedral prussian white as cathode for rechargeable sodium-ion batteries. *Journal of the American Chemical Society*, 137(7):2548–2554, 2015.

[169] Y. Wang, J. Liu, B. Lee, R. Qiao, Z. Yang, S. Xu, X. Yu, L. Gu, Y.-S. Hu, W. Yang, et al. Ti-substituted tunnel-type $Na_{0.44}MnO_2$ oxide as a negative electrode for aqueous sodium-ion batteries. *Nature communications*, 6(1):1–10, 2015.

[170] Z. Wang, J. Ha, Y. H. Kim, W. B. Im, J. McKittrick, and S. P. Ong. Mining unexplored chemistries for phosphors for high-color-quality white-light-emitting diodes. *Joule*, 2(5): 914–926, 2018.

[171] C. D. Wessells, R. A. Huggins, and Y. Cui. Copper hexacyanoferrate battery electrodes with long cycle life and high power. *Nature communications*, 2(1):1–5, 2011.

[172] C. D. Wessells, S. V. Peddada, R. A. Huggins, and Y. Cui. Nickel hexacyanoferrate nanoparticle electrodes for aqueous sodium and potassium ion batteries. *Nano letters*, 11 (12):5421–5425, 2011.

[173] C. D. Wessells, S. V. Peddada, R. A. Huggins, and Y. Cui. Nickel hexacyanoferrate nanoparticle electrodes for aqueous sodium and potassium ion batteries. *Nano letters*, 11 (12):5421–5425, 2011.

[174] J. Whitacre, A. Tevar, and S. Sharma. $Na_4Mn_9O_{18}$ as a positive electrode material for an aqueous electrolyte sodium-ion energy storage device. *Electrochemistry Communications*, 12(3):463–466, 2010.

[175] M. S. Whittingham and A. H. Thompson. Intercalation and lattice expansion in titanium disulfide. *The Journal of Chemical Physics*, 62(4):1588–1588, 1975.

[176] J. C. Wojdeł, I. de PR Moreira, S. T. Bromley, and F. Illas. On the prediction of the crystal and electronic structure of mixed-valence materials by periodic density functional calculations: The case of prussian blue. *The Journal of chemical physics*, 128(4):044713, 2008.

[177] X. Wu, W. Deng, J. Qian, Y. Cao, X. Ai, and H. Yang. Single-crystal $FeFe(CN)_6$ nanoparticles: a high capacity and high rate cathode for na-ion batteries. *Journal of Materials Chemistry A*, 1(35):10130–10134, 2013.

[178] X. Wu, Y. Luo, M. Sun, J. Qian, Y. Cao, X. Ai, and H. Yang. Low-defect prussian blue nanocubes as high capacity and long life cathodes for aqueous na-ion batteries. *Nano Energy*, 13:117–123, 2015.

[179] X. Wu, C. Wu, C. Wei, L. Hu, J. Qian, Y. Cao, X. Ai, J. Wang, and H. Yang. Highly crystallized $Na_2CoFe(CN)_6$ with suppressed lattice defects as superior cathode material for sodium-ion batteries. *ACS applied materials & interfaces*, 8(8):5393–5399, 2016.

[180] X.-y. Wu, M.-y. Sun, Y.-f. Shen, J.-f. Qian, Y.-l. Cao, X.-p. Ai, and H.-x. Yang. Energetic aqueous rechargeable sodium-ion battery based on $Na_2CuFe(CN)_6$–$NaTi_2(PO_4)_3$ intercalation chemistry. *ChemSusChem*, 7(2):407–411, 2014.

[181] P. Xiao, J. Song, L. Wang, J. B. Goodenough, and G. Henkelman. Theoretical study of the structural evolution of a $Na_2FeMn(CN)_6$ cathode upon na intercalation. *Chemistry of Materials*, 27(10):3763–3768, 2015.

[182] P. Xiao, J. Song, L. Wang, J. B. Goodenough, and G. Henkelman. Theoretical study of the structural evolution of a $Na_2FeMn(CN)_6$ cathode upon na intercalation. *Chemistry of Materials*, 27(10):3763–3768, 2015.

[183] H. Xiong, M. D. Slater, M. Balasubramanian, C. S. Johnson, and T. Rajh. Amorphous TiO_2 nanotube anode for rechargeable sodium ion batteries. *The journal of physical chemistry letters*, 2(20):2560–2565, 2011.

[184] Y. You, X.-L. Wu, Y.-X. Yin, and Y.-G. Guo. High-quality prussian blue crystals as superior cathode materials for room-temperature sodium-ion batteries. *Energy & Environmental Science*, 7(5):1643–1647, 2014.

[185] L. Zhang, T. Huang, and A. Yu. Carbon-coated $Na_3V_2(PO_4)_3$ nanocomposite as a novel high rate cathode material for aqueous sodium ion batteries. *Journal of Alloys and Compounds*, 646:522–527, 2015.

[186] W. Zhang, J. Liang, Y. Zhu, Y. Qian, et al. Facile synthesis and electrochemistry of a new cubic rocksalt $Li_xV_yO_2$ (x= 0.78, y= 0.75) electrode material. *Journal of Materials Chemistry A*, 5(10):5148–5155, 2017.

[187] W. Zhang, D.-H. Seo, T. Chen, L. Wu, M. Topsakal, Y. Zhu, D. Lu, G. Ceder, and F. Wang. Kinetic pathways of ionic transport in fast-charging lithium titanate. *Science*, 367(6481): 1030–1034, 2020.

[188] Y. Zhang, C. Yuan, K. Ye, X. Jiang, J. Yin, G. Wang, and D. Cao. An aqueous capacitor battery hybrid device based on na-ion insertion-deinsertion in λ-MnO_2 positive electrode. *Electrochimica Acta*, 148:237–243, 2014.

[189] Y. Zhong, Z. Wu, Y. Tang, W. Xiang, X. Guo, and B. Zhong. Micro-nano structure Na_2MnPO_4F/c as cathode material with excellent sodium storage properties. *Materials Letters*, 145:269–272, 2015.

[190] T. Zhu, P. Hu, X. Wang, Z. Liu, W. Luo, K. A. Owusu, W. Cao, C. Shi, J. Li, L. Zhou, et al. Realizing three-electron redox reactions in nasicon-structured $Na_3MnTi(PO_4)_3$ for sodium-ion batteries. *Advanced Energy Materials*, 9(9):1803436, 2019.

[191] A. Zunger, S.-H. Wei, L. Ferreira, and J. E. Bernard. Special quasirandom structures. *Physical review letters*, 65(3):353, 1990.

[192] Y. Zuo, C. Chen, X. Li, Z. Deng, Y. Chen, J. Behler, G. Csányi, A. V. Shapeev, A. P. Thompson, M. A. Wood, et al. Performance and cost assessment of machine learning interatomic potentials. *The Journal of Physical Chemistry A*, 124(4):731–745, 2020.